Rapid electric-field molecular fingerprinting

Advancing infrared laser spectroscopy for blood-based phenotype diagnostics

Philip Jacob

SIGILL·UNIVERSITAT·LUDOVIC·MAXIM

München 2024

Rapid electric-field molecular fingerprinting

Advancing infrared laser spectroscopy for blood-based phenotype diagnostics

Philip Jacob

Dissertation
der Fakultät für Physik
der Ludwig-Maximilians-Universität
München

vorgelegt von
Philip Jacob
aus Chennai, Indien

München, den 13. Dezember 2023

Erstgutachter: Prof. Dr. Ferenc Krausz
Zweitgutachter: Prof. Dr. Jürgen Hauer
Tag der mündlichen Prüfung: 06. Februar 2024

Contents

List of Figures

List of Tables

List of Abbreviations

ASOPS	asynchronous optical sampling
CW	continuous wave
DFG	difference-frequency generation
ECOPS	electronically controlled optical sampling
EMF	electric-field molecular fingerprint
EODT	electro-optic delay tracking
EOS	electro-optic sampling
FFT	fast Fourier transform
FTIR	Fourier transform infrared
HNF	highly nonlinear fiber
IPDFG	intra-pulse difference frequency generation
LGS	$LiGaS_2$
LO	local oscillator
MIR	mid-infrared
NIR	near-infrared
OAPM	off-axis parabolic mirror
PID	proportional, integral, and derivative
QWP	quarter-wave plate
ROC	receiver operating characteristic

RMS	root-mean-squared
SFG	sum-frequency generation
SHG	second harmonic generation
TF	transfer function
THG	third harmonic generation

Zusammenfassung

Menschliches Blutplasma besteht aus einer komplexen Mischung von Biomolekülen. Im Vergleich zu invasiven klinischen Tests, bei denen die molekulare Abdeckung und die Analysetiefe oft begrenzt sind, stellt die Infrarotspektroskopie komplexer Bioflüssigkeiten einen wertvollen, minimal-invasiven diagnostischen Ansatz dar. In mehreren Studien wurde die Wirksamkeit des blutbasierten molekularen Infrarot-Fingerabdrucks zur Bestimmung des Gesundheitszustands einer Person untersucht. Hierbei wurden hauptsächlich Fourier-Transform-Infrarotspektrometer eingesetzt. Aufgrund der limitierten Sensitivität der aktuell verfügbaren Geräte gestaltet sich die Detektion schwacher Infrarotabsorption schwierig. Daher wurde in dieser Dissertation die Femtosekundenlasertechnologie zur Entwicklung eines schnell scannenden, feldauflösenden Infrarot-Spektrometers mit Vorteilen in Bezug auf Sensitivität, Zeitgenauigkeit und Durchsatz genutzt, um die diagnostischen Möglichkeiten zu verbessern.

Ein zuvor entwickelter Yb:YAG-Scheibenlaseroszillator, welcher 16-fs-Pulse mit einer Repetitionsrate von 28 MHz emittiert, wurde genutzt, um 60-fs-Pulse im mittleren Infrarotbereich zwischen 6,5 µm und 11 µm (-20 dB) zu erzeugen. Es wurden zwei neue Methoden zur schnellen elektro-optischen Abtastung mit kHz-Raten demonstriert. Bei der ersten Methode variierte die optische Verzögerung mithilfe einer Sonotrode. Ein Teil der optischen Leistung des 16-fs-Pulses wurde als Gate für die elektro-optische Abtastung genutzt. Die Gate-Pulse wurden an der Sonotrode reflektiert, um schnelle Verzögerungsscans zu ermöglichen, bei der 38.000 Spuren der mittleren Infrarot-Wellenform pro Sekunde erfasst wurden. In einem einzigen Scan, der in 26 µs durchgeführt wurde, wurde ein Dynamikumfang des elektrischen Feldes von 150 mit einer zeitlichen Präzision von 34 Attosekunden an den Nulldurchgangspunkten erreicht.

Bei der zweiten Methode wurden die Gate-Pulse für die elektro-optische Abtastung von einem Er:Fiber-Laseroszillator geliefert. Eine elektronisch gesteuerte Modulation der Repetitionsrate wurde verwendet, um die relative Verzögerung zwischen den Pulsen im mittleren Infrarotbereich und den

Gate-Pulsen zu scannen. Die neue elektro-optische Verzögerungsverfolgungstechnik ermöglichte die genaue Abbildung der relativen Verzögerung, indem eine schmalbandige Mittlere-IR-Wellenform mit einer bekannten optischen Frequenz als Kalibrationssignal erzeugt und durch elektro-optisches Scannen erfasst wurde. Die Er:Fiber-Laserpulse wurden in zwei geteilt, wobei ein Teil als Gate für das Kalibrationssignal und der andere Teil als Gate für die breitbandige mittlere IR-Wellenform diente, die aus der Probenküvette austrat. Es werden 2.800 Wellenformspuren pro Sekunde erfasst.

In früheren Arbeiten über hochpräzise Dual-Oszillator-Spektrometer wurde ein konstanter Offset zwischen den Repetitionsraten verwendet. Dies entspricht bei Repetitionsraten im MHz-Bereich Verzögerungsbereichen im Nanosekundenbereich, die für die Gasphasenspektroskopie geeignet sind. Für die Kondensationsphasenspektroskopie hingegen sind deutlich kürzere Verzögerungsbereiche in der Größenordnung von Pikosekunden erforderlich. Das Dual-Oszillator-Schnellabtastungs-Spektrometer mit elektro-optischer Verzögerungsnachführung ermöglicht eine präzise Abtastung von Pikosekunden-Verzögerungen mit einem höheren Tastverhältnis als bisherige Methoden. In einem einzigen Scan, der in 357 µs durchgeführt wurde, wurde eine Zeitpräzision von 50 Attosekunden für die Nulldurchgänge der Wellenform im Verzögerungsfenster mit der höchsten Signalstärke erreicht. Die schnelle Messung mit kHz-Raten "friert" das technische Rauschen im sub-kHz-Bereich ein und ermöglicht die Erfassung dynamischer Prozesse, z. B. in der Durchflusszytometrie. Bei statischen Proben wird die Sensitivität durch die Mittelung wiederholter Messungen der erfassten Wellenformen erhöht.

Das Spektrometer wurde in der multizentrischen klinischen Studie "*Lasers4Life*" getestet, um zu untersuchen, wie gut Personen mit Lungen-, Prostata-, Brust- und Blasenkrebs im therapienaiven Zustand anhand von molekularen Infrarot-Fingerabdrücken des Blutplasmas identifiziert werden können. Die Studie wurde in Zusammenarbeit mit Spezialisten des Universitätsklinikums der LMU durchgeführt. Die Blutplasmaproben von mehr als 5.300 Probanden wurden mit dem beschriebenen feldauflösenden Spektrometer analysiert. Das Spektrometer erwies sich als robust genug, um reproduzierbare Messungen in großem Maßstab an klinischen Proben durchzuführen und Personen mit Lungenkrebs von nicht symptomatischen Kontrollpersonen mit einer Genauigkeit von 80% zu unterscheiden. Die Ergebnisse für die anderen Krebsarten waren im Vergleich dazu weniger vielversprechend. Der erfolgreiche Abschluss der ersten groß angelegten klinischen Studie mit einem feldauflösenden Infrarotspektrometer ist ein ermutigendes Zeichen für die Entwicklung eines neuen schnellen, minimal-invasiven Ansatzes zur Überwachung der menschlichen Gesundheit.

Abstract

Human blood plasma comprises a complex mixture of biomolecules. Compared to invasive clinical testing, which is often limited in molecular coverage and depth of analysis, infrared spectroscopy of complex biofluids presents a valuable, minimally invasive, single-measurement diagnostic approach. Several recent studies have explored the efficacy of blood-based infrared molecular fingerprinting to determine the state of an individual's health. Commercially available Fourier transform infrared spectrometers were predominantly applied. However, the limited sensitivity of currently available devices makes it difficult to detect weak infrared absorption. In this thesis, the power of femtosecond laser technology has been harnessed to develop a rapid-scanning field-resolving infrared spectrometer with advantages in sensitivity, timing precision, and throughput, in the hope of improving diagnostic capabilities.

To achieve this, a previously developed Yb:YAG thin-disk laser oscillator emitting 16-fs pulses at a repetition frequency of 28 MHz was utilized to generate few-cycle mid-infrared radiation spanning from 6.5 µm to 11 µm (-20 dB). This thesis demonstrates two new techniques for rapid electro-optic sampling at kHz rates. The first technique used an ultrasonic sonication device called a sonotrode, which vibrates at 19 kHz, to vary optical delay. A fraction of the optical power of the 16-fs pulse is picked off to act as the gate for electro-optic sampling. The gate beam was reflected off the sonotrode to facilitate ultra-rapid delay scanning, with 38,000 traces of the mid-IR waveform acquired per second. In a single scan acquired in 26 µs, an electric-field dynamic range of 150 was achieved, with a timing precision of 34 attoseconds at the zero-crossing points.

The second method involved a dual-oscillator approach, in which the gate pulses for electro-optic sampling were sourced from a second Er:fiber laser oscillator. The relative delay between the mid-infrared and gate pulses was scanned by an electronically controlled modulation of the pulse repetition frequency of the second oscillator with respect to the first. The novel electro-optic delay tracking technique facilitated precise mapping of the relative delay, wherein a narrowband mid-infrared waveform with a known optical frequency was produced as a delay calibration signal and captured using electro-optic sampling. The Er:Fiber laser pulses were split into two, with one part serving as a gate for the delay calibration signal to track the relative delay with high precision and the other gating the broadband mid-IR waveform that came out through the cuvette containing the sample. By modulating the repetition frequency of the Er:Fiber laser at a frequency of 1.4 kHz, traces of the mid-IR waveform are acquired at a rate of 2,800 per second.

Previously reported dual-oscillator spectrometers with sub-femtosecond timing precision have applied a constant offset between the repetition frequencies of the two oscillators. For MHz repetition rates, this corresponds to nanosecond delay ranges well suited to gas phase spectroscopy. Condensed phase spectroscopy, on the other hand, requires much smaller delay ranges on the order of picoseconds due to the shorter dephasing times of the excited molecular vibration states. The dual-oscillator rapid scanning spectrometer with electro-optic delay tracking fills this space by enabling precise scanning of picosecond delays with a much higher duty cycle. For a single scan acquired in 357 µs, a timing precision of 50 attoseconds was achieved at the zero-crossings of the waveform in the delay window with the strongest signal strength. Rapid measurement at kHz rates 'freezes' technical noise in the sub-kHz range and enables the capture of dynamic processes, such as in flow cytometry. For static samples, averaging repeated measurements also enhances the sensitivity of the captured waveforms. Nonlinear spectroscopy techniques, such as pump-probe, photon echo, and coherent anti-stokes Raman scattering, can benefit from the versatile method of electro-optic delay tracking.

The developed instrument was put to the test in the "*Lasers4Life*" multi-centric clinical study to evaluate how accurately individuals with lung, prostate, breast, and bladder cancer could be identified at therapy naïve states from infrared molecular fingerprints of blood plasma. The study, which was conducted in collaboration with specialists at the LMU University Hospital, involved more than 5300 individuals. The blood plasma samples were analyzed over several months using the field-resolving spectrometer described in this thesis. The newly developed device proved robust enough to perform reproducible large-scale measurements on clinical samples, classifying individuals with lung cancer from non-symptomatic control individuals with an accuracy of 80 %. The results for the other cancer types were less promising in comparison. The successful completion of the first large-scale clinical study with a field-resolving infrared spectrometer is an encouraging sign for developing a rapid, minimally-invasive, single-measurement approach to monitoring human health.

List of Publications

Journal publications

- A. Weigel, **P. Jacob**, D. Gröters, T. Buberl, M. Huber, M. Trubetskov, J. Heberle, and I. Pupeza, *"Ultra-rapid electro-optic sampling of octave-spanning mid-infrared waveforms,"* Opt. Express 29, 20747-20764 (2021): *I performed test experiments with the sonotrode delay-scanning approach together with A. Weigel and D. Gröters, and analyzed the measured data with A. Weigel.*

- A. Weigel, **P. Jacob**, W. Schweinberger, M. Huber, M. Trubetskov, P. Karandušovský, C. Hofer, T. Buberl, T. Amotchkina, M. Högner, D. Hahner, P. Sulzer, A. Leitenstorfer, V. Pervak, F. Krausz, I. Pupeza,: *"Dual-oscillator infrared electro-optic sampling with attosecond precision,"* Optica (accepted for publication, 2024): *I implemented dual-oscillator delay scanning in the field-resolving spectrometer together with A. Weigel, performed the experiments with W. Schweinberger, analyzed the data with the support of M. Huber, M. Högner, and M. Trubetskov, prepared the figures, and drafted the text together with A. Weigel, I. Pupeza and M. Huber.*

- M. Huber, M. Trubetskov, W. Schweinberger, **P. Jacob**, M. Zigman, F. Krausz, I. Pupeza, *"Standardized electric-field-resolved molecular fingerprinting,"* in review: *I performed the measurements using the field-resolving spectrometer with W. Schweinberger*

Conference contributions

- **P. Jacob**, A. Weigel, D. Gröters, T. Buberl, M. Trubetskov, M. Huber, J. Heberle, I. Pupeza, *"Mid-infrared waveform measurement by rapid mechanical scanning,"* EPJ Web Conf. 243 16002 (2020)

- A. Weigel, T. Buberl, **P. Jacob**, T. Amotchkina, C. Hofer, M. Trubetskov, P. Sulzer, S. A. Hussain, V. Pervak, F. Krausz, I. Pupeza, *"Attosecond-Precision Dual-Oscillator Infrared Field-Resolved Spectroscopy Employing Electro-Optic Delay Tracking,"* 2021 Conference on Lasers and Electro-Optics Europe & European Quantum Electronics Conference (CLEO/Europe-EQEC).

- T. Amotchkina, M. Trubetskov, A. Weigel, D. Hahner, S. A. Hussain, **P. Jacob**, I. Pupeza, V. Pervak, *"Fabry-Pérot Based Temporal Standard at 8.5 µm for Electro-Optic Delay Tracking,"* 2021 Conference on Lasers and Electro-Optics Europe & European Quantum Electronics Conference (CLEO/Europe-EQEC).

- **P. Jacob**, A. Weigel, W. Schweinberger, T. Buberl, M. Högner, P. Karandušovský, C. Hofer, M. Trubetskov, M. Huber, F. Krausz, and I. Pupeza, *"Precision time-domain spectroscopy of infrared waves,"* in Proceedings of the 2022 Conference on Lasers and Electro-Optics Pacific Rim, Technical Digest Series (Optica Publishing Group, 2022)

Chapter 1

Introduction and Motivation

Health is an essential aspect of human development, and the quest for better health care is universal. This quest requires progress on several fronts, from new medical discoveries to the invention of new devices and tools for medical diagnosis and treatment, new technological approaches that improve affordability and accessibility, and socio-political efforts to break down the barriers to universal health coverage [91, 11, 17]. In addition to the increasing range of medical devices and tests, improvements in computing, data storage and handling, and artificial intelligence are opening up possibilities to efficiently use the information available from multiple diagnostic measurements to provide a more comprehensive description of an individual's health state [18]. The emerging field of personalized medicine [32], which incorporates a person's genetic profile to make individually tailored medical decisions, could be a significant step forward.

The work described in this thesis is part of a wider aim to develop a minimally-invasive and affordable medical test to monitor the state of human health. Our chosen method is infrared spectroscopy of human blood serum and plasma. Several studies in the past have explored the potential of performing infrared spectroscopy on human biofluids for medical diagnostics [6]. Among the biofluids studied are blood serum or plasma [5, 84, 55, 41], urine [63], bile [93], sputum [53], saliva [88], and breath [61, 31]. Infrared spectroscopy can also be extended to personalized clinical decision-making as person-specific molecular fingerprints are stable over time [39]. Most studies have used the well-established technique of Fourier transform infrared (FTIR) spectroscopy.

Ultrafast-laser-based sources of few-cycle mid-infrared (MIR) pulses combined with electric-field-sensitive electro-optic detection offer the advantages of improved dynamic range of detection, as well as temporal confinement of the excitation pulse to a few tens of femtoseconds [76]. This allows the resonant response of the coherently excited molecules to be recorded with reduced noise since it is separated in time from the strong excitation pulse. My colleague Marinus Huber, in his doctoral work [38], introduced the applicability of electro-optic sampling (EOS)-based electric-field molecular fingerprinting of human blood serum/plasma for disease detection. My former colleague Theresa Buberl [13], in her doctoral thesis, developed a femtosecond laser-based field-resolving infrared spectrometer that combines broadband infrared spectral coverage with high dynamic range field-sensitive detection by EOS.

This thesis builds on the work in Ref. [13] by developing and implementing two independent rapid delay-scanning techniques. This reduces the noise, making the individual EOS traces, each acquired in less than a millisecond, immune to laser intensity fluctuations that occur on slower time scales. In addition, rapid delay scanning makes the instrument suitable for high-throughput applications. A first large-scale case-control study has been performed with the instrument, bringing this method a step closer to clinical implementation through the "*Lasers4Life*" clinical study, a prospective, single-time-point, case-control study aimed at evaluating the potential of infrared spectroscopy of human blood plasma for the early detection of cancer.

The remainder of this chapter provides a brief description of spectroscopy and an introduction to the technique of field-resolved spectroscopy used in this work.

1.1 Spectroscopy

It was Sir Isaac Newton who, more than 350 years ago, reported the splitting of white light into its distinct constituent colours, unveiling a 'spectrum' of light for the first time [62]. Later on, in the 19th century, Joseph von Fraunhofer invented the diffraction grating and studied the dark lines in the spectrum of the sun. In the second half of the century, Robert Kirchoff, Robert Wilhelm Bunsen, and Carl August von Steinheil built a spectroscope with a flame acting as its own light source, using it to heat and study the optical spectra arising from various chemical substances. Subsequently, Anders Jonas Ångström studied the spectrum of atomic Hydrogen, the result of which contributed to the development of theories describing the atomic spectral lines by Johann Jakob Balmer and Janne Robert Rydberg [27, 68].

The theories arising from the spectroscopic study of atomic hydrogen proved instrumental in the development of Niels Bohr's atomic model [29], and consequently, together with the study of the spectral characteristics of black body radiation by Max Planck, quantum mechanics began to develop.

Spectroscopy of the hydrogen atom deals with transitions between electronic energy levels. Molecular vibrational spectroscopy relates to transitions in the vibrational levels of molecules, which typically occur in the infrared spectral range from 200 cm^{-1} to 5000 cm^{-1}. A molecule comprising N items has 3N degrees of freedom by virtue of the motion of atoms. Of this, three correspond to the translational motion of the molecule as a whole and 3 to its rotation. In the remaining 3N-6 cases, the molecule's center of mass remains the same, while the relative position and orientations of the atoms in the molecule vary. These are the internal vibrations, the energy levels we seek to measure by vibrational spectroscopy. A detailed account of the molecular vibrational energy levels and the factors affecting them can be found in [65]. The three vibrational modes of a triatomic molecule are depicted in Fig. 1.1 (adapted from Fig. 6.1 in Ref. [65]).

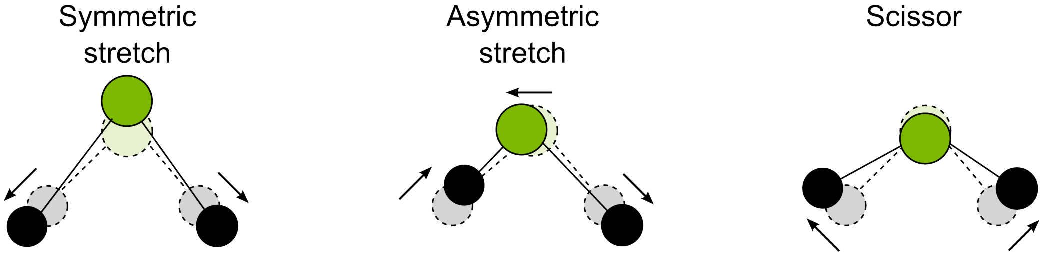

Figure 1.1: Molecular vibrational degrees of freedom

1.1.1 Fourier transform infrared spectroscopy

Most FTIR are based on the Michelson interferometer, where a beam splitter separates an optical beam into two parts. The two beams propagate in two arms and are reflected by mirrors back to the beam splitter, where they are combined by interference. Half of the interferometric signal returns to the source, while a photodetector detects the other half. A movable mirror is used in one of the interferometer's two arms to change the relative delay between the interfering beams. This results in a modulation of the interferometric signal. For a monochromatic incident beam and mirror motion with a constant velocity, the resulting interferometric signal will be sinusoidal, with the modulation frequency of the interferogram being proportional to the optical frequency of the source. For a polychromatic incident beam, the modulation of the interferogram would resemble the superposition of multiple sinusoidal oscillations. A Fourier transform of the interferogram and multiplication by appropriate conversion coefficients would give out the spectrum of the incoming light. This is the basic principle behind Fourier transform spectroscopy. A more detailed description of the instrumentation and properties of FTIR spectrometers can be found in [33]. Fig. 1.2 shows the example of a Michelson interferometer.

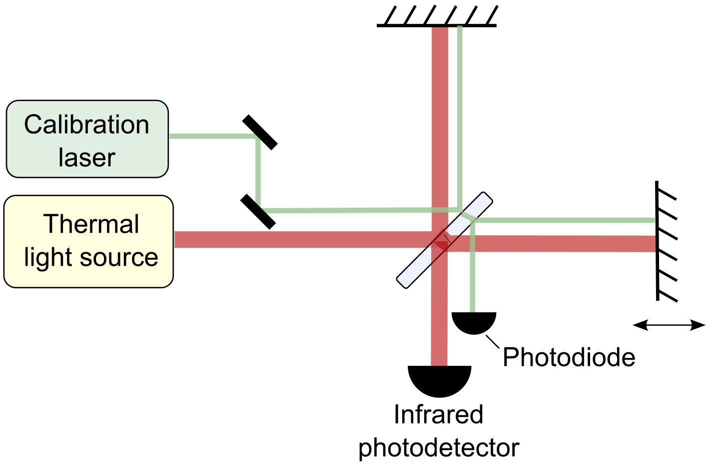

Figure 1.2: Schematic diagram of a Michelson interferometer

Fourier transform spectroscopy has multiple advantages in comparison with conventional spectroscopic methods, where a prism or a grating monochromator is used to spatially split incident light into its spectral components:

- **Multiplexing (Felgett's) advantage:** This deals with the fact that an interferometric measurement has the ability to capture all spectral components simultaneously, while a monochromator with a single detector captures the spectrum one component at a time. Let us say that there are M spectral components that can be resolved. An FTIR spectrometer can capture a spectrum with the same signal-to-noise ratio as a single-detector monochromator spectrometer M times faster. In other words, for measurements taken over the same amount of time, the signal-to-noise in the case of Fourier transform spectroscopy will be $\sqrt{M}$ times larger.

- **Throughput (Jacquinot's) advantage:** The fact that a slit aperture is not required to achieve spectral resolution as is the case for a monochromator results in higher throughput and sensitivity.

While Fourier transform infrared spectrometers are widely used, their sensitivity is still limited.

1.1.2 Field-resolved spectroscopy

Advancements in femtosecond laser technology have helped develop broadband sources of infrared radiation with a brilliance that is orders of magnitude higher than a globar®or even synchrotron beamlines. A comparison of the brilliance and spectral coverage of laser-based sources of mid-infrared radiation can be found in [46]. Laser-based sources also bring in the advantage of spatially and temporally coherent light pulses. For waveform-stable femtosecond infrared pulses, electro-optic sampling can be employed to capture the full information enclosed in the electric field [77], containing the spectral amplitude and the phase.

With a limited number of laser sources in the MIR, frequency down-conversion of visible and near-infrared (NIR) radiation to the MIR by nonlinear optical processes such as difference-frequency generation (DFG) and optical rectification has been a strategy that has been widely used [77, 57, 92]. The invention of the quantum cascade laser [23] brought about a new coherent source of mid-infrared radiation. The further development of tunable quantum cascade lasers has made them a useful tool for mid-infrared spectroscopy in liquid phase [52, 1] as well as gas phase [71, 31]. They, however, have a limited spectral bandwidth.

Compared to direct detection in the mid-infrared, performing electro-optic sampling with frequency conversion from the mid-infrared to the NIR spectral range enables the use of more developed, sensitive, and low-noise detectors widely available in the NIR range. Field-resolved spectroscopy based on electro-optic sampling takes advantage of this fact [76].

Previously presented field-resolving infrared spectrometers [75, 13] require 1-2 seconds to capture a trace of the mid-infrared waveform by scanning picosecond-level optical delays. Variations in laser intensity as well mechanical fluctuations that occur within the time of a scan result in technical noise that limits the sensitivity of a measurement. To tackle this, we introduce two rapid delay-scanning approaches where a single scan is completed in less than a millisecond. This enables sub-kHz noise contributions to be suppressed, and in addition, opens up possibilities for probing dynamic processes. The upgrade of the field-resolved spectrometer to perform rapid scanning is at the heart of this work.

1.2 From concept to clinical study

This thesis demonstrates the upgrade of a proof-of-concept slow-scanning field-resolving spectrometer to a rapid-scanning version. Rapid scanning enables the suppression of fluctuations that occur at a time-scale that is slower than the time required for a single scan. By scanning at kHz rates, we 'freeze' a significant amount of technical noise within each scan. By averaging scans over time, the sensitivity can be increased by a factor of the square root of the number of scans averaged.

Further progress is made in transforming the spectrometer into a device that can be operated by a trained user, with the ability to function consistently over a period of several months. The field-resolving spectrometer is then employed the *Lasers4Life*, done in collaboration with medical specialists at the LMU University Hospital, to test the viability of the device in detecting common cancer phenotypes from the electric-field molecular fingerprints (EMFs) of human blood plasma. In the first phase of the study, blood plasma samples from 5,300 individuals were collected, stored, measured, and analyzed with infrared spectroscopy following a standardized procedure, as will be discussed in Chapter 5.

To our knowledge, it is the first time that such a field-resolving spectroscopic technique has been utilized for a clinical study involving thousands of individuals. This requires the newly developed device to operate in a reproducible and consistent manner over months. The performance of the field-resolved spectrometer is compared with a commercially available Fourier-transform infrared spectrometer, which was previously reported as a promising candidate for the task [41].

The thesis is structured as follows: Chapter 2 is meant to serve as a background for the main concepts and techniques used in this thesis. In Chapter 3, starting with the existing slow-scanning spectrometer, we transition to an ultra-rapid delay scanning scheme that uses an ultrasonic sonication device called a sonotrode. Results of a test experiment with the sonotrode delay-scanning are presented. Chapter 4 describes the concept and experimental implementation of a dual-oscillator approach for electro-optic sampling, where the mid-infrared and gate pulses are sourced from 2 different laser oscillators. The repetition rates of the two oscillators are carefully controlled using an electronic feedback loop. The novel technique of electro-optic delay tracking, which enables precise calibration of the relative delay between the two laser pulse-trains, is presented. In Chapter 5, the field-resolved spectrometer is put to the test in carrying out measurements for the multi-centric case-control clinical study called *Lasers4Life*. The workflow and measures taken to ensure the reliable functioning of the field-resolving spectrometer are highlighted. The results of the case-control study shed light on the robustness of the new spectroscopic approach, guiding future efforts to develop the method further for potential real-world clinical application.

Chapter 2

Background

This chapter aims to bring up physical phenomena, mathematical methods, and previous work in the field that have been utilized or contributed to this thesis. Starting with a brief description of linear and basic non-linear optics, applications of non-linear optics central to this work are introduced, namely intra-pulse difference frequency generation and electro-optic sampling, for the generation and field-resolved detection of mid-infrared optical radiation, respectively. This leads to the topic of infrared spectroscopy, touching on the well-established technique of Fourier Transform Infrared Spectroscopy, as well as femtosecond-laser-based field-resolved infrared spectroscopy, which our research group has been working on over the past few years.

This work applies infrared spectroscopy of human blood plasma for disease detection, using machine-learning-based pattern recognition to classify the spectra. The remaining part of the chapter introduces concepts used to build or train a binary classifier and the parameters used to quantify classification efficiency.

2.1 Maxwell's equations

The nature of light has been a topic of study over centuries. In the latter part of the 19th century, James Clerk Maxwell proposed the nature of light as we know it today, as an electromagnetic wave. Building upon observations made in the past generations on light's properties and connecting them to more recent discoveries in electricity and magnetism, Maxwell came up with an elegant set of equations relating the electric field (E) and magnetic field (H), that accurately describe the propagation of light in vacuum, which is highly significant and useful even today. The equations are represented as follows:

$$\nabla \times E = -\mu_0 \frac{\partial H}{\partial t}, \tag{2.1}$$

$$\nabla \times H = \epsilon_0 \frac{\partial E}{\partial t}, \tag{2.2}$$

$$\nabla \cdot E = 0, \tag{2.3}$$

$$\nabla \cdot H = 0. \tag{2.4}$$

Here, ϵ and μ refer to the permittivity and permeability of the medium of propagation, with the subscript 0 referring to vacuum.

To obtain an equation with solely the electric field, we take the curl of Eq. 2.1:

$$\nabla \times (\nabla \times E) = \nabla \times \left(-\mu_0 \frac{\partial H}{\partial t}\right). \tag{2.5}$$

Making use of the following vector identity [22]:

$$\nabla \times (\nabla \times A) = \nabla(\nabla \cdot A) - \nabla^2 A, \tag{2.6}$$

,

and substituting it in 2.5, we obtain:

$$\nabla(\nabla \cdot E) - \nabla^2 E = \epsilon_0 \frac{\partial(\nabla \times H)}{\partial t}. \tag{2.7}$$

Now, substituting for $\nabla \cdot E$ and $\nabla \times H$ using Eq. 2.3 and 2.2, we have:

$$-\nabla^2 E = -\mu_0 \epsilon_0 \frac{\partial^2 E}{\partial t^2}$$

$$\implies \nabla^2 E - \mu_0 \epsilon_0 \frac{\partial^2 E}{\partial t^2} = 0. \tag{2.8}$$

Eq. 2.8 represents the electromagnetic wave equation, also know as the *Helmholtz wave equation* in vacuum. Any function in the form $E(z - c_0 t)$ with a constant factor c would solve the equation, from which we obtain the speed of light in vacuum,

$$c_0 = \frac{1}{\sqrt{\epsilon_0 \mu_0}} = 2.998 \times 10^8 m/s \tag{2.9}$$

In a real medium, the Maxwell equations, accounting for current (J) and charge densities (ρ) in the medium, as well as its electromagnetic properties, become the following:

$$\nabla \times E = -\mu \frac{\partial H}{\partial t}, \tag{2.10}$$

$$\nabla \times H = J + \epsilon \frac{\partial E}{\partial t} \tag{2.11}$$

$$\nabla \cdot E = \frac{\rho}{\epsilon}. \tag{2.12}$$

$$\nabla \cdot H = 0. \tag{2.13}$$

Here, μ refers to the magnetic permeability of the medium, and ϵ, to the permittivity of the medium of propagation. The speed of light in any medium depends on the value of these parameters.

$$c = \frac{1}{\sqrt{\epsilon\mu}} \triangleq \frac{c_0}{n}, \tag{2.14}$$

where the refractive index of a medium is calculated as the ratio of the speed of light in vacuum to the speed of light in the medium.

For non-magnetic materials, $\mu = \mu_0$. Thus we get:

$$n = \sqrt{\frac{\epsilon}{\epsilon_0}} = \sqrt{\kappa}, \tag{2.15}$$

where κ is the dielectric constant, which will be discussed in the following section.

2.2 Linear optics

As a precursor to Maxwell, Michael Faraday had developed the concept of the electric field lines of force. He also famously studied the effect that inserting different insulating materials between the charged capacitor plates has on the capacitance. He observed that the capacitance increased by a material-dependent factor, which came to be called the dielectric constant, κ. This increase in capacitance was explained to be due to the formation of electric dipoles within the dielectric. The dipoles aligned in an opposing manner to the electric field induced by the charged plates. This decreased the effective electric field inside the dielectric, allowing a higher charge to be stored in the capacitor when a fixed voltage was assigned.

The electric polarization vector, P, is defined as the electric dipole moment per unit volume generated in the dielectric material by the external electric field.

$$P = Nq\delta, \tag{2.16}$$

where N is the density of atoms, and a charge q is separated by a distance δ in each atom.

In the simplest case, P is assumed to be linearly proportional to E, i.e,

$$P = \epsilon_0 \chi E, \tag{2.17}$$

where χ is the constant of proportionality. This implies that adding a dielectric increases capacitance by a factor $(1 + \chi)$, where:

$$\kappa = 1 + \chi \tag{2.18}$$

This assumption holds in most cases in everyday life. The induced polarization, P, and hence the optical response, scales linearly with the strength of the applied electric field. This describes linear optics.

Combining Eq. 2.9 with Eq. 2.8, we get:

$$\nabla^2 E - \frac{1}{c_0^2}\frac{\partial^2 E}{\partial t^2} = 0, \tag{2.19}$$

for light propagating in vacuum.

For a dielectric medium, assuming that linear optics holds true, we obtain a similar equation:

$$\nabla^2 E - \frac{1}{c^2}\frac{\partial^2 E}{\partial t^2} = 0, \tag{2.20}$$

with the only difference being an adjustment in the speed of light:

$$c = \frac{c_0}{\sqrt{1 + \chi}} \tag{2.21}$$

In truth, however, P does not have a linear relationship with E. The deviation from the linear approximation is usually noticed only for an electric field strength $>10^6 V/cm$ when it becomes comparable to the atomic field strength, E_{at}, given by:

$$E_{at} = \frac{e}{4\pi\epsilon_0 a_0^2} = 5.14 \times 10^9 V/cm. \tag{2.22}$$

Here, e refers to the charge of an electron, ϵ_0, the permittivity of free space, and a_0, the Bohr radius of the Hydrogen atom. The invention of the laser and advances in laser technology in the second half of the last century [19] made it possible to observe various effects relating to this nonlinear relationship, hence opening up the field of nonlinear optics.

2.3 Nonlinear optics

Soon after the conception [79] and first demonstration [60] of a laser, researchers started observing new phenomena, such as the generation of optical harmonics[26], resulting in the realization that the electric polarization is not linearly dependent on the electric field. This proved wrong the assumption of the susceptibility (χ) being a constant linear coefficient, implying a complex relationship with the electric field, which, in the simplified assumption of an instantaneous response, can be expressed as a Taylor series:

$$P = \epsilon_0(\chi^{(1)}E + \chi^{(2)}E^2 + \chi^{(3)}E^3 + ...) \tag{2.23}$$

Eq. 2.23 can be represented in the following form as well:

$$P = P^{(1)} + P^{(2)} + P^{(3)} + ... = P^{(1)} + P^{NL}, \tag{2.24}$$

where $P^{(1)}$ corresponds to the linear part, and P^{NL} to the non-linear part of the polarization.

$$\tilde{P^{(1)}} = \epsilon_0\chi^{(1)}\tilde{E}, \tag{2.25}$$

$$P^{(\tilde{NL})} = \epsilon_0(\chi^{(2)}\tilde{E}^2 + \chi^{(3)}\tilde{E}^3 + ...) \tag{2.26}$$

The *Helmholtz wave equation* changes to the following:

$$\nabla^2 E - \frac{n^2}{c_0^2}\frac{\partial^2 E}{\partial t^2} = \frac{1}{\epsilon_0 c_0^2}\frac{\partial^2 P^{(NL)}}{\partial t^2}. \tag{2.27}$$

Here, n represents the linear refractive index. In the following sections, we shall describe a few nonlinear optical processes, following the flow of thought and notation in Ref. [10].

2.3.1 Second-order nonlinear processes

Let us represent the electric field strength of a laser beam at a particular point in space as follows:

$$\tilde{E}(t) = Ee^{-i\omega t} + c.c., \tag{2.28}$$

where c.c. stands for complex conjugate.

If we now consider the leading (second-order) term of the non-linear polarization, $\tilde{P}^{(NL)}(t)$, which we shall call $\tilde{P}^{(2)}(t)$, we get:

$$\tilde{P}^{(2)}(t) = 2\epsilon_0\chi^{(2)}\tilde{E}^2(t) = \epsilon_0\chi^{(2)}|E|^2 + (\epsilon_0\chi^{(2)}E^2e^{-2i\omega t} + c.c). \tag{2.29}$$

Thus, the second-order polarization term transforms a single incident frequency of electromagnetic radiation into a static electric field and a field oscillating at twice the frequency. These processes are called optical rectification and second harmonic generation (SHG), respectively. The formation of the second harmonic of a laser beam was the first reported nonlinear optical effect six decades ago [26]. The SHG process can be pictured as two photons of the same frequency being converted into a single photon with twice the frequency, thus conserving energy. Having already considered the case of a single frequency of incident light, we shall look into the case of having radiation at two frequencies.

Consider an incident electric field strength given by:

$$\tilde{E}(t) = E_1 e^{-i\omega_1 t} + E_2 e^{-i\omega_2 t} + c.c., \tag{2.30}$$

This gives us:

$$\begin{aligned}\tilde{P}^{(2)}(t) = \epsilon_0 \chi^{(2)}[2|E_1|^2 + 2|E_2|^2 + (E_1^2 e^{-2i\omega_1 t} + E_2^2 e^{-2i\omega_2 t} \\ + 2E_1 E_2 e^{-i(\omega_1+\omega_2)t} + 2E_1 E_2^* e^{-i(\omega_1-\omega_2)t} + c.c)].\end{aligned} \tag{2.31}$$

While the first four terms refer to optical rectification (static electric fields) and second harmonic generation (ω_1 and ω_2) as described above, two terms have newly emerged, the generation of the sum ($\omega_1 + \omega_2$) and difference ($\omega_1 - \omega_2$) frequencies. The two processes referred to as sum-frequency generation (SFG) and DFG are of great interest to us and have been applied in this thesis.

2.3.2 Third-order nonlinear processes

In the previous subsection, we looked at the leading term of the nonlinear polarization, which is proportional to E^2. If we now look at the next term, where the polarization scales with E^3, many new possibilities arise. For simplicity, we consider the case where the incident light is monochromatic. This gives us the following expression for the third-order polarization.

$$P^{(3)} = \epsilon_0 \chi^{(3)} (E^3 e^{-i3\omega t} + 3|E|^2 E e^{-i\omega t} + c.c) \tag{2.32}$$

Here, the first term represents the third harmonic generation (THG), where a new frequency component thrice the incident radiation frequency emerges from the crystal. The second term consists of radiation at the same frequency as the incident but with the extent of polarization proportional to the intensity of incident radiation. This leads to an intensity-dependent refractive index, n_2. Substituting for $P^{(1)}$ and $P^{(3)}$ in Eq. 2.23, and collecting the terms that oscillate at the same frequency as the incident radiation, we get:

$$P = \epsilon_0(\chi^{(1)} + 3\chi^{(3)}|E|^2) \tag{2.33}$$

Combining Eq. 2.15 and Eq. 2.18, we obtain the following:

$$n^2 = 1 + \chi^{(1)} + 3\chi^{(3)}|E|^2 \tag{2.34}$$

If we represent n as a sum of the constant linear refractive index and an intensity-dependent non-linear refractive index, as,

$$n = n_0 + n_2|E|^2, \tag{2.35}$$

Eq. 2.34 implies,

$$n_0^2 + 2n_0n_2|E|^2 + n_2^2|E|^4 = 1 + \chi^{(1)} + 3\chi^{(3)}|E|^2. \tag{2.36}$$

Assuming the value of n_2^2 to be insignificant compared to n_0, we neglect the last term to obtain:

$$n_2 = \frac{3\chi^{(3)}}{2n_0} \tag{2.37}$$

The value of $\chi^{(3)}$ for Si is around $10^{-18} m^2/V^2$, and that for glass is even lower, of the order of $10^{-22} m^2/V^2$ [10]. Although relatively small, the intensity-dependent change in the refractive index can have significant effects.

Self-focusing:

When a sufficiently intense light beam with a non-uniform spatial profile passes through a material, the intensity-dependent refractive index caused by the $\chi^{(3)}$ susceptibility results in transverse sections of the beam experiencing different refractive indices. Light travels at different speeds along the sections of the beam profile. In a beam that is more intense at the centre than at the edges, this results in a converging effect. The fact that light travels slower at the centre than at the edges causes the beam to focus, as if it was passing through a convex lens. This phenomenon is called self-focusing [47, 66].

Self-phase modulation:

Another effect of an intensity-dependent refractive index is observed when working with ultrashort pulses of intense laser light. Here, let us consider the non-uniform temporal distribution of electric field strength. The temporal variation in the intensity envelope of a short pulse results in a different refractive index at different points in time as the pulse propagates through the medium. This works out as an effective time-dependent shift in the optical phase of the pulse and is referred to as self-phase modulation. These phase shifts result in changes in the instantaneous frequency of oscillation along the temporal profile of an ultra-short pulse, leading to the generation of new spectral components and the suppression of existing ones [85, 67]. Thus, self-phase modulation becomes a useful technique to broaden the spectrum of an ultra-short laser pulse.

2.3.3 Phase-matching

We have seen above how multiple potential non-linear optical processes could take place from the effect of the second and third-order optical susceptibility. All of the processes described above conserve energy. Take the case of SHG, for example. Two photons of frequency ω_1 are converted to a single photon of frequency $\omega_2 = 2\omega_1$, which has twice the energy as each of the two absorbed photons. The energy conservation can be shown as follows:

$$\hbar\omega_2 = 2\hbar\omega_1 \tag{2.38}$$

For the nonlinear process to take place efficiently, momentum should also be conserved, that is,

$$\hbar\vec{k}_2 = 2\hbar\vec{k}_1, \tag{2.39}$$

where $\vec{k}_1$ and $\vec{k}_2$ represent the wave-vectors for the incident and generated second harmonic radiation, respectively. Assuming the same direction of propagation, let us look at only the magnitude of the wave-vector, $|\vec{k}|$ for simplicity.

$$|\vec{k}|= \frac{n(\omega)\omega}{c_0}, \tag{2.40}$$

where $n(\omega)$ is the refractive index, and c_0 is the speed of light in vacuum.

Combining Eq. 2.39 and Eq. 2.40, momentum conservation boils down to the refractive index $n(\omega)$ remaining a constant. Due to dispersion, this turns out not to be the case.

One way to obtain phase-matching makes use of the property of birefringence, wherein the refractive index depends on the polarization direction. For demonstration purposes, let us consider the crystal to portray negative birefringence, that is, the refractive index of extraordinary (e) light is lower than that of ordinary (o) polarized light. Let light travel along the z-axis in the crystal, and let the horizontal (x-z) plane represent the plane of incidence. We place the birefringent nonlinear crystal in such a way that the optic axis lies in the x-z plane and can be rotated about the vertical (y) axis.

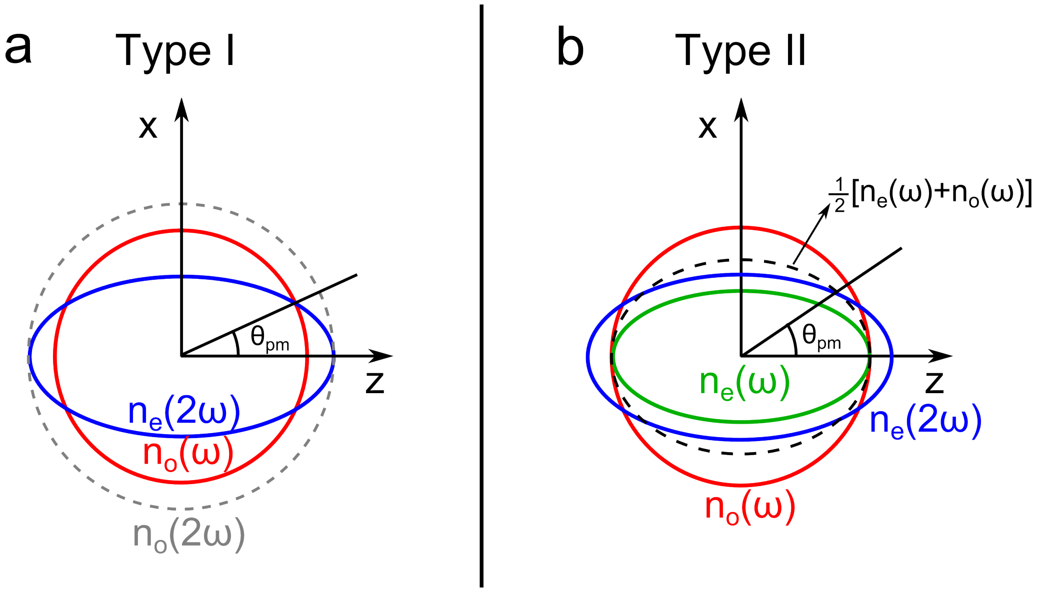

Figure 2.1: Type-I (left) and type-II (right) birefringent phase-matching for second harminic generation in a non-linear crystal exhibiting negative birefringence and normal dispersion.

Figure 2.1 depicts type-I (left) and type-II (right) birefringent phase matching for SHG, taking the example of a negative birefringent crystal showcasing normal dispersion. Normal dispersion implies that the refractive index increases monotonically with the optical frequency. In type-I phase-matching, the two interacting photons of frequency ω have the same polarization (s-polarization, in this case), while the generated second harmonic is orthogonally (p-) polarized. S-polarized light experiences the higher ordinary refractive index, (n_0). The p-polarized light experiences an angle-dependent refractive index, n_e that lies between the ordinary and nominal extraordinary indices, n_o and $\bar{n_e}$, given by:

$$\frac{1}{n_\mathrm{e}^2(\theta)} = \frac{\sin^2(\theta)}{\bar{n_\mathrm{e}}^2} + \frac{\cos^2(\theta)}{n_\mathrm{o}^2}. \tag{2.41}$$

Here, θ represents the angle between the optic axis of the crystal and the z-axis. The ordinary refractive index for light at the fundamental frequency, $n_\mathrm{o}(\omega)$ is shown in red, and the extraordinary refractive index for the second harmonic, $n_\mathrm{e}(2\omega)$ is shown in blue. By rotating the crystal, we tune the refractive index of the p-polarized light until the system is phase-matched. Phase matching occurs for the angle at which the equation, $n_\mathrm{e}(2\omega, \theta) = n_\mathrm{o}(\omega)$ is satisfied, represented by θ_pm in Fig. 2.1.

In type-II phase-matching, the two interacting photons have orthogonal polarization directions. The refractive indices, $n_o(\omega)$ and $n_e(\omega,\theta)$ are shown in red and green on the right panel of Fig. 2.1. In the case of a negative birefringent crystal, as is in our example, the generated second-harmonic experiences the extraordinary refractive index, $n_e(2\omega)$, shown in blue. Phase matching occurs at the angle where the following equation holds:

$$n_{\mathrm{e}}(2\omega,\theta) = \frac{1}{2}\left[n_{\mathrm{e}}(\omega,\theta) + n_{\mathrm{o}}(2\omega)\right]. \tag{2.42}$$

2.3.4 Applications of non-linear optics

Intra-pulse difference frequency generation

The second-order non-linear process of difference frequency generation is a useful technique for generating mid-infrared optical radiation. In the special case where we have a broadband NIR pulse whose spectrum spans thousands of wavenumbers, there exists the possibility of different frequency components from the same pulse from the two ends of the spectrum interacting to generate their difference frequency in the mid-infrared. This process is referred to as intra-pulse difference frequency generation (IPDFG) [77], or optical rectification [44]. Fig. 2.2 is a simplified schematic showing the process of IPDFG, with the green bar representing the incident spectrum from which the DFG spectrum depicted by the grey bar is created. A pair of spectral components within the incident spectrum, which we shall represent by ω_2 and ω_3 interact to generate a new spectral commponent ω_1, in the grey bar. The DFG spectrum potentially spans from the origin to a frequency or wavenumber characterised by the largest difference obtained between the spectral components ω_2 and ω_3 in the incident spectrum. We thus represent this as:

$$\omega_{1,\mathrm{max}} = \omega_{3,\mathrm{max}} - \omega_{2,\mathrm{min}}, \tag{2.43}$$

where $\omega_{3,max}$ and $\omega_{2,min}$ represent the ends of the incident spectrum, denoting the maximum and minimum wavenumber/frequency values for ω_2 and ω_3. In reality, the generated DFG spectrum is further restricted in range due to limitations in phase matching, as well as in transparency of the non-linear crystal.

In DFG, the frequency and the phase of two spectral components are subtracted. When the two spectral components originate from a single mode-locked laser, the phase of the two spectral components vary by the same amount from pulse to pulse, causing the newly generated pulse to have a passively stabilized waveform [14, 81, 45], which is key in our application.

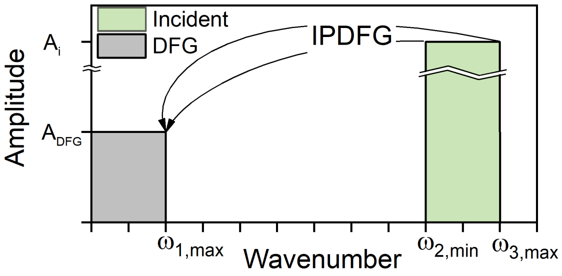

Figure 2.2: Simplified schematic diagram showing intra-pulse difference frequency generation. Spectral components from the two ends of the incident spectrum (green) interact by a second-order nonlinear process to generate frequency components corresponding to their frequency difference (grey)

Electro-optic Sampling

The technique of EOS, which makes use of the second-order non-linear optical process of either sum or difference frequency generation, enables optical waveforms to be measured with high sensitivity. By sequentially sampling the infrared waveform using a sub-infrared-cycle gate beam that is variably delayed, the field-sensitive detection of the temporal evolution of the sampled waveform is achieved. The sampled waveform must have a stable optical phase. The infrared and gate beams are spatially overlapped to perform EOS and focused onto a nonlinear crystal with a second-order nonlinear susceptibility. The incident infrared pulse is polarized orthogonal to the gate pulse. The sum frequency of the gate and the infrared pulses is created, with polarization orthogonal to the gate pulse. The part of the frequency signal that overlaps spectrally with the gate signal superposes to cause a rotation in its polarization. This polarization rotation on the gate signal, which acts as a local oscillator (LO), is measured using a balanced optical heterodyne detection setup to obtain an output that is proportional to the infrared electric field. The setup comprises a quarter-wave plate (QWP), Wollaston prism, and balanced photodetectors after the nonlinear crystal, as shown in Fig. 2.3. A mathematical description is detailed below, following from Ref. [37].

To describe the polarization rotation and heterodyne detection process, we make use of Jones calculus. It is a very convenient and useful formalism discovered by R. Clark Jones in 1941 to express the polarization of light in the form of a normalized 2-component vector with horizontal and vertical linear polarization states as basis vectors. Table 2.1 represents the Jones vectors for common polarization states (adapted from Table 2.1 in Ref. [7]).

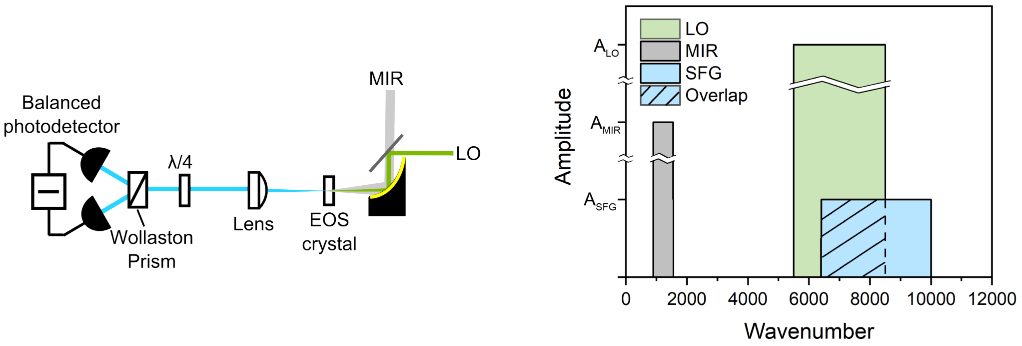

Figure 2.3: (a) EOS setup (b) Interaction between SFG and LO spectra in the overlap region

In Jones calculus, the effect of optical elements on the polarization of a beam that passes through is compared to multiplication by the Jones matrix corresponding to the optical element. The Jones matrix depends on the orientation of the optical element. A few of the most commonly used Jones matrices are depicted in Table 2.2, which has been adapted from Table 2.2 in Ref. [7].

Let us come back to describing the EOS process. We shall be following the treatment in [37]. Let $\tilde{E}_{LO}$ and $\tilde{E}_{MIR}$ represent the *s*- and *p*-polarized gate (local oscillator) and mid-infrared waveforms. Second order non-linear interaction in the EOS crystal generates a p-polarized sum frequency signal, $\tilde{E}_{SFG}$. For simplicity, let us assume that the fields have a constant amplitude and phase across the entire spectral range, giving:

$$\tilde{E}_{LO} = A_{LO} e^{-i\varphi_{LO}}, \tag{2.44}$$

$$\tilde{E}_{\mathrm{MIR}} = A_{\mathrm{MIR}} e^{-i\varphi_{\mathrm{MIR}}}, \tag{2.45}$$

$$\tilde{E}_{SFG} = A_{SFG} e^{-i\varphi_{SFG}}, \text{with} \tag{2.46}$$

$$A_{\mathrm{SFG}} \propto A_{\mathrm{LO}} \cdot A_{\mathrm{MIR}}, \text{and} \tag{2.47}$$

$$\varphi_{\mathrm{SFG}} = \varphi_{\mathrm{LO}} + \varphi_{\mathrm{MIR}} \tag{2.48}$$

The Jones vectors can be represented as follows:

$$\tilde{\mathbf{E}}_{\mathrm{LO}} = \begin{pmatrix} 0 \\ \tilde{E}_{\mathrm{LO}} \end{pmatrix}$$

$$\tilde{\mathbf{E}}_{\mathrm{SFG}} = \begin{pmatrix} \tilde{E}_{\mathrm{SFG}} \\ 0 \end{pmatrix}$$

Polarization	Jones vector
Horizontal	$\begin{pmatrix}1\\0\end{pmatrix}$
Vertical	$\begin{pmatrix}0\\1\end{pmatrix}$
+45°linear	$\frac{1}{\sqrt{2}}\begin{pmatrix}1\\1\end{pmatrix}$
-45°linear	$\frac{1}{\sqrt{2}}\begin{pmatrix}1\\-1\end{pmatrix}$
θ° linear	$\begin{pmatrix}\text{cos}\theta\\\text{sin}\theta\end{pmatrix}$
Left circular	$\frac{1}{\sqrt{2}}\begin{pmatrix}1\\i\end{pmatrix}$
Right circular	$\frac{1}{\sqrt{2}}\begin{pmatrix}1\\-i\end{pmatrix}$

Table 2.1: Jones vectors

The superposition of the two is represented by:

$$\tilde{\mathbf{E}}_{\text{het}} = \begin{pmatrix}\tilde{E}_{\text{SFG}}\\\tilde{E}_{\text{LO}}\end{pmatrix}$$

The beam superposition is then passed through a $\frac{\lambda}{4}$ plate with its fast axis set at 45 °with respect to the horizontal to project the polarizations onto a common axis. Applying the Jones matrix for the $\frac{\lambda}{4}$ plate, from Table 2.2, we get the following:

$$\tilde{\mathbf{E}}_{\text{het,mix}} = \frac{1}{\sqrt{2}}\begin{pmatrix}1 & -i\\-i & 1\end{pmatrix}\cdot\begin{pmatrix}\tilde{E}_{\text{SFG}}\\\tilde{E}_{\text{LO}}\end{pmatrix} = \frac{1}{\sqrt{2}}\begin{pmatrix}\tilde{E}_{\text{SFG}} - i\tilde{E}_{\text{LO}}\\-i\tilde{E}_{\text{SFG}} + \tilde{E}_{\text{LO}}\end{pmatrix} \tag{2.49}$$

Optical element	Jones matrix
Horizontal polarizer	$\begin{pmatrix}1 & 0\\0 & 0\end{pmatrix}$
Vertical polarizer	$\begin{pmatrix}0 & 0\\0 & 1\end{pmatrix}$
Polarizer at angle θ	$\begin{pmatrix}\text{cos}^2\theta & \text{cos}\theta\text{sin}\theta\\\text{cos}\theta\text{sin}\theta & \text{sin}^2\theta\end{pmatrix}$
$\lambda/4$ plate with fast axis at 45°	$\frac{1}{\sqrt{2}}\begin{pmatrix}1 & -i\\-i & 1\end{pmatrix}$

Table 2.2: Jones matrices

The two polarization components are split into two separate beams by the Wollaston prism with the electric field strengths given by:

$$|\tilde{\mathbf{E}}_{\mathbf{1}}|= |\tilde{E}_{\text{het,mix,x}}|= \frac{1}{\sqrt{2}}|\tilde{E}_{\text{SFG}} - i\tilde{E}_{LO}| \tag{2.50}$$

$$|\tilde{\mathbf{E}}_{\mathbf{2}}|= |\tilde{E}_{\text{het,mix,x}}|= \frac{1}{\sqrt{2}}|-i\tilde{E}_{\text{SFG}} + \tilde{E}_{LO}| \tag{2.51}$$

The intensity of the two beams $I_1 = |\tilde{\mathbf{E}}_{\mathbf{1}}|^2$ and $I_2 = |\tilde{\mathbf{E}}_{\mathbf{2}}|^2$ are given as follows:

$$I_1 = \frac{1}{2}\left(A_{\text{SFG}}^2 + A_{\text{LO}}^2 + A_{\text{SFG}}A_{\text{LO}}(e^{-i\varphi_{\text{SFG}}+i\varphi_{\text{LO}}+i\frac{\pi}{2}} + e^{+i\varphi_{\text{SFG}}-i\varphi_{\text{LO}}-i\frac{\pi}{2}})\right). \tag{2.52}$$

Substituting for φ_{SFG} from Eq. 2.48, we get

$$I_1 = \frac{1}{2}\left(A_{\text{SFG}}^2 + A_{\text{LO}}^2 + A_{\text{SFG}}A_{\text{LO}}(e^{-i\varphi_{\text{MIR}}+i\frac{\pi}{2}} + e^{+i\varphi_{\text{MIR}}-i\frac{\pi}{2}})\right)$$

$$\implies I_1 = A_{\text{SFG}}^2 + A_{\text{LO}}^2 + A_{\text{SFG}}A_{\text{LO}}\text{cos}(\frac{\pi}{2} - \varphi_{\text{MIR}})$$

$$\implies I_1 = A_{\text{SFG}}^2 + A_{\text{LO}}^2 + A_{\text{SFG}}A_{\text{LO}}\text{sin}(\varphi_{\text{MIR}}) \tag{2.53}$$

Similarly, we get

$$I_2 = \frac{1}{2}\left(A_{\text{SFG}}^2 + A_{\text{LO}}^2 + A_{\text{SFG}}A_{\text{LO}}(e^{-i\varphi_{\text{SFG}}-i\varphi_{\text{LO}}+i\frac{\pi}{2}} + e^{+i\varphi_{\text{SFG}}+i\frac{\pi}{2}-i\varphi_{LO}})\right). \tag{2.54}$$

$$\implies I_2 = \frac{1}{2}\left(A_{\text{SFG}}^2 + A_{\text{LO}}^2 + A_{\text{SFG}}A_{\text{LO}}(e^{-i\varphi_{\text{MIR}}-i\frac{\pi}{2}} + e^{+i\varphi_{\text{MIR}}+i\frac{\pi}{2}})\right)$$

$$\implies I_2 = A_{\text{SFG}}^2 + A_{\text{LO}}^2 + A_{\text{SFG}}A_{\text{LO}}\text{cos}(\frac{\pi}{2} + \varphi_{\text{MIR}})$$

$$\implies I_1 = A_{\text{SFG}}^2 + A_{\text{LO}}^2 - A_{\text{SFG}}A_{\text{LO}}\text{sin}(\varphi_{\text{MIR}}) \tag{2.55}$$

The balanced photodetector performs subtraction of the intensities, giving:

$$\Delta I = I_1 - I_2 = 2A_{\text{SFG}}A_{\text{LO}}\text{sin}(\varphi_{\text{MIR}}). \tag{2.56}$$

Comparing with Eq. 2.47, we get

$$\Delta I \propto A_{\text{LO}}^2 A_{\text{MIR}}\text{sin}(\varphi_{\text{MIR}}), \tag{2.57}$$

thus resulting in an intensity measurement that is proportional to the infrared waveform.

2.4 Statistics: Allan variance

The Allan variance is a statistical quantity developed by David W. Allan in the 1960s to estimate the frequency stability of atomic clocks[2]. In measuring the frequency fluctuations of an atomic clock, he realized that the standard variance does not always converge, especially in the presence of drifts or a random-walk process. The standard deviation of a variable y, measured in an adjacent series is given as follows:

$$\sigma^2_{\mathrm{y,std}} = \frac{1}{\mathrm{N}-1}\sum_{i=1}^{\mathrm{N}}(y_i - \bar{y})^2, \tag{2.58}$$

where N is the total number of samples, y_i denotes an individual sample, and $\bar{y}$, the mean value of y. In the case of drifts, the mean value does not remain constant for an infinitely long period of time, resulting in the $\sigma^2_{\mathrm{y,\ std}}$ degrading for an increasing number of samples.

Allan's idea was to look at differences in the adjacent spectrum instead of comparing it with the mean. The Allan variance is represented as follows:

$$\sigma^2_{\mathrm{y,Allan}} = \frac{1}{2(\mathrm{M}-1)}\sum_{j=1}^{\mathrm{M\text{-}1}}(\bar{y}_{\mathrm{j+1}} - \bar{y}_{\mathrm{j}})^2. \tag{2.59}$$

Here, the N samples have been divided into M sets with an equal number of samples, with $\bar{y}_{\mathrm{j}}$ representing the mean of the y values in set j. The square root of the Allan variance is called the Allan deviation, $\sigma_{\mathrm{y,Allan}}$. The Allan deviation is calculated for different values of M, that is different sizes of the set over which y is averaged. Fig. 2.4 shows a schematic of the Allan variation calculated for different numbers of samples to be averaged.

The concept of the Allan deviation will be used in evaluating the stability of the infrared waveforms measured using two different rapid-scanning field-resolved spectroscopic approaches in Chapters 3 and 4.

2.5 Machine learning and classification

Statistical learning involves gaining insight or understanding from the available data. Mankind has come far in this over the centuries, performing varied experiments, and making meaningful inferences from available data. There is however a limit on how much data a human can take in and make inferences from, in a time-bound scenario. The advent of computers has enabled humans to process larger amounts of data, by outsourcing mathematical operations to be performed on the data to a computer, in the form of well-defined steps.

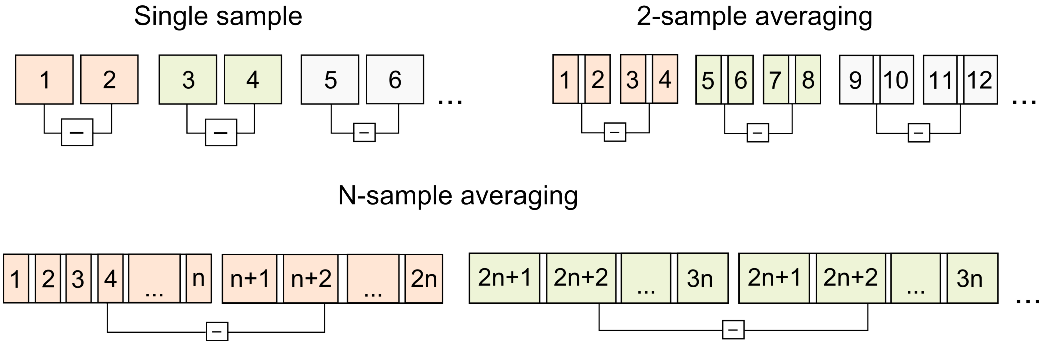

Figure 2.4: Allan variance for different averaging sets. In the single sample case (top left), differences are calculated between adjacent pairs of individual samples. For the 2-sample averaging case (top right), a set of 2 samples are averaged, and the mean is subtracted from the mean of the next set. For the case of n-sample averaging (bottom), the same is performed, taking the average of n samples in each batch, before subtracting the means of subsequent batches.

In many real-life situations, however, it is not easy to explicitly describe the solution of the problem in a series of clear steps. Let us consider cooking food as an example. An aspiring cook can follow an explicitly described recipe to create something delicious. However, the author of a recipe cannot write a new recipe by following a set of instructions. It is years of experience, and a vivid imagination, of what kind of tastes match well together, that enable them to come up with a culinary marvel. Similarly, if a computer's task goes beyond performing predefined steps, to making inferences from previously recorded data, that is if the data enables the computer to solve a problem better, the machine is said to have 'learned' from it. This is referred to as *'machine learning'*

We shall look into the simplest form of learning from data, that is a linear model, where the output or inference is made from a linear combination of the input parameters or input data. Starting with a recap on linear regression, we shall take a look at two linear techniques used to perform binary classification. The receiver operating characteristic curve is presented as a tool to evaluate the performance of a binary classifier. Later on, in Chapter 5, the receiver operating characteristic will be used to test the accuracy of the binary classifier for categorizing infrared spectra of human blood plasma for the most widely prevalent cancer phenotypes.

2.5.1 Linear regression

A linear regression task aims to develop a linear relationship between one or more input parameters and an output parameter in a way that most accurately describes a given data set. Thus, we express the output parameter as a linear superposition of the input parameters. The role of the model is to determine the coefficients of the linear combination, and the quality of fit is determined by how much the predicted values from the linear superposition deviate from the actual values of the output parameter. If we have m data points of the form

$$z_i = (x_{1,i}, x_{2,i}, ..., x_{n,i}, y_i) \tag{2.60}$$

, with i going from 1 to m, the linear regression model can be represented as follows:

$$y_{pred}(z) = a_1x_1 + a_2x_2 + a_3x_3 + ... + a_nx_n + b, \tag{2.61}$$

where $a_1, a_2, a_3, ..., a_n, b$ are the coefficients describing the regression model. A commonly used measure of how well the model corresponds to the data is the mean squared error, which we shall call the cost (C), and is given as follows:

$$C = \sum_{i=1}^{m} \left[y_i - y_{\text{pred}}(z_i)\right]^2 . \tag{2.62}$$

The linear regression task is then simplified to adjusting the values of coefficients $a_1, a_2, a_3, ..., a_n$, and b, so as to minimize C.

For simplicity in visualization, let us consider the case where there is just one input parameter, i.e., $m = 1$. Fig. 2.5(a) shows a sample data set (blue squares) and the fit obtained by linear regression (red line). The line is given by:

$$y_{\text{pred}}(x) = ax + b \tag{2.63}$$

There are several ways to obtain values for the slope and intercept of the regression line, a and b. We shall look into one method, known as gradient descent, which is widely used as an optimization technique in machine learning.

Gradient Descent

As the name suggests, the gradient descent optimization technique involves updating the values of the model parameters or coefficients in the direction of decreasing gradient, that is, the route of fastest change. The step size or rate at which the values of the coefficients are updated is called the learning rate, and is denoted as α. In our one-dimensional example, the update steps

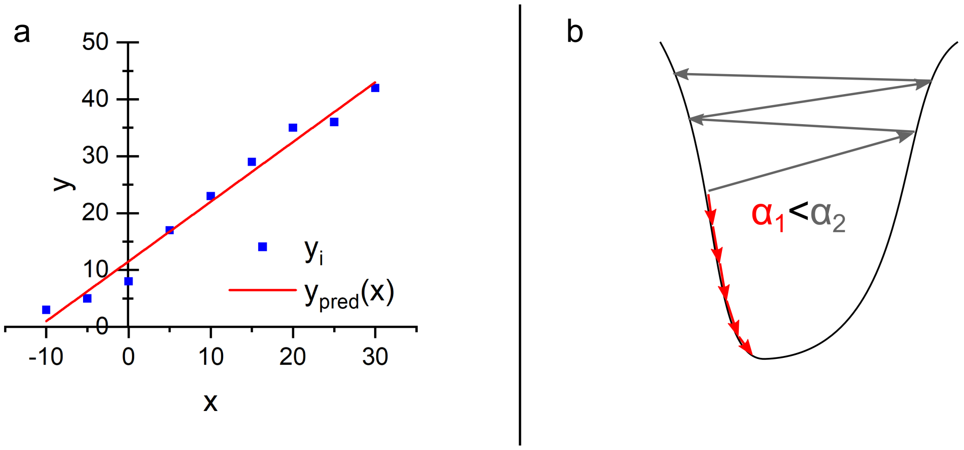

Figure 2.5: (a) Sample data points (blue squares) and the linear fit for the data obtained by least squares fitting. (b) The effect of the learning rate, α, in the gradient descent optimization technique. Here, α_1 (red) leads to a converging result with minimum error, while α_2 (grey) is too large in this case.

can be represented as follows:

$$a_{\text{new}} = a - \alpha \frac{\partial C}{\partial a} \tag{2.64}$$

$$b_{\text{new}} = b - \alpha \frac{\partial C}{\partial b} \tag{2.65}$$

In a scenario with more input parameters, the same is followed for all the corresponding coefficients.

Care must be taken when choosing the learning rate, α, for optimal performance. If too large, the algorithm might miss the real minima and run off to higher values. If chosen too small, finding the minimum may take a lot of time or computational effort due to the large number of iterations that would be required. This is shown in Fig. 2.5(b).

2.5.2 Logistic regression

In linear regression, the output parameter is free to take on any value from $-\infty$ to $+\infty$. While this proves useful, there are scenarios where the range of output values is limited, to say between zero and 1. Another set of problems may have it such that the output is limited to an integer number of possibilities, the extreme case of which being the binary classification problem where the output is limited to 2 possibilities. Logistic regression is a useful technique for the case of binary classification, working as follows.

Similar to before, let us consider a simple linear relation on a single input parameter, x, given by:

$$z = ax + b \tag{2.66}$$

Let the two possible outcomes in a binary classification problem be 0 and 1. To perform logistic regression, we first squeeze the range of the output to the interval $(0, 1)$ using a mathematical function called the Sigmoid function, which is represented as follows:

$$\sigma(z) = \frac{1}{1+e^{-z}} \tag{2.67}$$

We define $\sigma(ax + b)$ to be the output parameter, i.e,

$$y_{\text{pred}}(x) = \sigma(ax+b) + \frac{1}{1+e^{-(ax+b)}} \tag{2.68}$$

Having obtained the predicted output values, the cost (C) that quantifies the error in predicting the value of the output, y, is defined as follows:

$$C = \begin{cases} -log(y_{\text{pred}}) & \text{if } y = 1 \\ -log(1-y_{\text{pred}}) & \text{if } y = 0 \end{cases} \tag{2.69}$$

Fig. 2.6(a) depicts the Sigmoid function. The cost function described above is shown for the two cases of $y = 0$ and $y = 1$ in (b). Using gradient descent in a similar way as before, the model for effective binary classification is developed.

2.5.3 Linear support vector machine

A linear support vector machine is a powerful tool for separating linearly separable data belonging to two classes. A detailed description of support vector machines can be found in Ref. [16]. Fig 2.7 shows an example of linearly separable (left) and nonlinearly separable (right) classes, for the case where there are two independent input parameters or features, x_1 and x_2. This means that, in the first case, we can construct a line that separates the space into two sub-spaces, each corresponding to a class. In the second case, a line would not be sufficient to correctly separate the two classes. One would need a curve, which is a nonlinear expression in x_1 and x_2 to do the same.

Let us now consider the linearly separable case. The question arises, as to how to construct select the line that best separates the two classes. Let

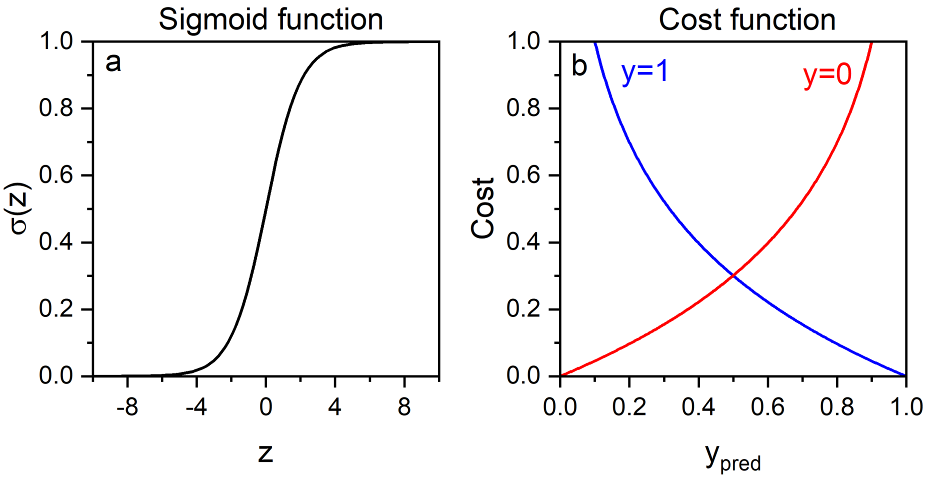

Figure 2.6: (a) The Sigmoid function which maps an input in the interval $(-\infty, \infty)$ to an output in the interval $(0, 1)$ (b) The cost function for logistic regression as a function of the predicted output for the two outcomes in a binary classification problem.

us take a step back, and consider the case where there is a single classifying parameter, instead of two, as shown in Fig. 2.8(a). The two classes represented in red and blue can be separated by setting a threshold value anywhere between $x = 2$ and $x = 4.25$. The threshold point can more generally be referred to as a decision boundary, to encompass cases with multiple parameters. One possible choice fro the decision boundary, so as to maximize the distance from the decision boundary to the data points closest to it. This can be done by calculating the mid-point of the two closest points, one each from the two distinct classes.

Fig. 2.8(b) shows a sample case with two parameters or variables, x_1 and x_2. In the 2-dimensional case, a linear decision boundary implies a line. Now the task lies to determine the slope and position of the line. We, again, try to maximize the margin, that is, the distance of the decision boundary to the data points closest to it on either side. The data points closest to the decision boundary are called support vectors. They are responsible for determining the maximum-margin decision boundary. The fact that the orientation of the decision boundary is determined by the support vectors, and not the entire set of data points reduces the number of computations required. This is a major reason behind the popularity of support vector machines.

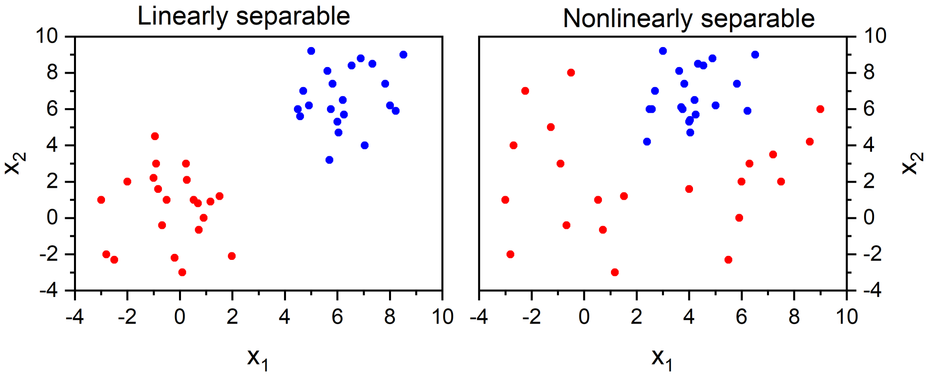

Figure 2.7: Linearly separable (left) and nonlinearly separable (right) distributions with respect to parameters x_1 and x_2

2.5.4 Quantifying classification accuracy

Once a classifier is created, the next step is to evaluate how well the classification works. Let us assume that the input parameters have been transformed into a single classifying parameter. We consider the simplest of a binary classification, where there are two output classes. Fig. 2.9 displays two distinct distributions of the occurrences over the classifying parameter, with the two classes, positive and negative, shown in green and blue respectively in each case.

In (a), there is a clear separation between the two classes with respect to the classification parameter. By setting an appropriate value of the parameter as the classification threshold, the two classes can be accurately separated, with the positive class having values of the classification parameter that are lower, and the negative, higher than the threshold. In (b), the separation is not as clear, as there is a range of values that could correspond to either class. Thus one can say that (a) represents a better classifier than (b). Next, we shall introduce some parameters that are used to quantify the effectiveness of a binary classifier.

The Confusion Matrix

This is a matrix that quantifies the effectiveness of a classification model by displaying the actual and predicted number of items in each class, thereby showing how many have been correctly and incorrectly classified. Table 2.3 represents the confusion matrix for a binary classification.

Fig. 2.10 represents a distribution involving two outcomes plotted as a

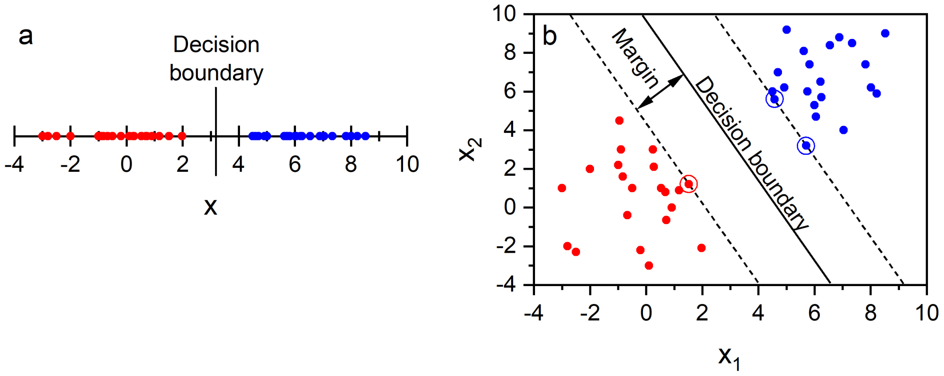

Figure 2.8: Choosing the decision boundary for binary classification using support vectors

Predicted value	Actual value	
	True	False
True	True Positive (TP)	False Positive (FP)
False	False Negative (FN)	True Negative (TN)

Table 2.3: Confusion matrix for binary classification.

function of a classifying parameter. The dotted black represents a classification threshold. Cases where the classifying parameter has a lower value than the threshold are predicted to be positive, and those with a higher value are predicted to be negative. With reference to the confusion matrix depicted in Table 2.3, the true positive, false positive, false negative, and true negative portions of the distribution have been marked in light shades of green, red, grey and blue, respectively.

Two quantities that are used to rate the classification are sensitivity and specificity. Sensitivity refers to the fraction of symptomatic individuals who have been classified as positive, and is given by:

$$\text{Sensitivity} = \frac{\text{TP}}{\text{TP} + \text{FN}}. \tag{2.70}$$

Specificity refers to the fraction of symptom-free individuals that were correctly classified as negative, and is given by:

$$\text{Specificity} = \frac{\text{TN}}{\text{TN} + \text{FP}}. \tag{2.71}$$

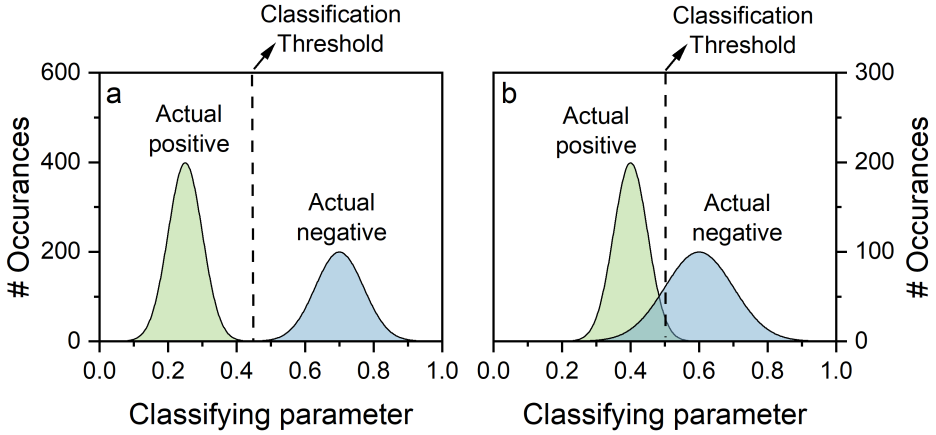

Figure 2.9: (a) The classifying parameter enables clear separation between positive and negative classes using a classification threshold. (b) The separation between the positive and negative classes is not clear or obvious.

Alternatively, the following two terms could be used:

$$\text{True Positive Rate (TPR)} = \frac{\text{TP}}{\text{TP} + \text{FN}} = \text{Sensitivity}. \tag{2.72}$$

$$\text{False Positive Rate (FPR)} = \frac{\text{FP}}{\text{FP} + \text{TN}} = 1 - \text{Specificity}. \tag{2.73}$$

In a binary classification scenario, the values of sensitivity and specificity depend on the selection of the classification threshold, as shown in Fig. 2.10. It is common practice to use as a performance metric, the sensitivity of a classifier at 95% specificity. In the following section, we shall look into a graphical representation, called the Receiver Operating Characteristic, to get a measure for the effectiveness of a classifier, independent of the value chosen for the classifier threshold.

In the intended application of this work, the positive class refers to symptomatic individuals for a particular type of cancer, and the negative class, to non-symptomatic individuals.

Receiver Operating Characteristic

To generate the graphical representation called the receiver operating characteristic (ROC), we scan the classifier threshold across the entire range of values of the classifying parameter. Fig. 2.10(b) to (e) displays four sample

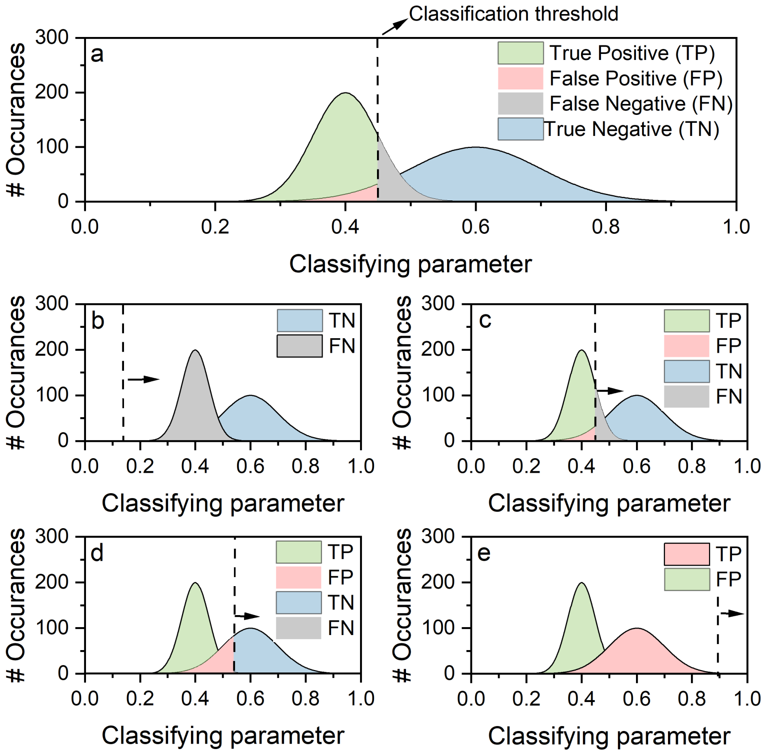

Figure 2.10: (a) Dependence of sensitivity and specificity on the selection of the classification threshold. (b-e) Shifting the classification threshold to construct the ROC curve

snapshots of the distribution of true positive, false negative, true negative and true positive predictions, on shifting the classification threshold from left to right. Fig. 2.10(b) shows how at one extreme, the TPR and FPR. In most real life cases of binary classification, there is a region of overlap where the actual positive and negative cases are not distinguished accurately, giving rise to false positive and false negative cases. This can be seen in 2.10(c) and (d), with false positive and false negative cases coming up to different extents. Sub-plot (e) shows the other extreme where all occurrences have been classified as positive. The True Positive Rate (TPR), as well as the False Positive Rate (FPR), is calculated at every point, and the TPR is plotted as a function of the FPR to generate the ROC curve for the distribution.

Fig. 2.11(a,c,e) displays three sample distributions as a function of the classifying parameter, and their corresponding ROC curves (b,d,f respectively). The area under an ROC curve, abbreviated as AUC, is a measure of the ability of a test to discriminate members of two classes. The AUC has

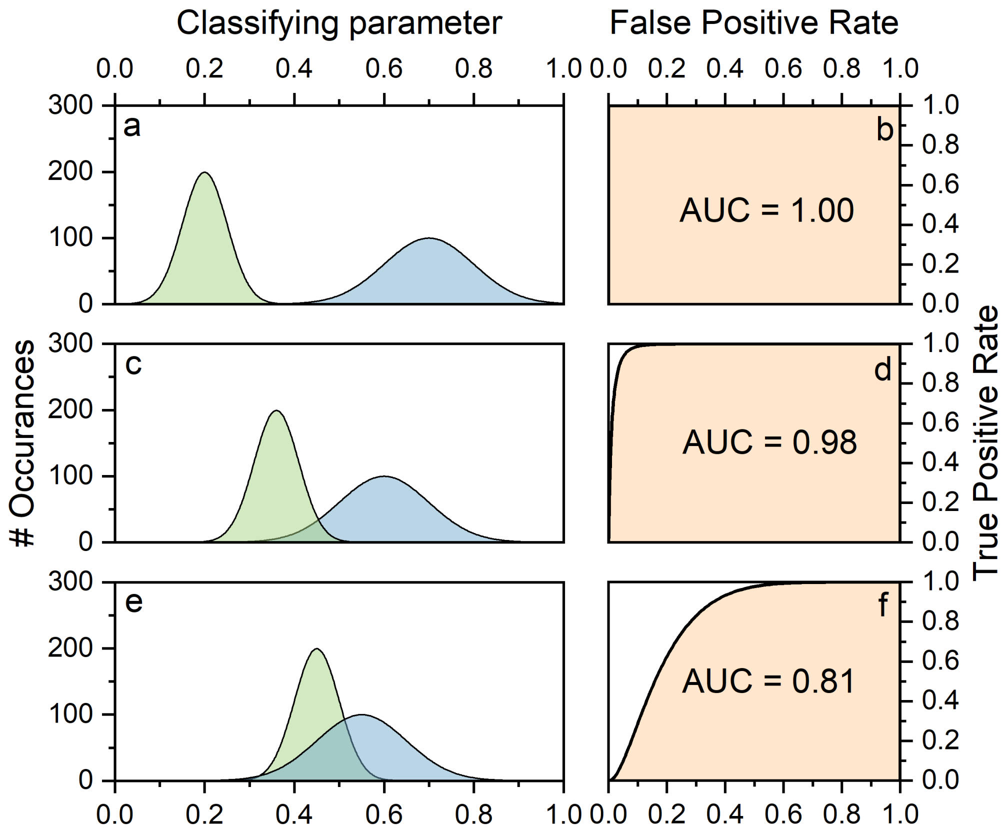

Figure 2.11: Example ROC curves for 3 different distributions

a minimum value of 0 and a maximum value of 1. An AUC of 1 describes correct classification by the classifier model. The AUC represents the probability that a pair of samples, one from either class, is classified correctly [34].

Fig. 2.11(a) represents an ideal scenario where the two classes are clearly separated in the distributions over the classifying parameter. The corresponding ROC curve, as shown in Fig. 2.11(b) is a rectangle with the area under it being 1. In the example in Fig. 2.11(c), the two distributions have an overlapping region with respect to the classifying parameter. As a result, the area under the ROC curve shown in Fig. 2.11 (d) is lower than 1. Fig. 2.11(e) displays a situation with greater overlap or ambiguity. The deviation of the area under the ROC curve (Fig. 2.11(f)) is stronger in this case, coming to 0.81. An AUC of 0.5 corresponds to the situation of pure chance, that is, there is a 50% probability of 2 samples belonging to different classes being identified correctly.

Chapter 3

Ultra-rapid electro-optic sampling using a sonotrode

3.1 Slow-scanning field-resolving spectrometer

Our group previously demonstrated field-resolved infrared spectroscopy of liquid samples, highlighting the technique's superior sensitivity compared to Fourier transform infrared spectroscopy [76, 13]. The impulsive excitation of molecules in the sample by a short mid-infrared pulse that lasts just a few optical cycles enables background-free detection of the coherent electric-field response of the excited molecules.

Fig. 3.1 shows the experimental scheme for a slow-scanning field-resolving spectrometer, as in Ref. [13]. The setup consists of a mode-locked Yb:YAG oscillator generating NIR pulses centered at a wavelength of 1030 nm, with an average power of 90 W, pulse duration of 250 fs, and a repetition rate of 28 MHz. The pulses are spectrally broadened and temporally compressed to a pulse duration of 16 fs in a Herriott-type multipass cell [28]based on self-phase modulation in bulk silica. A beam splitter splits off a small portion of the power of the 16-fs pulses to act as a gate pulse with variable delay for electro-optic sampling. A major portion of the 60 W of average power is focused onto a non-linear optical crystal for intra-pulse difference frequency generation, generating few-cycle mid-infrared pulses with an average power in the range of tens of mW.

The MIR pulses are collimated and focused onto the liquid sample in a cuvette. The MIR and gate beams are later combined for the infrared waveforms to be measured by EOS. Shown in green is a beam from a continuous wave (CW) laser used for delay calibration. The beam is split at the beam splitter so that its two branches trace the mid-infrared and gate pulses. The

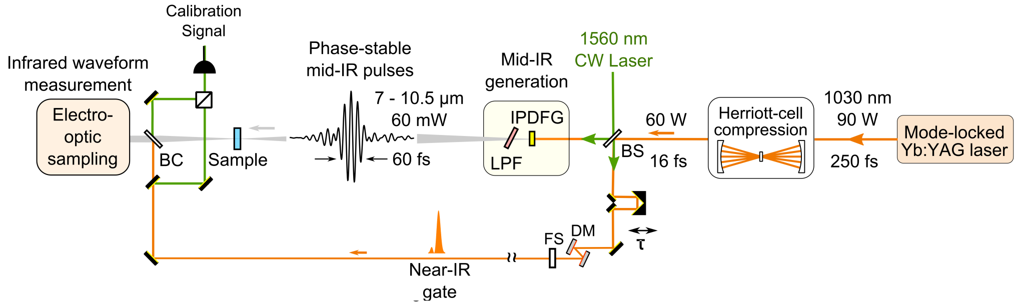

Figure 3.1: Schematic diagram for field resolved spectroscopy with slw mechanical delay scanning. CW: Continuous wave; BS: Beam splitter; DM: dispersive mirror; FS: Fused Silica; BC: Beam combiner.

two branches are later combined to obtain an interferometric signal that is measured and enables precise delay tracking [83]. To capture the infrared waveform, the gate pulse scans the mid-infrared waveform by varying the optical delay. This is done using a retroreflector mirror placed on a motorized linear translation stage that changes the length of the optical path traversed by the gate beam. A single scan of the optical delay covering 5-10 picoseconds takes 1-2 seconds.

3.2 Sonotrode scanning: Experimental setup

Building on the slow-scanning field-resolving spectrometer setup, we introduced an industrial sonication device called a sonotrode, with a mirror mounted on its vibrating surface to act as an ultra-rapid optical delay line. The idea of using a sonotrode to vary optical delays was previously demonstrated in Ref. [89] for time-resolved FTIR spectroscopy. Results from the sontrode-based ultra-rapid EOS experiment performed with Alexander Weigel have been published in Ref. [96]. The delay scanning setup comprises an ultrasonic generator (Hielscher UIP100hd) connected to a piezo-electric transducer, a mechanical booster, a sonotrode, and a mirror glued onto the sonotrode's front surface. The piezo-electric transducer, powered by the fast-oscillating voltage of the 500W generator, induced vibrations at kHz rates. The booster and sonotrode are designed to act together as an acoustic wave-guide, with either part being half the resonance wavelength corresponding to an oscillation frequency of 19 kHz, thus amplifying the piezo-induced oscillations to over 40 µm.

The experimental scheme for sonotrode-based ultra-rapid EOS is shown in Fig. 3.2. The setup is similar to the field-resolved spectroscopy scheme

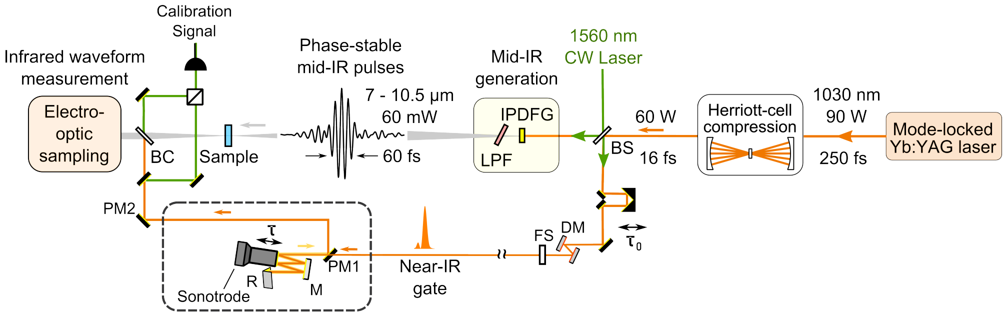

Figure 3.2: Experiental setup for ultra-rapid EOS using a sonotrode. BS: Beam splitter; LPF: Lowpass filter; DM: Dispersive mirror; FS: Fused silica; PM: Pickoff mirror; M: Mirror; R: Retroreflector; BC: Beam combiner.

with slow delay scanning described in Fig. 3.1 but with the addition of the sonotrode in the path of the NIR gate beam. Phase-stable few-cycle mid-IR pulses with a pulse duration of 60 fs, an average power of 60 mW, covering a spectral range from 7 - 10.5 µm in wavelength are generated in a 1-mm-thick crystal of $LiGaS_2$ by IPDFG.

The sonotrode now does the delay scanning by varying the path length of the EOS gate beam. The oscillation amplitude of the sonotrode was tuned to 70 percent of the maximum, coming to 30 µm. The amplitude was set at a level lower than the maximum to prevent the glued mirror from getting detached from the sonotrode surface. The gate beam was reflected 4 times on the mirror to increase the corresponding total delay range by a factor of 4, from 0.4 ps to 1.6 ps. A linear delay stage was used to match the path length of the gate pulses to that of the mid-IR pulses, that is to find time-zero (τ_0). This was done before acquiring EOS traces, and the stage was kept stationary during each measurement, as the sonotrode carried out the delay scan. The optical path from after the Herriott-cell compression stage, till after the GaSe EOS crystal lies in vacuum-compatible chambers, with the sonotrode introduced from one of the walls of the chamber by a KF-40 flange.

Fig. 3.3 shows views of the sonotrode from inside and outside the chamber. A retroreflector 'roof' mirror is used to change the height of the gate beam after two bounces on the sonotrode. The beam is reflected off the sonotrode two more times, before being picked off by mirror PM1, which is placed at a lower height than the incoming beam. The CW laser beam is separated from the mid-IR beam at the Germanium beam combiner, and from the gate beam by pick-up mirror PM2.

Marked in green in Fig. 3.2 is an auxiliary continuous-wave (CW) laser

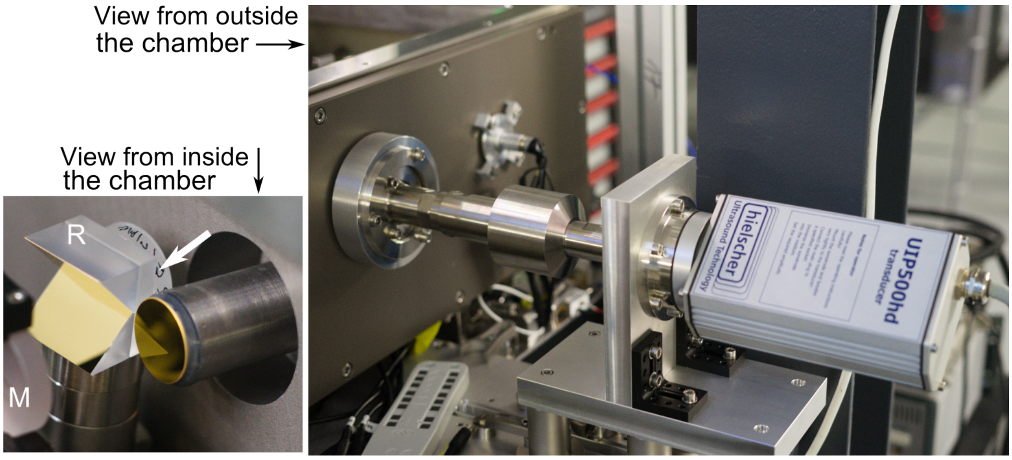

Figure 3.3: Photographic images showing views of the sonotrode from inside and outside the vacuum-compatible experimental chamber

that was used to precisely calibrate the relative delay of the gate pulses with respect to the mid-IR pulses interferometrically. This auxiliary beam was split into two, tracing both the mid-IR and gate pulse beam paths before they were recombined to obtain the interferometric calibration signal. The EOS signal was recorded using a balanced heterodyne detection setup, using 100MHz-bandwidth balanced photodetector (Femto HBPR-100M-60K-IN) with a built-in transimpedence amplifier. The signals were then channeled to a high-speed 2-channel 14-bit digitizer card (Gage RazorExpress 1422 CompuScope) and stored digitally.

The acquisition of the digitizer card was synchronized with the fourth harmonic of the repetition frequency of the laser oscillator to capture data at a rate of 112 Megasamples/second. Sampling was done at this high rate to ensure that the Nyquist sampling criterion was satisfied for the calibration signal. While the EOS signal was also sampled in synchrony with the calibration signal at 112 MHz, only one in every 4 of the acquired data points corresponded to a mid-IR laser shot. Data from the calibration channel and the relevant quarter of the data from the EOS channel were then analyzed to extract the delay axis for each scan in post-processing, the algorithm for which will be described in the following section.

3.3 Sonotrode scanning: Delay extraction

Electro-optic sampling with sonotrode-based ultra-rapid delay scanning enables the capture of 38,000 scans per second, capturing every single laser shot.

For precision spectroscopic applications, however, the relative delay between the gate and mid-IR pulses is to be determined with sub-femtosecond precision. To effectively average scans acquired over multiple seconds would mean that hundreds of thousands of acquired scans would have to align on top of each other perfectly. Accurate extraction of the delay information turns out to be an important task. This section describes the delay extraction algorithm developed for this purpose with Alexander Weigel and Michael Trubetskov. Knowledge of the approximate motion of the sonotrode was taken into account in developing a sequential predictor-corrector algorithm. The steps of the algorithm are described below.

3.3.1 Data preparation

The interferometric calibration signal was normalized to the range [-1,1], considering segments of 170 points each. The turning points of the interferometric signal, that is, the points where the direction of motion of the sonotrode switched, were identified by exploiting the symmetry of the signal around the turning points. Fig. 3.4 shows a section of the raw (top) and normalized (bottom) interferometric calibration signal. The inset zooms into a turning point. The data index of each turning point, n_{tp} was obtained by locating the points of minimal asymmetry in an interval where the turning point was expected, as follows:

$$n_{\mathrm{tp}} = \min_{n} \left[\sum_{i=1}^{m} \left(I_{\mathrm{raw}}(n+i) - I_{\mathrm{raw}}(n-i) \right)^2 \right]. \tag{3.1}$$

Here, n represents the data index, I_{raw}, the intensity of the raw calibration signal, and m, the size of the segment chosen for evaluating the symmetry. We use the value of the turning point indices to later cut the measured signals into forward and backward scans. The distance between the turning point gives an estimate to the period of the oscillatory motion of the sonotrode.

3.3.2 First estimation

Th optical delay, τ, follows the motion of the sonotrode, which is approximately sinusoidal, and can be estimated as follows:

$$\tau(n) = A_{\tau} \cos\left(\frac{2\pi}{T} (n - n_{\mathrm{tp0}}) \right) + \tau_0, \tag{3.2}$$

where n represents the data index, n_{tp0}, the data index corresponding to the first turning point, τ_0, the optical delay at the first turning point, T is the

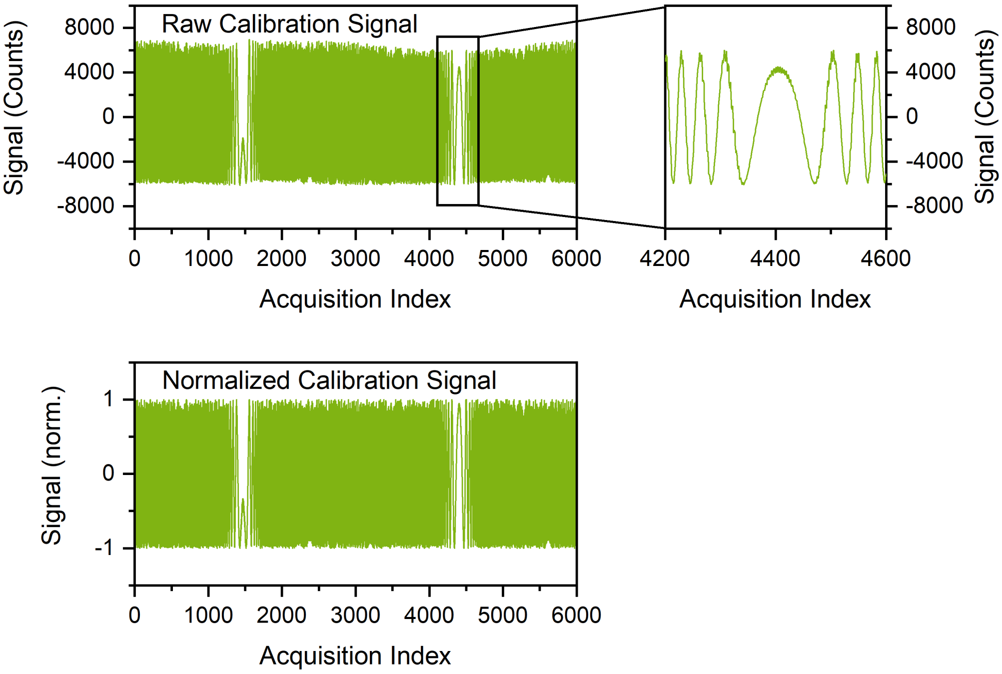

Figure 3.4: Segments of the raw (top) and normalized (bottom) interferometric calibration signal. The inset in the top panel zooms into an interval surrounding a turning point of the calibration signal.

period of oscillation of the sonotrode in terms of nuber of data points, and A_τ is the amplitude of oscillation in terms of optical delay. A_τ is proportional to the amplitude of oscillation of the sonotrode in space, A_s, as well as the number of times the beam is reflected off the sonotrode, N_{ref}, as follows:

$$A_\tau = \frac{A_\mathrm{s} \cdot N_\mathrm{ref}}{c}. \tag{3.3}$$

Here, c represents the speed of light in air.

We use the approximation given by Eq. 3.2 to predict the change in delay from data point n to $(n+1)$. We shall call the increment $\Delta\tau_{pred}(n)$, and obtain it by taking the derivative.

$$\Delta\tau_\mathrm{pred}(n) = \tau(n+1) - \tau(n)$$

$$\Delta\tau_\mathrm{pred}(n) = -A_\tau \frac{2\pi}{T} \sin\left(\frac{2\pi}{T}(n + 0.5 - n_\mathrm{tp0}) + \tau_0\right) \tag{3.4}$$

We take the derivative at the midpoint of n and $n+1$, hence $n+0.5$.Thus starting at the very first data, we take a step in predicting the optical delay of the next point. We then translate the predicted delay into a corresponding value for the normalized interferometric signal given by:

$$I(n) = \sin\left(\frac{2\pi c}{\lambda}(\tau) + \phi_0\right) \tag{3.5}$$

Here, c is the speed of light in air, lambda is the optical wavelength of the calibration laser, which is 1560 nm, and ϕ_0 is the optical phase associated with the geometric setup of the interferometer.

3.3.3 Initial conditions

For simplicity, let $n_{pt0} = 0$. Let us set τ_0 as $-A_{tau}$ such that $\tau(n = 0) = 0$. τ_0 is adjusted later, in post processing, such that zero delay matches with the peak of the excitation pulse.

We take the difference between the first and third turning points as an initial estimate for the period of oscillation of the sonotrode (T) in terms of data points, i.e,

$$T_{\text{est}} = n_{\text{tp2}} - n_{\text{tp0}}.$$

The offset in the interferometric phase, ϕ_0, is given by,

$$\phi_0 = \sin^{-1}\left(I(n = 0)\right).$$

We can estimate the total delay range, A_τ by evaluating the number of oscillations of the interferometric signal between subsequent turning points. WIth the signal crossing zero twice every oscillation, we have,

$$A_\tau = \frac{1}{4}\frac{N_{\text{zc}} \cdot \lambda}{c}, \tag{3.6}$$

where N_{zc} is the number of zero crossings in the interferometric signal encountered between a pair of turning points, and c is the speed of light in air.

3.3.4 Sequential prediction and correction

The next step involves point-by-point sequential prediction and correction. From a data point n, we predict the value of the interferometric signal at the next data point, $n + 1$, compare it to the actual signal, and correct for the deviation in the optical delay.

1. **Prediction:** Taking note of delay and interferometric signal values at acquisition index n, i.e, $\tau(n)$ and $I(n)$, the predicted change in delay

in moving to the next acquisition index, $\Delta\tau_{pred}$ is evaluated using Eq. 3.4. The predicted value of the interferometric signal, I_{pred}, is then obtained using Eq. 3.5:

$$I_{\mathrm{pred}}(n+1) = \sin\left(\frac{2\pi c}{\lambda}[\tau(n) + \Delta\tau_{\mathrm{pred}}(n)] + \phi_0\right) \tag{3.7}$$

2. **Correction:** The predicted interferometric signal at acquisition index $n+1$, $I_{\mathrm{pred}}(n+1)$ is compared with the actual interferometric signal $I(n+1)$. The difference between the two,

$$\delta I(n+1) = I(n+1) - I_{pred}(n+1)$$

.

Fig. 3.5 shows the motion of the sonotrode over a short segment in time (top panel), and the corresponding normalized calibration signal (bottom). The zoomed-in inset on the right shows the actual and predicted data points at a particular acquisition index, along with the difference δI.

This difference is translated to a corresponding change in the optical delay, $\delta\tau$ which is used to correct for $\Delta\tau_{pred}$:

$$\delta\tau = \delta I \frac{\Delta\tau_{\mathrm{pred}}}{I_{\mathrm{pred}}(n+1) - I(n)}, \tag{3.8}$$

so that $\tau(n+1)$ is given by:

$$\tau(n+1) = \tau(n) + \Delta\tau_{\mathrm{pred}} + \delta\tau, \tag{3.9}$$

3. **Update parameters:** After each oscillation of the sonotrode, that is after advancing by a pair of turning points, the period, T, amplitude (in terms of optical delay), A_τ of the next oscillation (m+1) of the sontrode are updated as follows.

$$T(m+1) = n_{\mathrm{tp(2m+2)}} - n_{\mathrm{tp(2m)}}$$

$$\text{for } m \in \mathbb{N},$$

$$A_\tau(m+1) = \max_n(\tau(n)) - \min_n(\tau(n)),$$

$$\text{for } n \in \{n_{\mathrm{tp(2m)}}, n_{\mathrm{tp(2m)}} + 1, n_{\mathrm{tp(2m)}} + 2, ..., n_{\mathrm{tp(2m+2)}} - 1, n_{\mathrm{tp(2m+2)}}\}$$

4. **Repeat** steps 1-3 till the end of a measurement

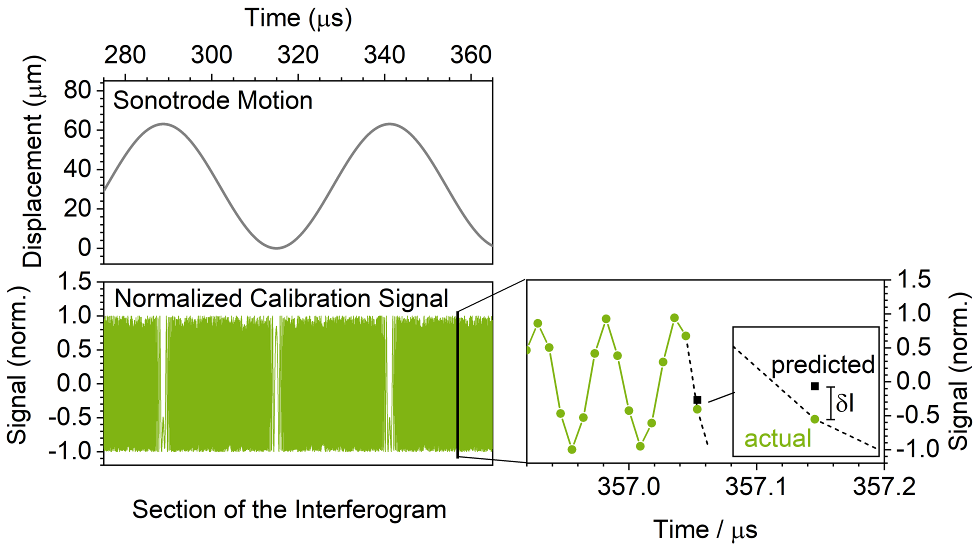

Figure 3.5: A segment showing the motion of the sonotrode with time (top) and the corresponding interferometric calibration signal (bottom). The inset zooms into a few data points, showing the measured (green) and predicted (black) values of the interferometric signal at a time point. The difference between the two, δI is used to make corrections to the predicted delay axis, for accurate calibration.

3.3.5 Post-processing

After the delay axis is extracted for a continuously recorded dataset, a series of post-processing steps are performed to improve the accuracy of the delay axis, using known information regarding the motion of the sonotrode, as well as to prepare the data, separating a single stream of data into individual scans for further analysis.

1. **Low-pass filtering the delay axis:** A second-order Butterworth low pass filter with a cut-off frequency of 2.24 MHz was applied on the extracted delay axis, $\tau(n)$. Fluctuations at higher frequencies, far beyond the scan frequency of the sonotrode, do not originate from the motion of the sonotrode, and were attributed to the detection noise. Hence, these frequency components were removed from the delay axis.

2. **Downsampling the signal and the delay axis:** Data acquisition was carried out at 112 MHz from the balanced photodetector capturing the EOS signal, as well as from the photodiode capturing the delay calibration signal. The mid-IR pulses are generated at a lower rate of

28 MHz. To separate out meaningful data, we downsample the data recorded by EOS by factor of 4. The delay extraction used all data captured from the calibration signal, at a rate of 112 MHz. Once the delay extraction is done, downsampling the extracted, low-pass-filtered delay axis, gives us the delay axis corresponding to down sampled EOS signal, while keeping the information provided by the excluded data points of the delay axis.

3. **Baseline correction:** Variations in beam pointing associated with the motion of the sonotrode cause fluctuations in the baseline of the raw EOS signal. A 140-kHz high-pass filter(in laboratory time) was applied to mitigate the variations in the baseline, as shown in Fig. 3.6(a).

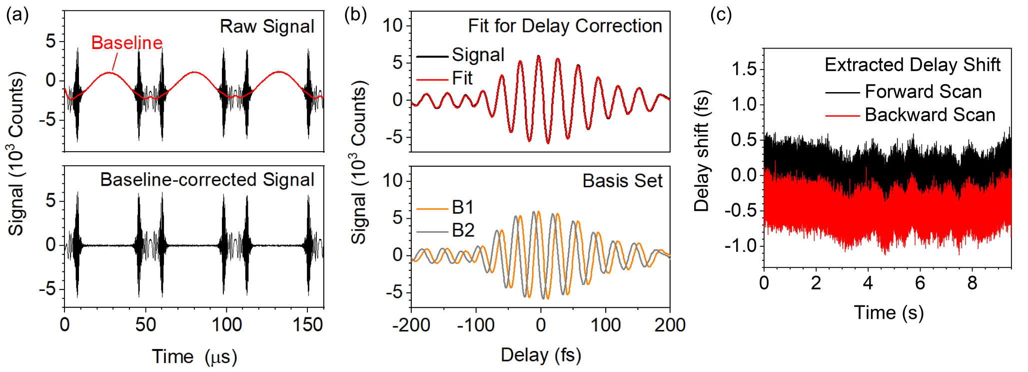

Figure 3.6: Sonotrode delay extraction: post-processing steps. (a) Baseline correction using a 140-kHz hugh-pass filter. (b) Delay correction for individual scans obtained by finding a linear combination of basis functions B_1 and B_2 from the first EOS scan (bottom panel) that best fits the i^{th} scan (EOS signal of i^{th} scan shown in black in the top panel, fit shown in red. (c) Extracted delay shift for each individual forward (black) and backward (red) scan over a 9.5-s-long measurement comprising of 365,800 scans

4. **Separation into individual scans:** The continuosly acquired EOS signal, as well as the extracted delay axis was split into individual forward and backward scans, using the turning points described earlier. Each individual scan corresponds to an acquisition time of 263 µs.

5. **Delay shift correction:** The calibration beams and the mid-IR and gate beams for EOS share common beam paths, except when the signals are spatially separated at the end, for independent detection. In order to compensate for drifts between the calibration and EOS signals that

may occur over the course of a measurement, a delay shift correction was performed for each individual EOS scan. Let the delay drift in the forward and backward scans be represented by $\delta\tau_{i,FW}$ and $\delta\tau_{i,BW}$, where i represents the trace index. $S_{i,FW}$ and $S_{i,BW}$ be the EOS signal corresponding to the i^{th} forward and backward delay scan, respectively. We use the first forward EOS scan, $S_{0,FW}$ to define a pair of basis functions $B_{1,\mathrm{FW}}(\tau)$ and $B_{2,\mathrm{FW}}(\tau)$, such that:

$$B_{1,\mathrm{FW}}(\tau) = S_{0,\mathrm{FW}}(\tau),$$

$$B_{2,\mathrm{FW}}(\tau) = S_{0,\mathrm{FW}}\left(\tau + \frac{1}{4\nu_c}\right).$$

Here, ν_c represents the carrier frequency of the mid-IR waveform (33.3 THz in our case). This implies that B2 and B1 have a relative phase difference of $\pi/2$.

Fig. 3.6(b) depicts the shift correction procedure. The top panel shows the i^{th} scan on which the shift correction needs to be applied (black). The bottom panel shows the basis functions B_1 and B_2 obtained from the first EOS scan. Any signal, $S_{0,\mathrm{FW}}(\tau + \delta\tau)$, obtained by shifting $S_{0,\mathrm{FW}}(\tau)$ by a constant phase, can exactly be expressed as a linear combination of $B_{1,\mathrm{FW}}(\tau)$ and $B_{2,\mathrm{FW}}(\tau)$ as follows:

$$S_{0,\mathrm{FW}}(\tau + \delta\tau) = p_{0,\mathrm{FW}} B_{1,\mathrm{FW}} + q_{0,\mathrm{FW}} B_{2,\mathrm{FW}}. \tag{3.10}$$

By finding the linear combination of the two basis functions that best fits the i^{th} scan, as shown by the red line on the top panel of Fig. 3.6(b), the delay shift, $\delta\tau$, is extracted using the following relation:

$$\delta\tau = \mathrm{atan2}(p_{0,\mathrm{FW}}, q_{0,\mathrm{FW}}). \tag{3.11}$$

The atan2(x,y) function returns the two-argument arc tangent, which is the angle made by the line connecting the origin to point (x,y), with the x-axis. Fig 3.6(c) shows the delay shifts for each individual forward and backward scan, for a 9.5 s long measurement, which lies in the sub-fs range.

6. **Interpolation to a common delay axis:** Each individual trace, after the delay shift correction, was interpolated with a common, uniformly spaced delay-axis.The uniform spacing would make it easier to perform Fourier transformation.

With the measured data having been post-processed and arranged as EOS traces corresponding to individual delay scans, it is ready to be analyzed, involving evaluations of the sensitivity, reproducibility and stability of the measured infrared waveform. This will be the focus of the following section.

3.4 Sonotrode scanning: Results

3.4.1 Sensitivity and dynamic range

Fig. 3.7(a) shows an individual-scan (black) and an averaged-scan (orange) EOS trace acquired over 26 µs and 9.5 s respectively, overlaid on top of each other. The orange trace, which is an average of 365,800 scans including scans in both forward and backward directions, resembles the individual-scan trace in shape as well as amplitude, such that the two are hardly distinguishable in the plot. This bears witness to the accuracy of the delay extraction process, as well as the intrinsic stability of the MIR waveforms generated by IPDFG [95, 77, 45, 76]. A deviation in either the delay axis, or in the stability of the shape of the mid-IR waveforms would have caused a reduction in the amplitude of the EOS trace on averaging several scans.

Each data point in the individual-scan trace represents a single laser shot. A 1000 times zoomed-in version of a section of the averaged-scan signal is shown as an inset, demonstrating the enhanced ability of averaged scans to capture weaker signals. The lower panel shows the detection baseline, measured with the mid-IR beam blocked. Here again, an inset zooming into the averaged scan shows how the detection noise level decreases by close to three orders of magnitude on averaging 365,800 scans. Defining the time-domain electric-field dynamic range as the ratio of the maximum amplitude of the EOS trace to the root-mean-squared (RMS) detection-noise level obtained by blocking the mid-IR beam, we obtained a value of 150 and of 8×10^4 for individual-scan and averaged-scan traces respectively, with the increase roughly approaching the square-root of the number of scans averaged.

Performing a Fourier transform on the EOS traces in Fig. 3.7(a) gives us the corresponding spectra, which are shown in Fig. 3.7(b). The spectrum of the mid-IR radiation is centered at 1100 cm^{-1} in wavenumber, which corresponds to a wavelength of 9 µm, and spans from 940 cm^{-1} to 1420 cm^{-1} (8.9 µm - 10.6 µm) at -20dB. The top panel shows the spectra for the signal (blue shaded region) and detection noise (grey shaded region) for an individual scan, while the bottom panel shows the same for an average of 365,800 scans. We define the intensity dynamic range in the frequency domain as the ratio of the peak intensity of the EOS signal spectrum to the RMS value of

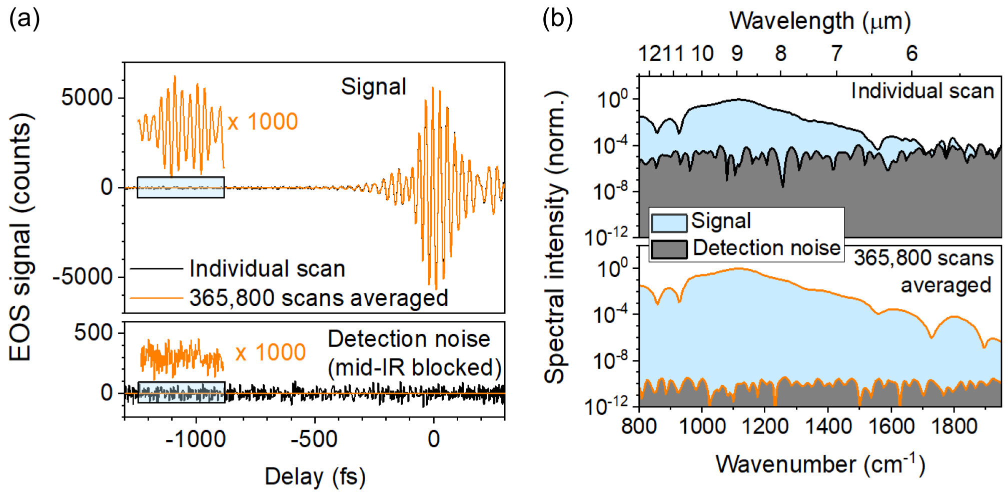

Figure 3.7: (a)Individual-scan (black) and averaged-scan (pink) EOS traces obtained by sonotrode ultra-rapid scanning, as a function of delay in the time domain. The detection noise obtained by blocking the mid-IR beam is shown in the bottom panel. (b) Spectra obtained by performing a Fourier transform on an individual scan (top) and an average of 365,800 scans (bottom) are plotted as function of wavenumber in the frequency domain. The shaded grey plots represent the detection noise in the frequency domain.

the detection noise. This corresponds to a value 1.6×10^5 for an individual scan, which increases by more than 5 orders of magnitude to 4.0×10^{10} on averaging 365,800 scans, which are acquired in 9.5 seconds.

In the next subsection, we will look into the timing precision of the delay extraction process in more detail.

3.4.2 Waveform reproducibility

Timing precision

We chose the delay positions where the mid-IR waveform crosses zero, in the region with the strongest EOS signal, as the points of reference to determine the timing precision of our EOS measurements. The top panel of Fig. 3.8(a) shows a section of an exemplary EOS trace (black line), centered around the negative peak of the trace, and spanning 80 femtoseconds in the positive as well as the negative direction. The zero crossing points are marked by solid black circles.

In the bottom panel, the standard deviation, σ_{ZC} in the position of the

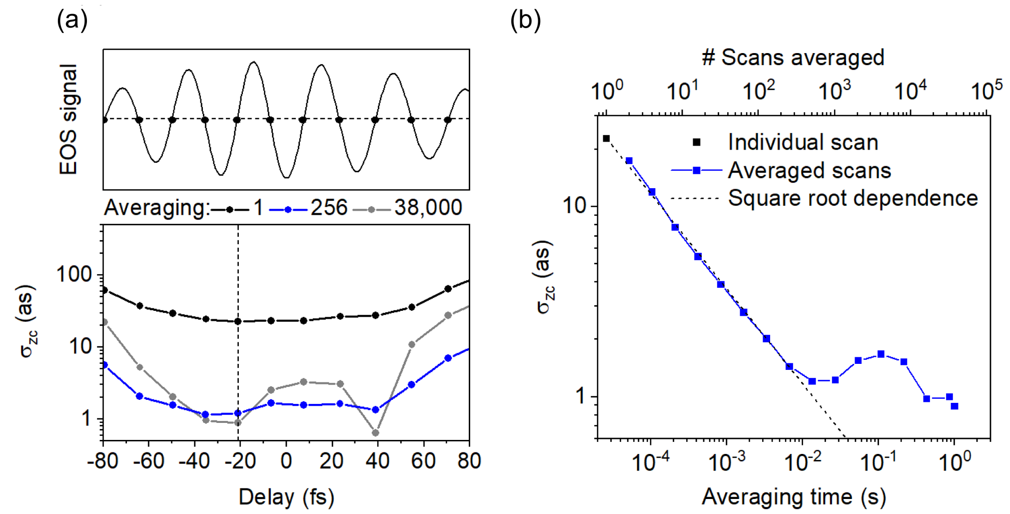

Figure 3.8: (a) The top panel shows a section of an individual EOS scan in the delay range where the amplitude is maximum. Zero-crossing points are marked by black circles. The bottom panel displays the standard deviation in the position of zero crossings σ_{ZC}, for a batch of individual scans (black), as well as for batches of averaged scans, with 256 scans averaged (blue), and 38,000 scans averaged (grey). (b) The value of σ_{ZC} for the zero-crossing at -21 as of delay (black vertical line in (a)) is plotted for a batch of 9 individual scans (black), as well as for batches of averaged scans (blue), as a function of the averaging time.

zero-crossings over 10 individual delay scans is plotted as a black line. The same is performed for a set of 256-scan averages (blue), as well as for 38,000-scan averages (grey). For individual scans, the mean value of σ_{ZC} for the 11 displayed zero crossings is 34 attoseconds. On averaging traces in sets of 256, the value goes down to 2.2 attoseconds. On further averaging, however, the value of σ_{ZC} increases to 7.2 attoseconds corresponding to batches of 38,000 traces, each acquired over 1 s. In Fig. 3.8(b), σ_{ZC} for the zero crossing at -21 as, represented by the vertical dashed line in Fig. 3.8(a), is plotted for a batch of 9 individual scans (solid black square), and for batches of averaged scans (solid blue square), for different averaging times/ numbers of traces averaged. It was observed that the precision increases with the square root of the averaging time, up until 10 ms, after which there was a deviation from the trend. We attribute this to infrared waveform distortions by laser fluctuations at sub-kHz timescales, mechanical vibrations and drifts. One possible reason for the mechanical effects is the fact that the EOS and delay calibration signals do not follow exactly identical paths. While we corrected for shifts in the entire delay axis for each individual delay scan in post-processing, as described in section 3.3.5, establishing a common path for both the EOS and delay calibration signals could help further.

Time-domain differences

The reproducibility of acquired EOS signal waveforms can be tested by looking at the difference between consecutive traces. The difference signal is expected to come to the level of the detection noise multiplied by $\sqrt{2}$. Fig. 3.9(a) displays the time-domain difference signals for three different scenarios as described in Fig. 3.9(b). The top panel shows the difference between two consecutive scan pairs, each being the mean of the EOS signals of a forward and the subsequent backward delay scan. Taking the mean of the two scans decreases the difference signal by a factor of $\sqrt{2}$ to bring it to the level of the detection noise of an individual scan. The RMS values of the two quantities are indeed similar, with the RMS value of the difference signal amounting to 8.5×10^{-3}, and that of the detection noise of an individual scan being 6.7×10^{-3}.

The middle panels of Fig. 3.9(a) and (b) simulate the difference between two EOS traces acquired by a conventional slow delay scanning technique, where a single scan is acquired over a few seconds. We call this slow referencing. In this case, 91,400 forward-backward scan pairs have been averaged (acquired in 4.75 s) and subtracted from the mean of the next set of 91,400 pairs (black plot in the middle panel of Fig. 3.9(a)).

There is a significant difference signal coming up to 10^{-2} in the region around 0 delay, where the EOS signal is strongest, which can be attributed to slow laser fluctuations and mechanical defects, as seen in Fig. 3.8 in the previous section. In order to check whether the large residual is due to fluctuations in the overall signal level, we scaled the second averaged trace before subtraction (orange). The large residue remained, indicating slow changes or fluctuations in the shape of the waveform in a time frame of seconds.

In the bottom panel in 3.9(a) and (b), another approach is adopted, where one forward-backward scan pair is subtracted from the subsequent pair, and the differences are added. This approach is only possible with rapid-delay scanning methods, such as the sonotrode. On doing this, what we call fast referencing, the difference signal goes down to the expected level in the order of 10^{-5}, on averaging over 9.5 seconds of acquired data.

Fast and slow referencing for various averaging times are compared in 3.9(c), where the RMS value of the difference signal across all delays is plotted as a function of the total measurement time, from 104 µs to 9.5 s. In the

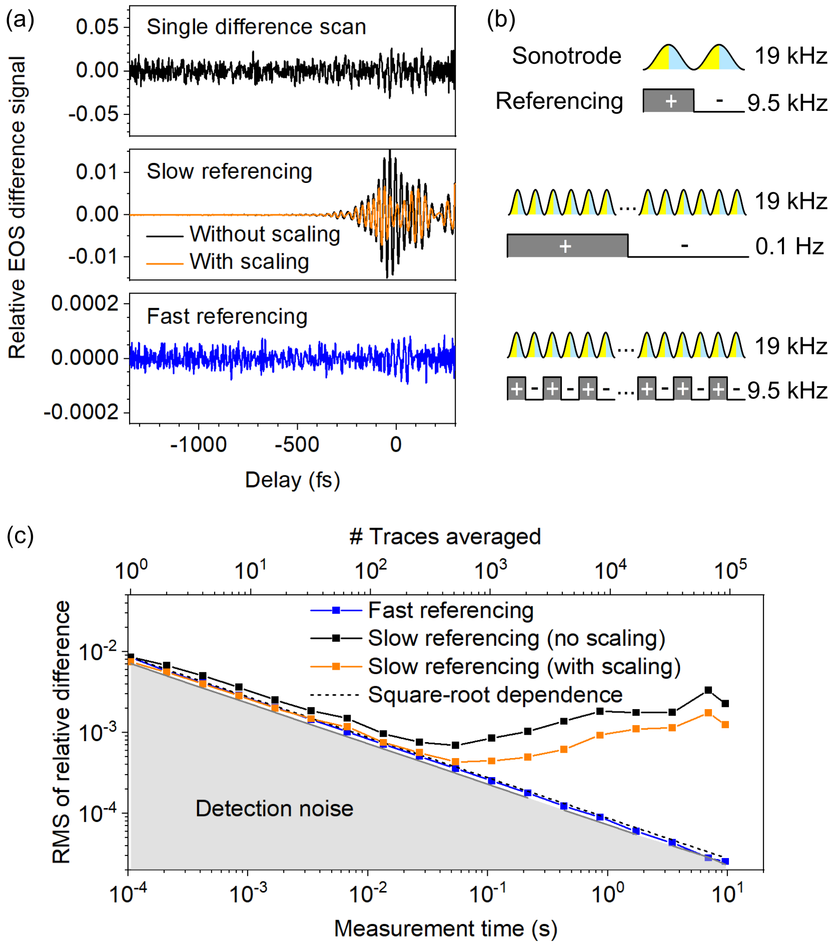

Figure 3.9: Time-domain referencing. The top panels in (a) and (b) show the difference between two subsequent signal scans. The middle panels (slow referencing) show the difference signals between two averaged scans, acquired over 4.75 s each, with and without scaling the averaged scans before subtraction (orange and black, respectively). The bottom panels represent pairwise difference signals of subsequent individual scans summed up over the entire measurement time of 9.5 s. (c) The difference signals for slow and fast referencing shown in the middle and bottom panels of (a) and (b) are plotted as a function of the measurement time, from 104 µs to 9.5 s.

case of slow referencing, we see a deviation from the statistical square-root dependence around the 10 ms mark. Scaling the averaged traces before subtration results in a minor improvement, but the trend remains the same.

Fast referencing on the other hand, results in the RMS relative difference going down with the square root of the number of traces averaged for the whole length of the measurement, which is 9.5 s.

3.4.3 Referencing in the frequency domain

In this section, we explore the reproducibility of spectra obtained by performing a Fourier transform on the EOS traces by taking ratios of consecutive spectra in the Fourier domain. In comparison to differences in the time domain, spectral ratios provide an instrument-independent quantity, which is broadly used in conventional Fourier transform spectroscopy. EOS goes beyond intensity-based spectroscopic techniques by providing information of the spectral phase, in addition. We thus obtain the complex sample response.

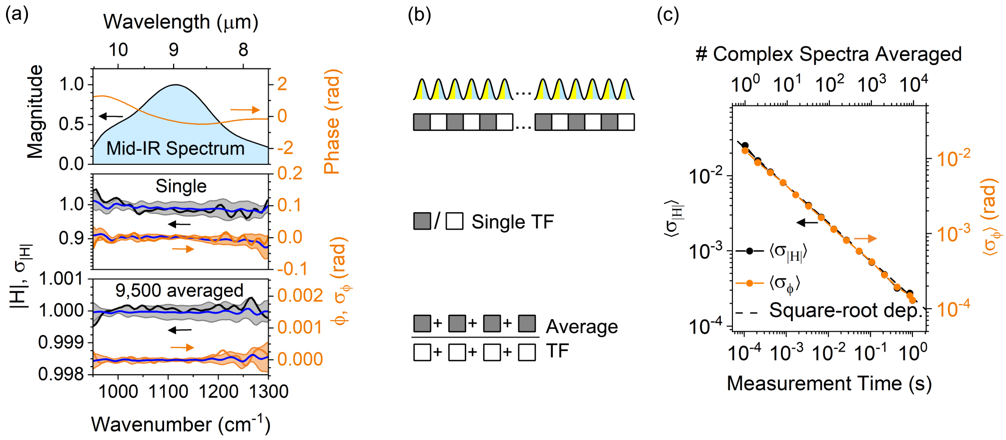

Figure 3.10: Referencing in the frequency-domain. (a) Top panel: Spectral magnitude (black) and phase (orange) of obtained by performing a Fourier transform of the time-domain EOS signal. Middle panel: Magnitude (black) and phase (orange) of a single transfer function (TF), obtained by taking a ratio between two consecutive complex spectra (shown in (b)). The blue lines show the mean value, the shaded regions, and the standard deviation, calculated over 9 Single TFs. Bottom panel: Averaged TFs were obtained from 19,000 spectra by taking the ratio between all odd-numbered spectra and all even-numbered spectra, as shown on the bottom panel of (b). Again, the blue lines and the shaded regions show the mean and standard deviation calculated over 9 Average TFs. (c) Mean calculated over the wavelength range from 900 cm^{-1} to 1300 cm^{-1} for the standard deviation of the magnitude (black) and phase (orange) average TFs, as a function of the number of scans averaged.

Fig. 3.10(a), on the top panel, shows the spectral magnitude and phase obtained by performing a Fourier transform on a time-domain EOS trace. The middle panel shows the magnitude (black line) and phase (orange line) of the ratio of two subsequent forward-backward scan pairs. We refer to this as a single transfer function transfer function (TF). The blue lines and the shaded regions display the mean and standard deviation obtained from 9 such single TFs.

In the absence of any sample, the ratio of spectra in the frequency domain equals unity, corresponding to a magnitude of 1 and phase of 0 in polar coordinates. The black and orange lines in the bottom panel of 3.10(a) show what we refer to as an average TF. Here, the sum of the spectra of odd-numbered scans (forward-backward scan pairs) is divided by the sum of the spectra of even-numbered scans, measured over 1 second. Again, the blue lines and shaded regions mark the mean and standard deviation calculated for 9 average TFs, measured over 1 second each.

Placing scans in the numerator and denominator of the formula for calculating the average TF is possible only with rapid scanning. In the measurement shown, there is no sample in that all measurements correspond to the same substance, pure water. The idea is to simulate a rapid referencing procedure, that is, to obtain measurements of a sample of interest and a reference liquid in an ultra-rapid manner, such that every odd scan corresponds to the sample and every even scan to a reference. This idea will be brought up again in the next chapter, in section 4.5.1, where its experimental implementation is described.

Fig. 3.10(c) shows the standard deviation in the magnitude ($\langle\sigma_{|H|}\rangle$, black) and phase ($\langle\sigma_{\phi}\rangle$, orange) of average TFs, averaged across the spectral range displayed in 3.10(a), from 900 cm^{-1} to 1100 cm^{-1} as a function of the total measurement time. In each case, the measurement was split into 9 segments, and the average TFs and the standard deviation were calculated.

Both $\langle\sigma_{|H|}\rangle$ and $\langle\sigma_{\phi}\rangle$ are observed to decrease monotonically with the square root of the number of spectra averaged for the entire available measurement time of 9.5 s. This proof of concept experiment suggests the possibility of an ultra-rapid referencing technique combined with the sonotrode-based ultra-rapid delay scanning for EOS being able to perform spectroscopic measurements with a sensitivity that scales with the square root of the measurement time, thus suppressing the effects of laser fluctuations and mechanical noise at the sub-kHz level.

We have looked at one method of rapid delay-scanning for EOS by using a sonotrode to act as an optical delay line in the gate beam path before it is combined with the MIR field to be sampled. The mirror attached to the front surface of the sonotrode, vibrating back and forth at a rate of 19 kHz, replaced a conventional optical delay line. The delay range and the scanning frequency were determined by the amplitude and frequency of vibration of the sonotrode, respectively. On the one hand, this restricted the possibilities for tailoring the delay scan to our needs. On the other hand, the rapid back and forth motion of the sonotrode potentially introduces variations in beam pointing. The gate laser beam for EOS was obtained by splitting off a part of the few-cycle NIR beam before generating MIR radiation. The delay was scanned by changing the optical path length of the gate beam with respect to the MIR beam.

In the next chapter, a dual-oscillator implementation of rapid electro-optic sampling is presented, where the delay scanning is done by means of electronically controlled detuning of the repetition rates of two laser oscillators. The gate pulse is sourced from a second laser system with a different central wavelength. By precisely calibrating the relative delay between the two lasers, we demonstrate rapid delay scanning with flexible delay ranges, scanning rates, and attosecond-level timing precision.

Chapter 4

Dual-oscillator electro-optic sampling

The idea of using two pulsed laser sources with detuned repetition rates to scan optical delay is not new. Paul A. Elzinga and co-workers introduced the concept of asynchronous optical sampling (ASOPS) for pump-probe spectroscopy more than three decades ago [20, 21]. In pump-probe experiments using the ASOPS technique, the pump and the probe pulses originate in two different mode-locked oscillators with a constant offset in their repetition frequencies instead of in the same laser. This results in a relative phase walk-off at a fixed speed, as shown by the expressions below, which have been adapted from Ref. [49]. Let f_1 and f_2 represent the repetition frequencies of the two lasers. The scan frequency Δf, time taken to acquire a single scan, t_{scan}, number of data points per scan, n_{scan} and the temporal resolution, Δt, are given as follows:

$$\Delta f = |f_1 - f_2| \tag{4.1}$$

$$t_{\text{scan}} = \frac{1}{\Delta f} \tag{4.2}$$

$$n_{\text{scan}} = \frac{f_1}{\Delta f} \tag{4.3}$$

$$\Delta t = \left| \frac{1}{f_1} - \frac{1}{f_2} \right| = \frac{|f_1 - f_2|}{f_1 f_2} = \frac{\Delta f}{f_1 f_2} \tag{4.4}$$

Fig. 4.1 shows a simplified setup scheme for dual-oscillator electro-optic sampling. Here, one out of two mode-locked femtosecond laser sources generates a phase-stable MIR pulse that is transmitted through the sample. The

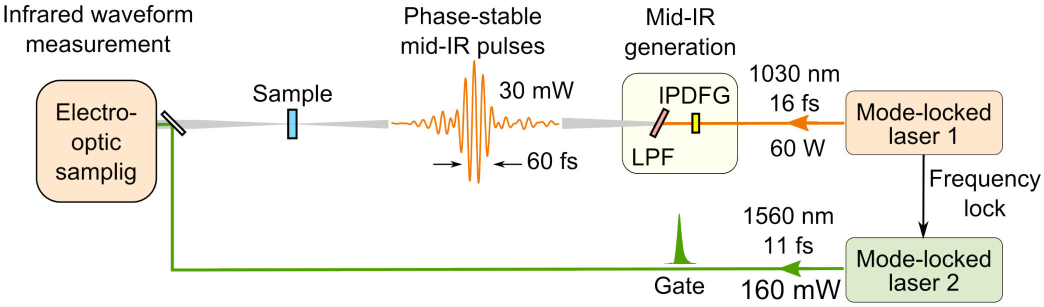

Figure 4.1: Simplified scheme for dual-oscillator EOS. The gate pulse is generated by a second mode-locked laser, whose repetition frequency locked to the first laser, but with a constant offset. LPF: low-pass filter.

MIR pulse excites molecular vibrations in the sample. A second mode-locked femtosecond laser generates pulses shorter than a half-cycle of the generated mid-infrared radiation to act as a probe, also called the gate, for EOS.

When the repetition rate of the second laser differs from that of the first laser by a constant offset, each subsequent gate pulse interacts with a different part of the mid-infrared pulse. If we start with the gate pulse overlapping with one end of the mid-infrared pulse and offset the repetition frequency in the right direction, the gate pulse will gradually move through to the other end of the mid-infrared pulse, after which the delay scanning continues, reaching the subsequent mid-infrared pulse in due time. The delay range of the scan is fixed as the reciprocal of the laser repetition rate, i.e., $\tau_{scan} = \frac{1}{f_1}$.

Fig. 4.2 (a) shows the EOS signal measured by asynchronous optical sampling over an acquisition time of 1 second. In our case, the laser repetition rate, f_1, is 28 MHz, thus resulting in a scan range,τ_{scan} of 35.7 ns. Each data point corresponds to a single laser shot. In liquid samples, the homogenous linewidth lies in the order of a THz, leading to picosecond level decay times. Considering the delay range of interest to be 10 picoseconds, the duty cycle with ASOPS with a 28 MHz laser system is less than one in a thousand. Fig. 4.2 (b) zooms into such a 15 picosecond delay range. Fig. 4.2 (c) shows a spectrum obtained by performing a Forier transform on a single delay scan.

To maximize the scan rate and minimize the dead time for the measurement, we limit the total delay range, restricting it to our range of interest. With the ASOPS technique, one would have to increase the repetition rates of the lasers to GHz levels. Such a change in the repetition rate is not easy to implement in all scenarios due to the resulting reduction in pulse energy. There is another solution to limit the total delay range to a few picoseconds:

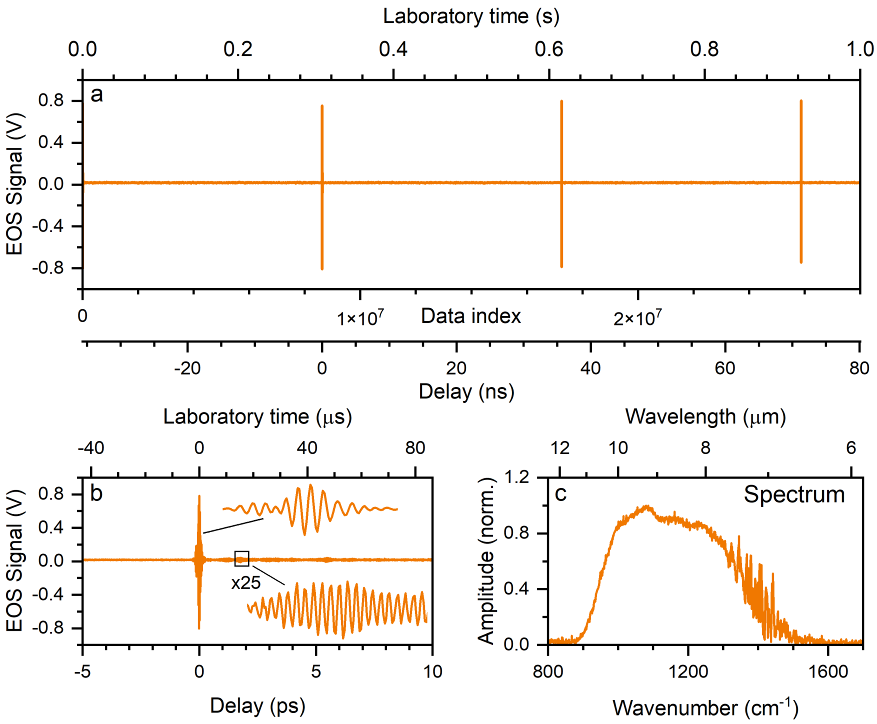

Figure 4.2: (a) Waveform measurement acquired in 1 second by asynchronous optical sampling (b) An enlarged view of the few-picosecond delay interval surrounding the peak of the EOS signal in a delay scan. (c) Spectrum obtained by performing a Fourier transform on a single delay scan.

switching the repetition frequency of the gate pulses back and forth between values that are slightly higher and lower than that of the mid-infrared driving laser. Fig. 4.3 shows a representation of the same. The mid-infrared pulses are depicted in orange, and the gate in green. The figure demonstrates the pulse slippage on detuning the repetition frequency of the gate pulse laser source initially with a higher value and later with a lower value than that of the MIR driving laser.

The technique of scanning a user-defined delay range by switching the relative repetition frequency between two lasers using an electronic feedback loop is referred to as electronically controlled optical sampling (ECOPS)[90]. Micrometer level changes are made in the length of the laser cavity by controlling the position of a cavity end mirror using a piezoelectric transducer.

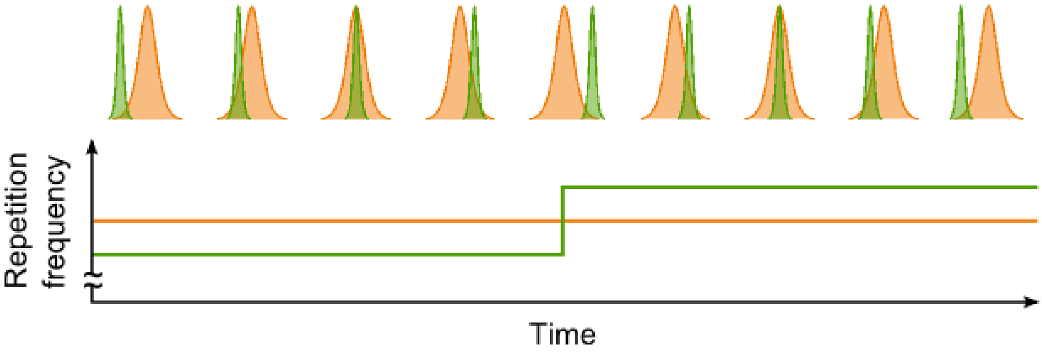

Figure 4.3: A representative scheme for restricting the delay range scanned by the gate pulse to the duration of the mid-infrared pulse (top). This is done by switching the repetition frequency of the gate pulses between values higher and lower than that of the mid-infrared pulses.

Instead of switching the cavity length abruptly, we vary the position of the corresponding end-mirror in a sinusoidal fashion, resulting in a frequency-modulated repetition rate.

In ECOPS, the frequency of switching or modulation (f_{scan}) directly translates as the scan rate, and the magnitude of the offset in repetition frequency, Δf determines the range of the delay scan. This is depicted in Fig. 4.4. The delay range is obtained by integrating Δf over time. Switching the value of Δf between two constant values like a square-wave function leads to a saw-tooth form for the scanned delay, as shown in the top panel of Fig. 4.4. The time taken to acquire a scan, $t_{scan} = (2f_{scan})^{-1}$. A sine-wave modulation, on the other hand, leads to a cosine waveform for the scanned delay, as shown in the bottom panel.

In the following section, we shall look into how the repetition rates are synchronized for dual-oscillator EOS.

4.1 Electronically controlled optical sampling

For our dual oscillator electro-optic sampling, we use the Yb:YAG thin-disk laser with Herriott-cell type pulse compression mentioned in Section 3.1 to generate the mid-infrared pulses, and a commercial femtosecond Erbium fiber laser (Menlo Systems C-Fiber) with a highly nonlinear fiber (HNF)-based broadening stage [12] for the gate pulses. The group of Prof. Alfred Leitenstorfer at the University of Konstanz provided the HNF. The spectrally broadened pulses from the Er:fiber laser were compressed to 12 fs, shorter

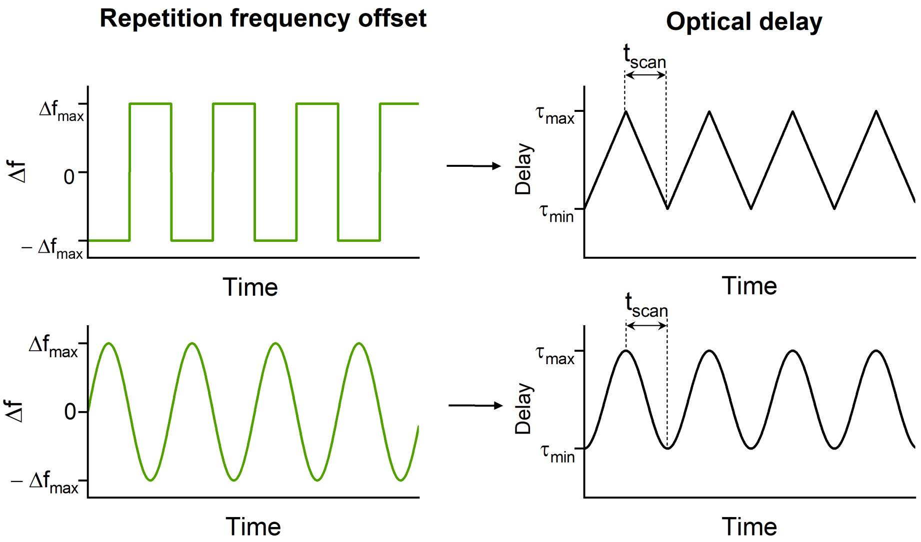

Figure 4.4: Switching the sign of the repetition frequency difference periodically (top, left) leads to a piece-wise linearly varying delay axis (top, right). Sinusoidally modulating the repetition frequency difference (bottom, left), leads to a sinusoidal delay axis with a $\pi/2$ phase-shift (bottom, right).

than a half-cycle of the mid-IR field using custom dispersive optics. Let us call the Yb:YAG thin-disk oscillator as Laser 1 and the Er:fiber oscillator as Laser 2. Laser 2 has a piezo-controlled end mirror to adjust the length of the laser resonator cavity, thereby controlling the repetition frequency. In addition to the piezoelectric transducer, a stepper motor connected to the same end mirror makes coarser adjustments to correct for drifts. Laser 1 acted as the master oscillator and Laser 2 as the slave. We tuned and modulated the repetition rate of Laser 2 using the RRE-SYNCRO (Menlo Systems GmbH) repetition rate locking electronic system.

4.1.1 Fundamental and harmonic frequency feedback

To measure rapidly, and to limit the scanned delay range to within 10 ps, the ECOPS mode was implemented.We used higher harmonics of the laser pulse signals for the repetition frequency feedback control loop for more precise frequency control. However, on the ECOPS technique, one has to consider that only a small fraction of the total delay between the mid-IR pulses is scanned. On locking on to the n^{th} harmonic of the repetition frequency, we get n possible ranges within the 35.7 ns delay range where the scanning occurs. As a result, instead of locking onto and scanning a limited range of delay around the mid-IR pulse peak, the gate pulse now has the possibility to lock onto and scan the delay range around $(n-1)$ virtual pulses that emerge in addition to the real pulse. This is shown in Fig. 4.5.

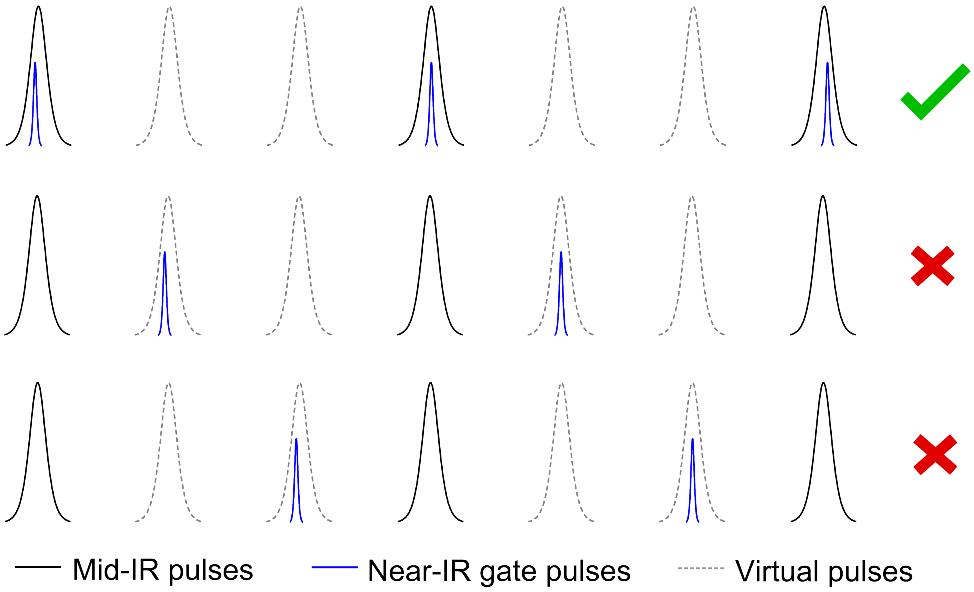

Figure 4.5: An example showing three potential scenarios of locking the third harmonic of the laser repetition rate for ECOPS. Only one among them scans the intended delay range.

We adopted the following procedure to ensure the consistency of the frequency lock. We set up two feedback loops, one working at the fundamental repetition rate of the Er:fiber laser of 56 MHz, to first synchronize the two lasers without any frequency offset and a second modulated harmonic loop for ECOPS. We first engaged the fundamental synchronization lock and then switched to the harmonic ECOPS lock while the lasers remained locked. This ensured that the delay range was reproducible.

The RRE-SYNCRO proportional, integral, and derivative (PID) controller has two locking channels, enabling the smooth switching from the fundamental to the harmonic lock. Fig. 4.6 shows the frequency locking schemes for ECOPS, including the fundamental (a) and the harmonic (b) frequency-based feedback loops. In the fundamental loop, the two lasers were locked to each other at the fundamental frequency of laser 2, which is at 56 MHz. The signals were mixed to form the error signal for the fundamental loop and fed into Channel 1 of the PID controller. The PID controller

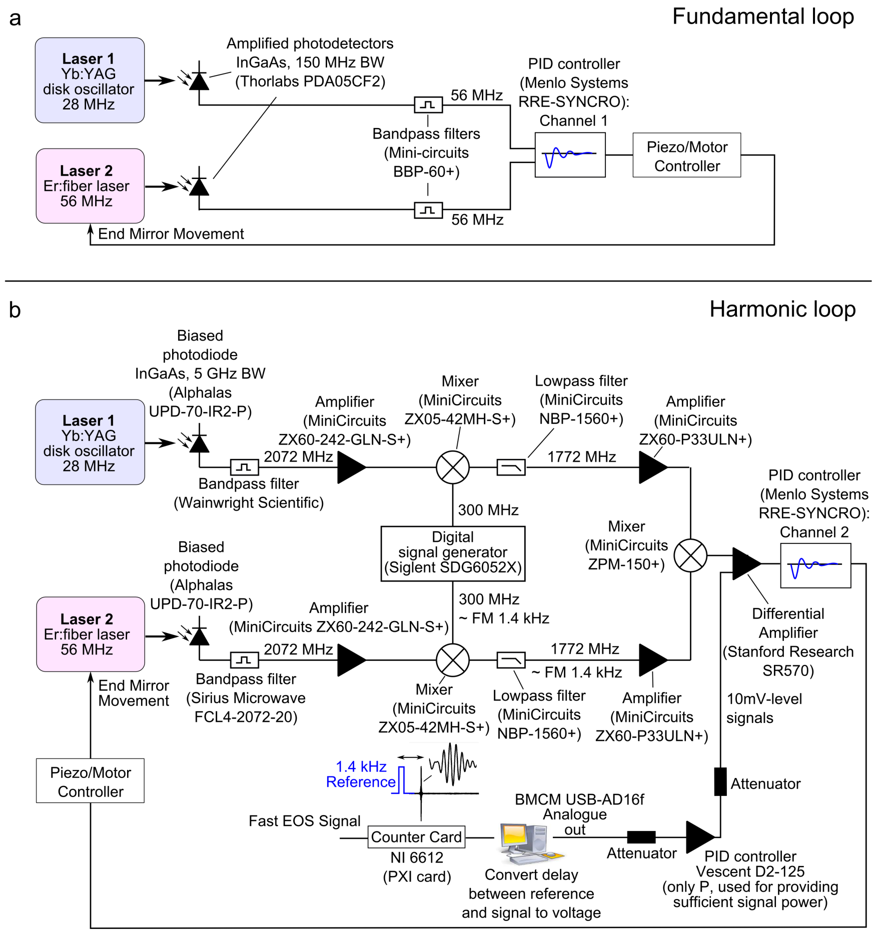

Figure 4.6: ECOPS frequency locking scheme. (a) Fundamental loop operating at 56 MHz. (b) Harmonic loop operating at 2072 MHz.

adjusted the position of the end mirror of the Laser 2 cavity, thus regulating the repetition frequency.

In the harmonic loop shown in Fig. 4.6(b), the 74^{th} and 37^{th} harmonic signals of Laser 1 and Laser 2 respectively, at 2072 MHz, were filtered out and amplified. Each of the two signals was mixed with the output signals from 2 channels of a digital signal generator (Siglent SDG6052X). One output was a sinusoidal wave at 300 MHz. A 1.4 kHz frequency modulation was applied to the second output of the digital signal generator, also centered at 300 MHz, which served as the repetition frequency difference, Δf_h. These signals were filtered to remove unwanted frequency components and amplified, before being mixed together to obtain a preliminary error signal.

Fig. 4.6(b) displays an additional step, where this error signal is fed into a differential amplifier in combination with another signal for enhanced stability. The following subsection describes this step.

4.1.2 Optical feedback for delay stabilization

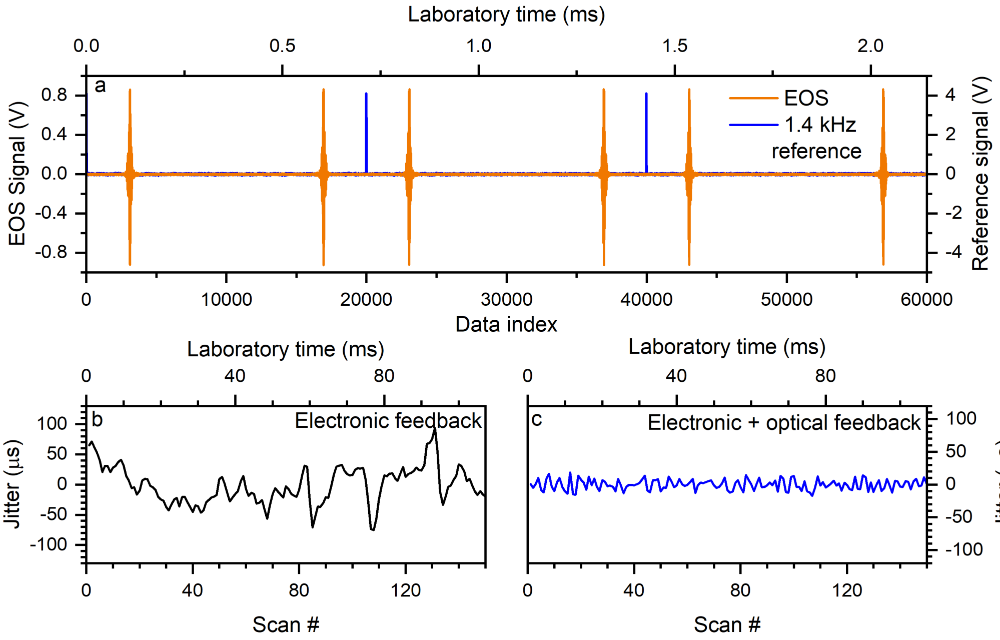

Figure 4.7: Optical-signal-based feedback for ECOPS. (a) EOS signal obtained by ECOPS with frequency modulation at 1.4 kHz (orange), and a 1.4 kHz reference pulse from a synchronized digital signal generator. (b) Time interval between reference pulses and subsequent EOS pulses with solely electronic-signal-based feedback. (c) The same time-interval, but in the case with additional optical-signal-based feedback.

The orange plot in Fig. 4.7(a) shows a few scans of the EOS signal measured using the ECOPS technique. The modulation frequency of 1.4 kHz implies that 2,800 delay scans (1,400 in the forward direction and 1,400 in the backward direction) are performed each second, implying an acquisition time of 367 µs for a single scan. To measure the reproducibility of the delay scans, we introduced a pulsed signal at the scanning frequency of 1.4 kHz, generated using a digital signal generator(Agilent 33250A) with a clock that is synchronized to the two-channel digital signal generator mentioned previously. This pulsed reference signal at 1.4 kHz is displayed in blue in Fig.

4.7(a).

To quantify the reproducibility of the scans, the time interval from each reference pulse to a threshold point near the peak of the EOS signal in the subsequent scan was measured using a counter card(National Instruments PXIe 6612). This quantity is plotted in black Fig. 4.7(b). This corresponds to the case of using the preliminary (electronic) error signal mentioned in Section 4.1.1 to lock the harmonic feedback loop.

We used the output of the counter card as an additional optical-signal-based feedback for the harmonic loop. The digital signal from the counter card was converted to an analogue voltage using an analogue-to-digital convertor (BMCM USB-AD 16f). The signal level was then adjusted using attenuators, and using only the proportional component of a PID Controller (Vescent D2-125). The output of the Vescent D2-125, which can be engaged and disengaged at will, was fed into a differential amplifier, along with the preliminary error signal mentioned before. On engaging the optical-signal-based feedback, the output of the counter card transforms to a more stable one, as shown in 4.7(c).

4.2 Electro-optic delay tracking

In our implementation of ECOPS the optical delay was scanned by varying the repetition rate of the laser oscillator generating the gate pulses for EOS at a rate of 1.4 kHz, thus giving 2,800 delay scans per second, 1,400 in one direction and 1,400 in the reverse direction. The jitter of the pulses along the delay axis is on the order of tens of femtoseconds. For sensitive spectroscopic measurements, we require the delay axis to have attosecond-level precision.

For the case of the sonotrode, delay tracking was done interferometrically, with one arm of the Mach-Zehnder interferometer tracing the path of the MIR pulse and the other, that of the gate pulse, both of which originated from the very same laser source. The sonotrode, or a conventional translation stage for that matter, changes the path length of the gate beam, thus affecting the interferometric signal.

In the current scenario, we have two different mode-locked lasers as the sources for the mid-infrared and the EOS gate pulses, with the delay being scanned by means of a relative difference in the repetition rates. This requires interferometry with two optical frequencies, as the interferometric signals depend on the relative optical delay and the relative phase determined by the carrier-envelope-phase. Even in a case where we would have a stable phase relationship between the pulses, the delay range would be restricted to the region where the pulses overlap in a sufficiently strong way.

For mapping electric fields by EOS, we require the sampled waveforms to have a stable phase but not the gate pulse. Our mid-infrared pulses are inherently phase-stable due to the fact that in intrapulse difference frequency generation, the two frequencies contributing to DFG interact to cancel away the carrier-envelope phase, as in the interaction of two comb-lines from the same frequency comb[81, 75].

The pursuit of an effective technique for the calibration of the optical delay, combined with the knowledge of the inherent waveform stability of the IPDFGn process led to the conception of a new idea in the team I am part of, one we refer to as electro-optic delay tracking (EODT). Our strategy to track the delay involves generating a quasi-monochromatic mid-IR waveform that covers a 10-picosecond delay range, capturing this waveform by dual-oscillator EOS simultaneously with the spectroscopic mid-IR waveform, and using the oscillations of the delay tracking waveform at the known, constant frequency to track the delay corresponding to each acquired data point.

The few-cycle NIR pulse used to generate mid-infrared radiation for field-resolved spectroscopy was recycled and recompressed using custom-designed dispersive mirrors. The recompressed NIR pulse is focused into a second crystal of LGS for IPDFG. We used a thicker crystal here, prioritizing higher dynamic range over bandwidth. We obtained few-cycle mid-infrared pulses with an average power of 50 mW.

Co-workersspecializingg in designing custom dispersive optics developed a Fabry-Pérot etalon that filters out a narrow spectral range centered at 8.33 µm[3] from the few-cycle mid-infrared pulse. On transmission through the etalon, the pulse is elongated by two orders of magnitude to cover 12 picoseconds of delay. To characterize the newly generated waveforms, we recorded the electric field by EOS with a previous version of the instrument[76] where the delay is scanned using a conventional translation stage and tracked interferometrically[83]. This is shown in Fig 4.8.

Fig. 4.8(a) shows the designed (top panel) and measured (bottom panel) curves for transmission and group delay, for a pair of Fabry-Pérot filters (FPFs). The measured transmission wavelength, which we shall represent by λ_{EODT}, is slightly shifted from design, at 8.53 µm, which might be due to possible discrepancies in the thickness of the layers of Ge and ZnS that make up the filter. Fig. 4.8(b) shows the effect of the filter, transforming the few-cycle mid-IR pulse shown in black to the multi-picosecond delay-tracking waveform shown in orange. Taking the Fourier transform of the waveforms in Fig. b gives us the spectra shown in Fig. 4.8(c). Fig 4.8(d) zooms in onto three sections of the delay-tracking waveform, spanning across 12 ps. The carrier frequency of oscillation remains constant across the entire delay range which has been shown.

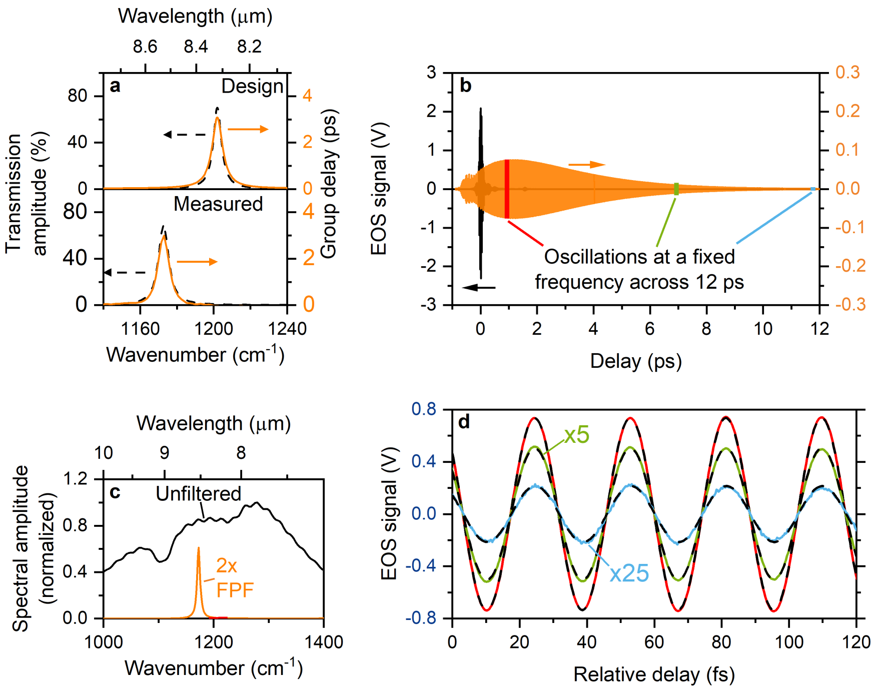

Figure 4.8: Characterizing the delay tracking waveform. (a) Design curve and measured values of transmittance (dashed black) and group delay on reflection (orange) of the Fabry-Pérot-type filter. (b) Time-domain EOS traces of the broadband unfiltered mid-IR waveform (black) and narrowband delay-tracking waveform (orange) obtained by transmission of the broadband pulse through two Fabry-Pérot-type filters (c) Normalized spectral amplitude of the broadband (black) and filtered (orange) pulses (d) Magnified view of three 120-fs long sections of the delay-tracking waveform shown in (b), marked in red, green and blue. The black dotted curves represent a sinusoidal waveform with a single frequency of 35.2 THz, multiplied by the pulse envelope of the experimental delay-tracking waveform.

For the delay extraction process, which will be described in Section 4.4, we assume a constant frequency of oscillation of the delay-tracking waveform. We simulated the waveform by multiplying a sinusoidal oscillation at a frequency of 35.1806 THz with the experimentally measured envelope of the delay-tracking waveform. The envelope, $a(n)$ was obtained by applying the Hilbert transform on the delay-corrected waveform as follows:

$$a(n) = \sqrt{(I_{\mathrm{EODT}}(n))^2 + \mathcal{H}\left(I_{\mathrm{EODT}}(n)\right)^2} \tag{4.5}$$

The simulated waveform is plotted as black dashed lines in Fig. 4.8d. The simulated waveform overlaps with each of the sections of the measured waveform across the 12 ps delay range, validating the single-frequency approximation. After characterizing the manufactured filters and extracting the transmission frequency, they were implemented in the dual-oscillator EOS setup for electro-optic delay-tracking.

4.3 Dual-oscillator scanning: Experimental setup

The experimental scheme for dual-oscillator EOS with EODT is shown in Fig. 4.9, with (a) showing a simplified version of the scheme, and (b), a more detailed representation of the same. In addition to the Yb:YAG thin-disk oscillator with Herriott-cell pulse compression stages, as shown in 3.1, we introduce a second oscillator, a commercial Er:Fiber laser (Menlo Systems C-Fiber), whose pulse repetition rate is actively controlled. The two laser oscillators are referred to as Laser 1 and Laser 2 respectively.

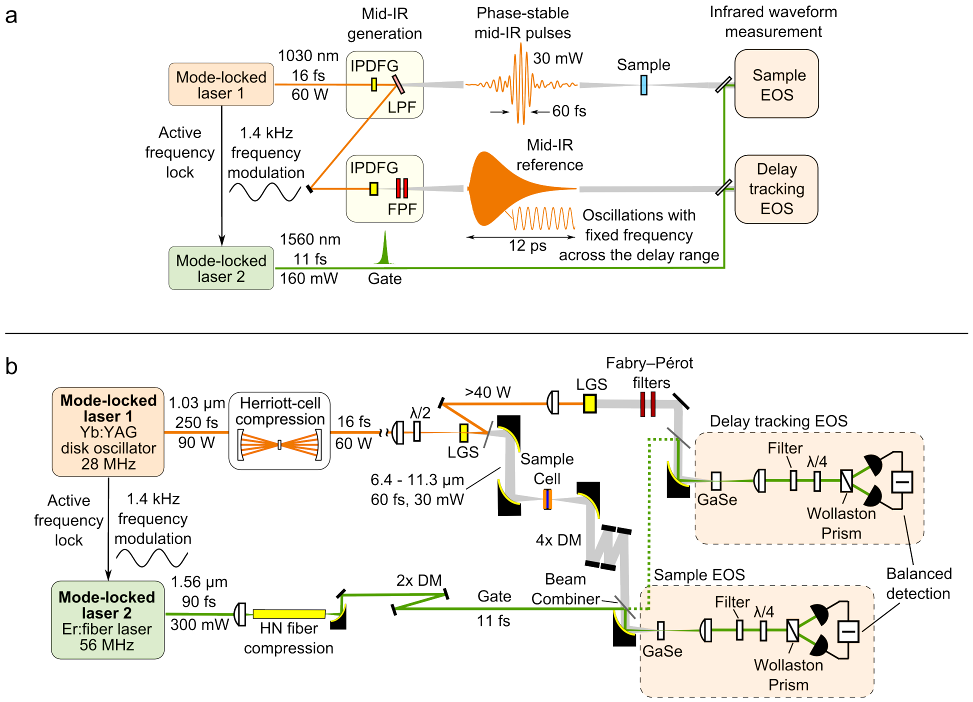

Figure 4.9: Experimental Scheme: (a) Simplified scheme for dual-oscillator EOS. FPF: Fabry-Pérot Filter; LPF: Lowpass filter. (b) Detailed experimental scheme. HN: highly nonlinear; DM: dispersive mirrors.

After the compression stages, the pulses have a duration of 16 fs, with an average power of 60 W. These compressed pulses with a spectrum ranging from 935 nm to 1145 nm (-20 dB) are focused using a lens with a focal length of 900 mm into a 1 mm thick $LiGaS_2$ crystal to create broadband few-cycle mid-infrared pulses by the process of intra-pulse difference frequency generation (IPDFG). The generated mid-IR pulses cover a spectral range spanning from 6.4µm to 11.3µm, with an average power of 30 mW. The mid-IR beam is collimated by an off-axis parabolic mirror (OAPM) and subsequently focused using a 40 mm OAPM into a 30 µm liquid sample cell with 1 mm thick ZnSe windows (MIRA eCell, CLADE GmbH). The transmitted light is recollimated using a second OAPM. A set of 4 custom dispersive mirrors (DM) designed and manufactured in-house then compress the mid-IR pulse, compensating for the dispersion acquired on passing through the windows of the sample cell, and half the thickness of the mid-IR generating $LiGaS_2$ crystal, down to 60 fs, before EOS detection. The entire mid-IR beam path from MIR generation to EOS, lies inside nitrogen-filled chambers to prevent infrared absorption by water vapour.

The gate pulses for EOS originate in Laser 2. The Er:fiber oscillator directly outputs pulses centered at a wavelength of 1.56 µm with a duration of 90 fs, at a 56 MHz repetition rate, and with an average power of 300 mW. The pulses were passed through a prism compressor to fine-tune the dispersion before being coupled into a highly non-linear fiber, where they were spectrally broadened to span from 1.25 µm to 1.79 µm (20 dB), with an average power of 165 mW. The pulses were temporally compressed to 11 fs using a pair of custom dispersive mirrors and transmitted through 20 mm of fused silica. The s-polarized gate beam was combined with the p-polarized MIR beam originating from Laser 1 at a 0.8 mm thick wedged ZnSe substrate with a diameter of 50.8 mm, which acts as a beam combiner. The MIR beam, which is incident at an angle of 65 degrees on the ZnSe beam combiner, was transmitted, while the gate beam was reflected in a to trace the path of the MIR beam. The co-propagating beams were focused by an OAPM with a principal focal length of 25.4 mm to a 250 µm thick z-cut GaSe crystal for EOS. The θ and ϕ angles of the GaSe crystal were adjusted for optimum phase matching in the spectral range of the mid-IR pulse.

In the $LiGaS_2$ crystal for mid-IR generation, only a small part of the 60 W NIR beam was converted into the mid-IR. The remaining power (>40 W) was reflected off a custom dichroic mirror, recompressed using 3 mm of fused silica and custom dispersive mirrors, and focused using a 450 mm focal length concave mirror into a 2mm-thick $LiGaS_2$ crystal for again generating mid-IR radiation by IPDFG. The NIR radiation that remained after the second $LiGaS_2$ crystal was directed to a water-cooled beam dump. MIR radiation spanning a spectral range from 970 cm^{-1} to 1270 cm^{-1}, with an average power of 50 mW was collimated by a concave mirror and transmitted through two Fabry-Pérot filters to generate a long-lasting, narrowband waveform that spanned the entire multi-picosecond delay range for delay-tracking.

A part of the gate beam (38 mW) was transmitted through the ZnSe beam combiner mentioned earlier, to be used as the gate for the delay-tracking waveform. The gate pulse was temporally compressed using a pair of custom dispersive mirrors and transmission through 12mm of fused silica to compensate for the dispersion acquired in the ZnSe beam combiner. The path length of the gate beam is carefully adjusted for temporal overlap with the delay-tracking mid-IR pulses. The delay-tracking MIR and gate beams were combined at a holographic wire grid polarizer (Thorlabs WP25H-Z), through which the MIR beam was transmitted and off which the gate was reflected at a low angle of incidence. The co-propagating beams were focused using an OAPM with a principal focal length of 50.8 mm into a 500 µm thick EOS crystal of z-cut GaSe.

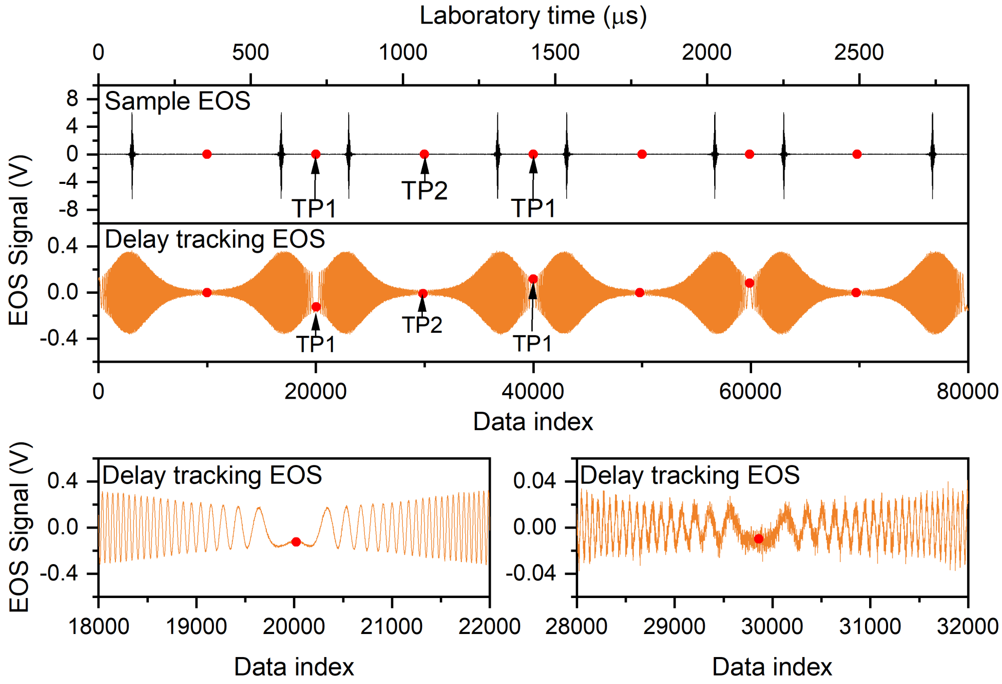

Figure 4.10: (Top) Simultaneous acquisition of EOS traces in the sample (black) and delay-tracking (orange) arms. The turning points, where the scan direction switches, are marked as solid red circles. (Bottom) The plots zoom into sections around two turning points

In both the EOS crystals, i.e., in the sample and delay tracking channels, mid-IR light interacts with the gate and was up-converted to the NIR by SFG. The up-converted light is polarized perpendicular to the gate pulses, resulting in a change in the polarization state in the overlap region. A convex lens was used to collimate the NIR beam after the EOS crystal. Short-pass filters with a cut-off frequency of 1350 nm and 1550 nm were used to filter away the non-interacting spectral components of the gate and hence reduce their contribution to the shot-noise[74]. The waveforms were then measured in an ellipsometric setup using a $\lambda/4$ plate, a Wollaston prism, and balanced detection.

We measured the infrared waveforms in both the EOS channels simultaneously, using a 4-channel digitizer (GaGe Razor Express CSE 1642) with a bandwidth of 125 MHz. We connect an additional photodiode output of the gate-pulse to the digitizer, using it as an external clock to capture every laser shot. Although generated in different crystals, the two mid-infrared pulses originated from the same driving NIR pulses and were gated by the same gate pulses during EOS. The modulation frequency for ECOPS of 1.4 kHz, which corresponds to 2,800 scans per second, 1,400 in the forward direction, and 1,400 in the reverse direction. Each single scan thus contained roughly 10,000 data points. Fig 4.10 depicts the continuous acquisition of EOS traces with a sinusoidally varying optical delay.

Having obtained the raw EOS signals and the calibration signal, the next task is to combine the information from both channels to obtain the sample EOS signal as a function of the delay for each scan.

To quantify the stability of the ECOPS modulation scheme, in terms of optical delay, the fluctuations in the delay position of the turning points were evaluated for 560,000 EOS traces (i.e., 280,000 forward and 280,000 backward scans) acquired in 200 seconds. The interval/distance between consecutive pairs of turning points, which corresponds to the delay range of a scan, was also calculated. The two quantities are plotted in 4.11.

In the next section, we shall describe the algorithm that tracks the optical delay of the gate pulses with respect to the mid-IR pulses in post-processing.

4.4 Dual-oscillator scanning: Delay extraction

Precise knowledge of the delay corresponding to each single data point is required to perform sensitive spectroscopic measurements. Electronic modulation of the repetition frequency for ECOPS results in multi-femtosecond jitter in optical delay from one scan to the next[64]. This turns out to be larger than the period of oscillation of the mid-IR electric fields. The in-

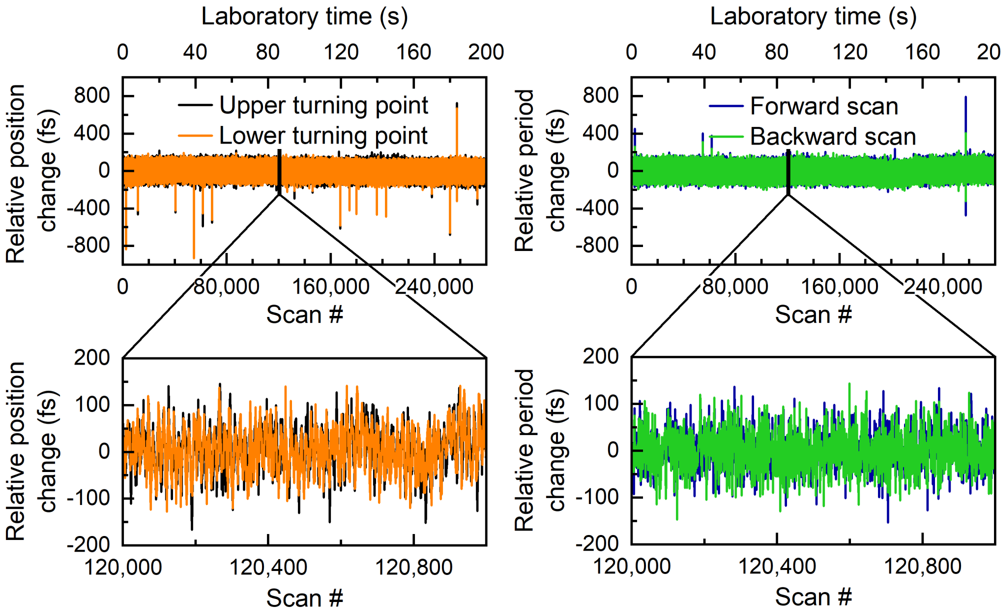

Figure 4.11: Fluctuations in turning point (left) and delay range (right) across 560,000 scans acquired in 200 seconds. The insets zoom into 0.8-second segments

tention here, is to use the optical electric-field information of a narrowband phase-stable mid-IR waveform to calibrate the relative delay between the sample mid-IR and gate pulses.

The fact that the mid-IR and gate pulses for both sample and delay tracking EOS channels originate from the same two lasers, with a fixed optical delay in the optical setup, ensure that the delay will be scanned in both channels identically, with mechanical disturbances and fluctuations in the beam path being the remaining potential sources of error. In the case of the sonotrode, which was described before, an interferometric signal from an auxiliary laser was used to track the delay.

The knowledge of the amplitude and frequency of the sinusoidal oscillation of the delay-scanning sonotrode mirror was utilized in the described predictor-correcter algorithm. In the current scenario, we similarly put the knowledge of the sinusoidal modulation of the repetition frequencies to use, for EODT. Here, the narrow-band delay tracking EOS signal replaces the auxiliary monochromatic laser. The steps of the delay-calibration algorithm are described below.

The first task is to cut the continuously acquired signals into individual scans. To do this, we identify the turning points where the direction of the scan changes. This is done by locating the points of mirror symmetry, by minimizing the least square error, just as was done in the case of the sonotrode. A zoom-in of the two turning points is shown in the bottom panels in Fig 4.10. Assuming the modulation of the repetition rates to be perfectly sinusoidal, we estimate the optical delay, τ_{est}, corresponding to the data index, n, as follows:

$$\tau_{\text{est}}(n) = A_\tau \cos\left(\frac{2\pi}{T}(n - n_{\text{tp1}})\right) + \tau_0 \tag{4.6}$$

Here, A_τ represents the delay amplitude, which is determined by the frequency modulation depth in ECOPS, n_{tp1} is the data index of the closest instance of turning point 1(TP1), T represents the period of the modulation, which is the reciprocal of the modulation frequency, and τ_0 is a constant delay offset. T can quite accurately be estimated by subtracting the indices corresponding to every second turning point. The total delay range scanned corresponds to twice of A_τ.

The delay tracking MIR signal, I has a narrow spectral range, which can be estimated to a single wavelength, λ_{EODT}. I can, thus, be described by a pulse envelope multiplied by the sine as a function of delay, τ with a constant carrier frequency of ω_{EODT}, and a constant phase offset, ϕ_0.

$$\omega_{\text{EODT}} = \frac{2\pi c}{\lambda_{\text{EODT}}} = 2.21 \times 10^{14}\,\text{rad/s} \tag{4.7}$$

$$I(n) = a(n)\sin\left(\omega_{\text{EODT}}\tau(n) + \phi_0\right) \tag{4.8}$$

Let us define the delay-dependent argument of the sine function as $\psi(\tau)$, i.e.,

$$\psi(n) = (\omega_{\text{EODT}}\tau(n) + \phi_0). \tag{4.9}$$

Let $\mathcal{H}\left(I(n)\right)$ represent the Hilbert transform of I(n). Then:

$$a(n) = \sqrt{I^2(n) + \left(\mathcal{H}\left(I(n)\right)\right)^2} \tag{4.10}$$

$$\psi(n) = \text{atan2}\left(I(n), \mathcal{H}\left(I(n)\right)\right), \tag{4.11}$$

where atan2 is the 2-argument tangent function that gives the argument of $x + iy$ in the interval $(-\pi, \pi]$. The delay can be calculated as:

$$\tau(n) = \frac{\psi(n) - \phi_0}{\omega_{\text{EODT}}} = \frac{\text{atan2}\left(I(n), \mathcal{H}\left(I(n)\right)\right) - \phi_0}{\omega_{\text{EODT}}} \tag{4.12}$$

We obtain an initial estimate for the delay range as follows:

$$A_\tau = \frac{max(\tau(n)) \; - \; min(\tau(n))}{2} \tag{4.13}$$

Eq 3.11 describes that the delay tracking EOS signal, I, oscillates sinusoidally with a constant frequency ω_{EODT} w.r.t the optical delay τ. When we look at the evolution of I w.r.t the data index, n, however, the frequency of oscillation, which we shall call $\acute{\omega}_{EODT}$, is no longer constant, and is given by:

$$\begin{aligned} \acute{\omega}_{EODT}(n) &= \left|\frac{d\psi(\tau)}{dn}\right| = \left|\frac{d\psi(\tau)}{d\tau}\frac{d\tau(n)}{dn}\right| \\ &= \left|\frac{2\pi A_\tau \omega_{\mathrm{EODT}}}{T}\sin\left(\frac{2\pi}{T}(n-n_{tp1})\right)\right| \end{aligned} \tag{4.14}$$

The delay-tracking waveform can be described as follows:

$$I(n) = a(n)\sin\left(\acute{\omega}_{\mathrm{EODT}}(n)n + \vartheta(n)\right) \tag{4.15}$$

Here, $\vartheta(n)$ is the data-index-dependent phase offset. If we take a small section of the trace, such as half the oscillation period of the delay-tracking waveform, we can approximate the amplitude and frequency of oscillation to be a constant in each section , which we denote by i, as follows:

$$I(n) = a_i \sin\left(\acute{\omega}_{\mathrm{i,EODT}} n + \vartheta_i\right), \tag{4.16}$$

where a_i denotes the average amplitude of the section of the signal, $\acute{\omega}_{i,EODT}$, the oscillation frequency at the mid-point of the section, and φ_i, the constant offset. We obtain the section-wise values of a_i and φ_i from an experimentally measured trace by numerical fitting. To minimize computational complexity, a linear fit was used:

$$I_{\mathrm{fit}}(n) = A\sin\left(\acute{\omega}_{\mathrm{i,EODT}} n\right) + B\cos\left(\acute{\omega}_{\mathrm{i,EODT}} n\right) \tag{4.17}$$

$$a_i = \sqrt{A^2 + B^2} \tag{4.18}$$

$$\vartheta_i = \mathrm{atan2}(A, B) \tag{4.19}$$

The envelope $(a(n))$ and correction phase $\vartheta(n)$ for the delay-tracking waveform are obtained by interpolating a_i and ϑ_i respectively. The measured $(I(n))$ and reconstructed (I_{fit}) delay tracking signals are plotted in Fig 4.12, and overlap well . Equation 4.12 is applied to extract the delay axis from $I_{\mathrm{fit}}(n)$ and its Hilbert transform.

After extracting the delay axis for the EOS traces, post-process was performed analogously to the case of the sonotrode in Section 3.3.5. As part of

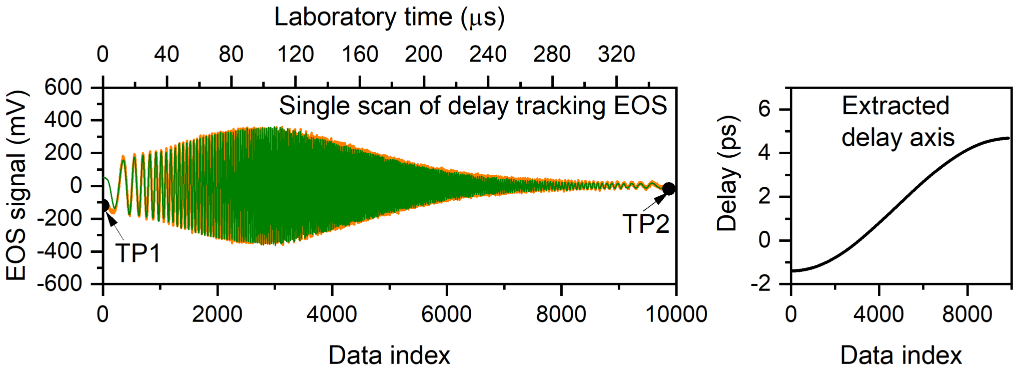

Figure 4.12: Reconstruction of delay tracking signal(left), and the extracted delay axis (right)

this, a delay shift correction was performed on the individual traces. This has been plotted in Fig. 4.13, for the case of 280,000 forward and 280,000 backward scans acquired over 200 seconds. The inset on the bottom zooms into a 0.8-second section of the plot. The maximum amplitude of correction applied on the 200-second measurement was 4 femtoseconds. We attribute this to shifts between the paths of the sample and delay calibration arms of the spectrometer.

Waveform reconstruction

The strength of the full EOS signal impinging on a balanced photodetector is beyond the working limits of the inbuilt 200 MHz-bandwidth transimpedance amplifier, causing the measured waveform to be clipped due to signal saturation. With the high bandwidth and dynamic range, technical limitations call for a compromise. We realized this by detecting stronger and weaker parts of the signal separately. This is depicted in Fig. 4.14(a).

The two beams of light were each split off by a beam sampler, a fused silica substrate with anti-reflection coating on one face, before being directed to the diodes of the balanced photodetector. The beams reflected off of the beam sampler are directed to a second balanced photo-detector which is identical to the first one. The signal from the second detector, being considerably weaker, lies within the working range of the amplifier, and does not exhibit a saturation effect. Fig. 4.14(b) and Fig. 4.14(c) show the EOS signal as a function of the optical delay, which is obtained by post-processing using the algorithm mentioned in section 4.4, measured using balanced detectors 1 and 2.

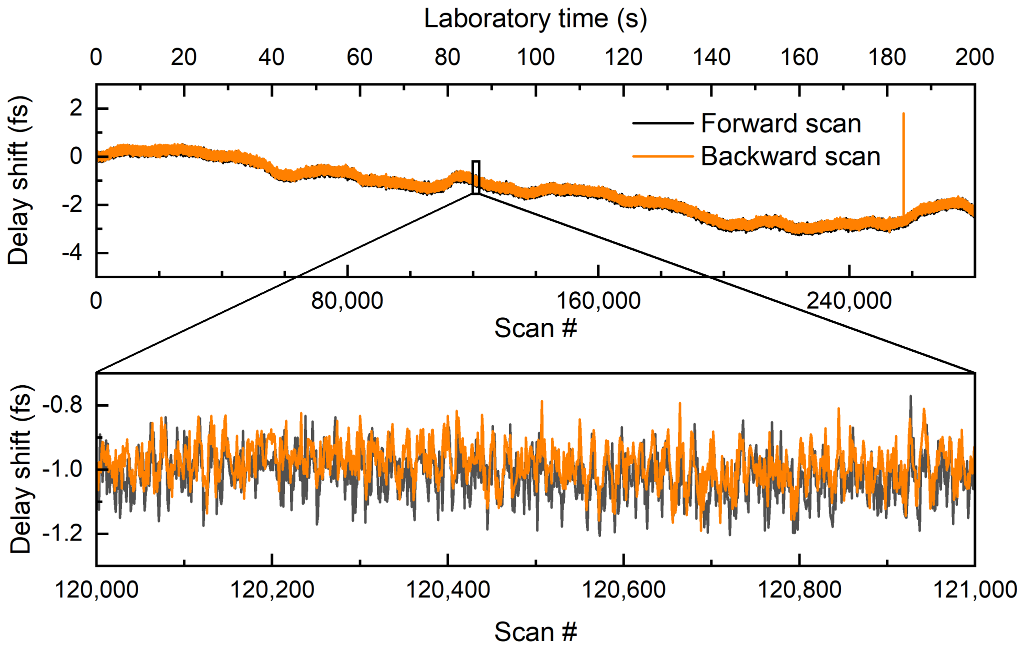

Figure 4.13: The delay shift applied as a correction to each scan to compensate for mechanical drifts between the Sample and delay-tracking EOS waveforms plotted as a function of time, or the number of delay scans, for a measurment lasting 200 s. The inset on the bottom zooms into a segment comprising of 1000 forward scans and 1000 backward scans.

The plots correspond to a single delay scan performed in 357 µs, with each data point corresponding to a single laser gate pulse and a single MIR pulse. To precisely combine signals from balanced detectors 1 and 2 to reconstruct the signal, we identified the maximum level of the saturated signal from Detector 1 and set a fraction of it as the threshold. In this case, the fraction was chosen to be 0.5. The signal reconstruction was done as follows.

In the optical delay region before the onset of the excitation, that is, to the left of the first crossing of the threshold, the signal from Detector 1 was selected. The same was done for the region beyond the excitation pulse, to the right of the last crossing below the threshold. In the region in between, where the signal strength is strong and often saturated, the signal from Detector 2 was considered. The signals from both detectors were compared in regions of weaker signal-strength to obtain the scaling factor that would match the two signals. The signal measured using Detector 2 was scaled, and 'stitched' on either side with signals from Detector 1 to obtain a reconstructed trace as shown in Fig. 4.14(d).

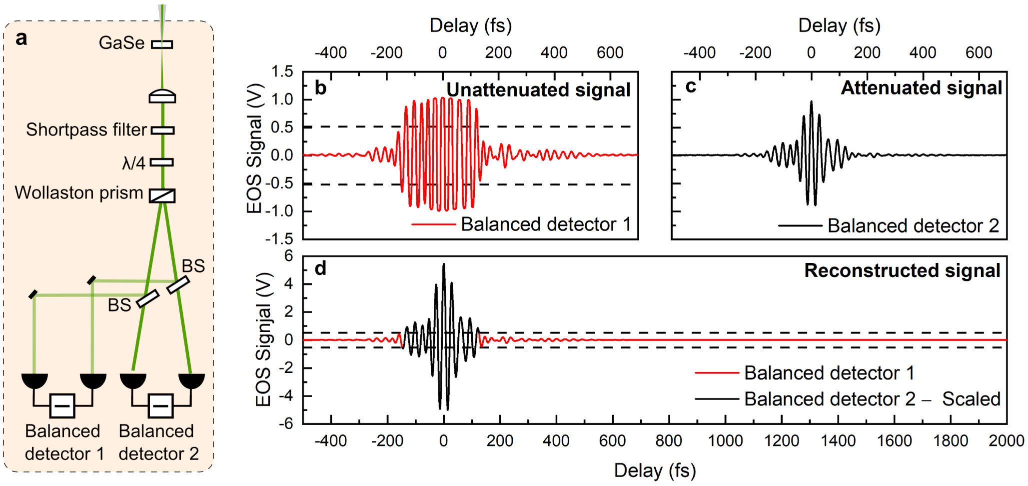

Figure 4.14: Reconstruction of EOS trace from the unattenuated and attenuated signals acquired using two balanced photodetectors

Noise - radio frequency analysis

To study the spectral distribution of the detection noise, the mid-IR sample beam was blocked, and the balanced output of the balanced photodetector measuring the sample was sent to a radio frequency spectrum analyzer. The voltage spectral density of the balanced output is plotted as a function of frequency in 4.15. For frequencies from 100 Hz to 100 kHz, the measurements were taken using a fast Fourier transform (FFT) spectrum analyzer (Stanford Research SR 760), and for higher frequencies, a GHz spectrum analyzer (Agilent E4447A) was used. The detection noise, measured by blocking the MIR beam (orange), approaches the calculated shot-noise (black-dashed) for frequencies above 40 kHz. There are spikes in the signal between 100 and 500 kHz, the origin of which is yet to be understood. The dark noise of the measurement scheme(grey) suggests a measuring error or artifact at frequencies below 2 kHz.

4.5 Dual-oscillator scanning: Results

4.5.1 Sensitivity and timing precision

We obtain the EOS signal for a 1 mg/ml aqueous solution of $DMSO_2$ as a function of optical delay, by calibrating each delay scan in a continuous measurement to the extracted delay axis. The EOS signal as a function of the delay is plotted in Fig 4.16(a), for a single scan acquired in 357 µs (gray),

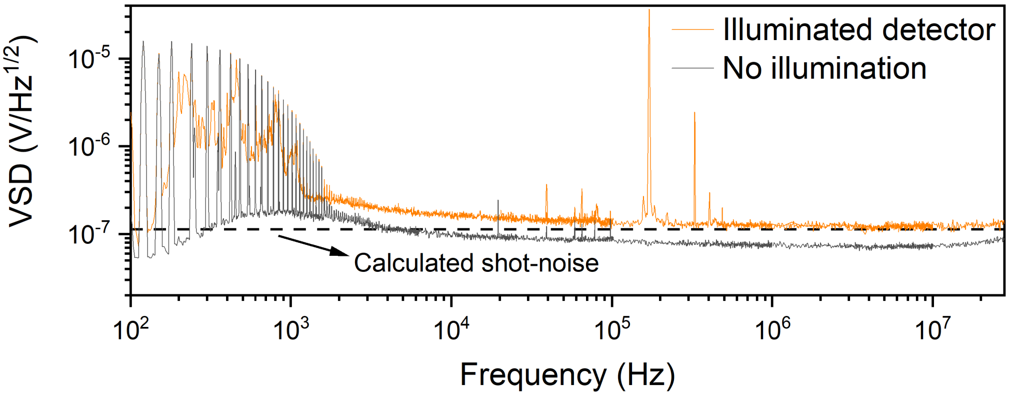

Figure 4.15: The detection noise of the field-resolving spectrometer measured using radio frequency spectrum analyzers, by blocking the MIR beam, is plotted as a function of frequency(orange). The noise approaches the calculated shot-noise (dashed black line) at frequencies higher than 40 kHz, except for a few spikes at frequencies between 100 kHz and 500 kHz. The dark noise of the measurement setup, obtained by blocking all beams, is plotted in grey. The spikes at lower frequencies are attributed to the measurement setup.

and an average of 560,000 scans (black). $DMSO_2$ is a polar molecule with two strong absorption bands within the spectral region covered by our mid-IR pulses, at 1140 cm^{-1} and 1290 cm^{-1}, which correspond to the symmetric and asymmetric stretching vibrations of the SO_2 group, respectively.

Fig. 4.16(a) shows individual-scan (black) and averaged-scan (gray) EOS traces. The traces overlap each other. The left inset in Fig 4.16(a) zooms into a delay segment preceding the excitation pulse, where the signal is expected to be zero. The fluctuations in the averaged trace cancel out, resulting in a much lower value in comparison to the individual scan. This behaviour is expected and validates the delay extraction process.

The inset on the right in Fig. 4.16 zooms in to a section of the EOS trace, spanning from 600 to 1000 fs in delay. The EOS signal clearly shows the resonant response of the sample, formed by a beating of the two strongly absorbing bands mentioned earlier. The field-resolved measurement performed using EOS makes it possible to separate the resonant response of the $DMSO_2$ from the strong excitation pulse

The spectral amplitude obtained by performing a Fourier transform on the EOS traces, is plotted in Fig 4.16(b). Here again, the solid gray line represents an individual trace, and the black line represents the 200-s-averaged trace. The spectral amplitude is normalized to the peak value of

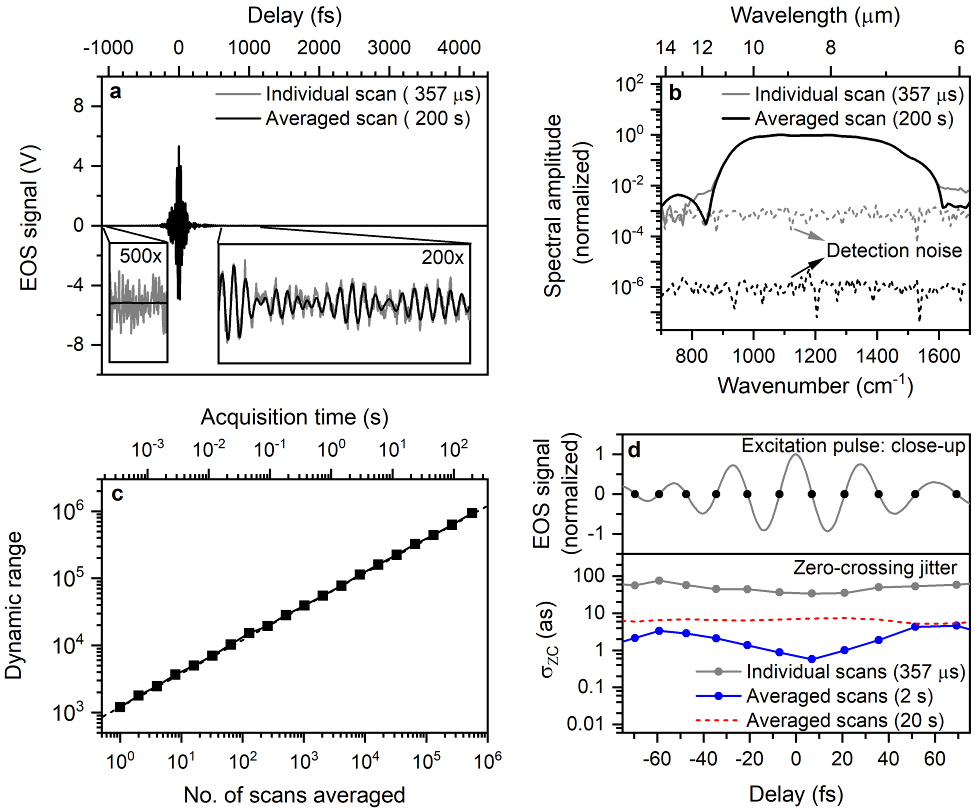

Figure 4.16: (a) Individual scan (grey) and averaged scan (black) EOS traces (b)Spectra corresponding to a single scan (grey) acquired in 357 µs and to an average of 560,000 scans (black) acquired over 200 s (c) Dynamic range as a function of the no.of scans averaged. (d) Timing precision represented by the standard deviation in the position of zero-crossings along the delay axis, for individual, as well as averaged scans

the averaged-trace spectrum. The noise of the EOS detection, obtained by blocking the mid-IR beam, is plotted as gray and black dashed lines for the case of the individual scan and 200-s-averaged scan, respectively. We define the dynamic range as the ratio of the peak spectral amplitude to the average spectral amplitude in the case where the MIR beam has been blocked. The field dynamic range as a function of the number of scans averaged is plotted in Fig 4.16(c). The dynamic range increases from 10^3 for an individual scan to 10^6 for a 200-s-averaged trace, strictly following a square-root relationship with the no. of scans averaged.

In order to showcase the timing precision of the EOS signals, we zoom

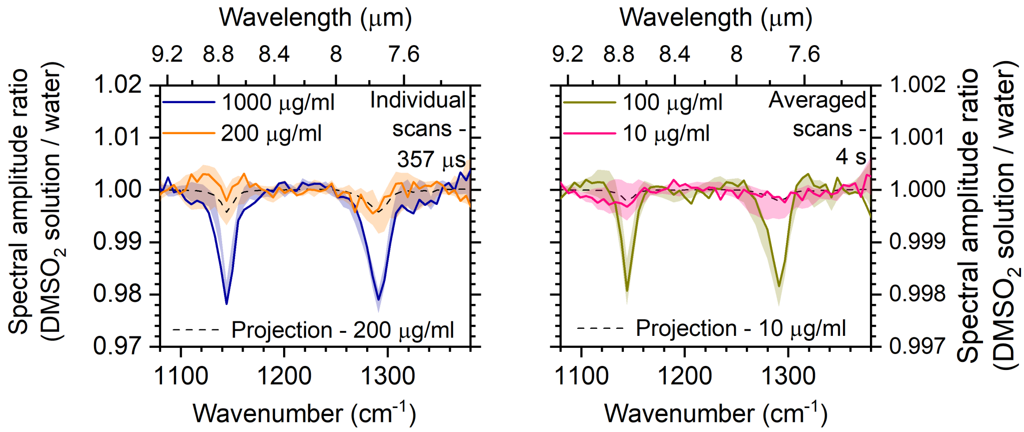

Figure 4.17: Ratio of the spectral amplitude for $DMSO_2$ solution to water for individual scans (left) and 3-s-averaged scans (right) corresponding to two pairs of concentrations, 1000 (blue) and 200 µg/ml (orange), and 100 (yellow) and 10 µg/ml (pink) respectively. Using the case of 1000 µg/ml as a reference, the deviation in the spectral ratio from unity are scaled down and plotted for the lower concentrations in both panels, as a black dashed line

into a 150-fs long segment of the EOS traces, around the excitation pulse where the signal is strongest. Each scan is aligned to the first scan using a constant delay shift that minimizes the squared-error between the trace, and the first trace, as mentioned before. The top panel in Fig 4.16(d) shows an exemplary section of an individual scan, with the zero-crossings being marked by black solid circles. The temporal position of each of the 11 zero-crossing shown in the plot is compared for 20 consecutive scans, and the standard deviation is calculated and plotted in the lower panel of Fig. 4.16(d). The same is done for a set of 20 averaged scans, for two cases, that is, averaging over 2-s and 20-s for each trace. This is depicted by the blue solid plot and the red dashed line respectively.

Fig. 4.17 the absorption by aqueous solutions of $DMSO_2$ with varying concentrations. In a step to standardize the spectrum, we divide the spectral amplitude of the $DMSO_2$ solution sample, by that of pure water. We then perform a polynomial baseline correction as in [98]. We plot the ratio of spectral amplitudes for $DMSO_2$ solution and water, for the case of individual scans (left panel), as well as 4-s averaged scans (right panel). In the case of individual scans, a solution of $DMSO_2$ in water with concentrations of 1 mg/ml and 200 µg/ml are plotted. Calibrating to the case of 1 mg/ml solution of aqueous $DMSO_2$, we estimate the spectral ratios for the case of the lower concentrations in each of the panels, of 200 µg/ml and 10 µg/ml, by downscaling the deviation from unity linearly w.r.t the concentration of $DMSO_2$.

Individual-scan referencing

Referencing the electric field or the corresponding spectral information from a sample measurement to that of a reference measurement without the sample of interest would help cancel out contributions in the signal, and the noise, of the excitation pulse, and separate the coherent molecular response of the sample. In past attempts within the group, this was done sequentially, where a measurement with the sample in the liquid cuvette was captured over multiple seconds, followed by a measurement with distilled water in the cuvette.

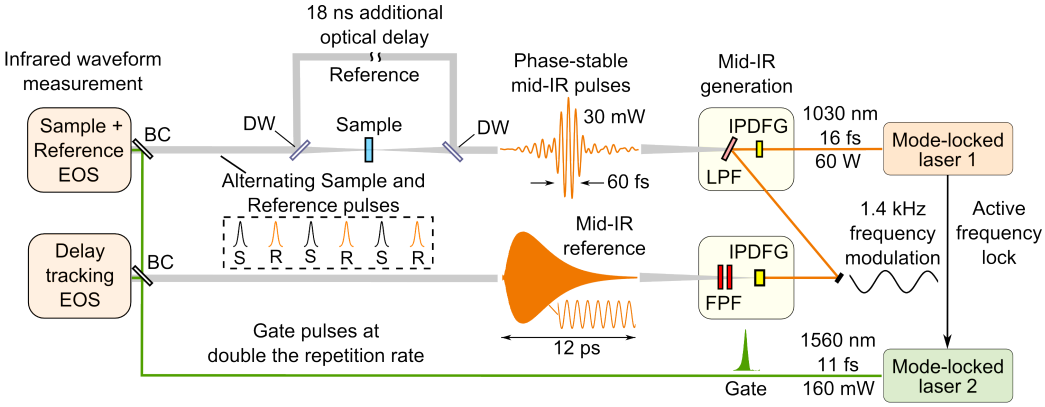

Figure 4.18: Simplified experimental scheme for dual-oscillator EOS with individual-scan referencing. DW - Diamond window, BC - Beam combiner

To harness the advantage of rapid acquisition of EOS traces enabled by the dual-oscillator ECOPS approach, the idea of a potential fast referencing scheme, working at the individual-scan-level, was introduced. The fact that the pulse repetition frequency of Laser 2, which provides the gate pulses for EOS, is twice that of Laser 1 is a key enabling feature. A simplified version of the experimental scheme for dual-oscillator EOS with individual scan referencing is shown in 4.18 A wedged chemical-vapour-deposition (CVD) diamond window (Diamond Materials GmbH) with a thickness of 500 µm was used to create a copy of the few-cycle mid-IR pulse, before the liquid cuvette, by reflection. While the transmitted beam passes through the liquid cuvette, the reflected beam is made to propagate through an additional 5.3 m of path length before the beams are combined with the help of a second wedged diamond window, which corresponds to 17.8 ns of optical delay, just the right amount for the next gate pulse to arrive. Thus, the gate pulses, arriving at 56 MHz interact with the Sample and Reference mid-IR pulses in an alternating manner in the same EOS crystal, and are subsequently detected using the same detection scheme.

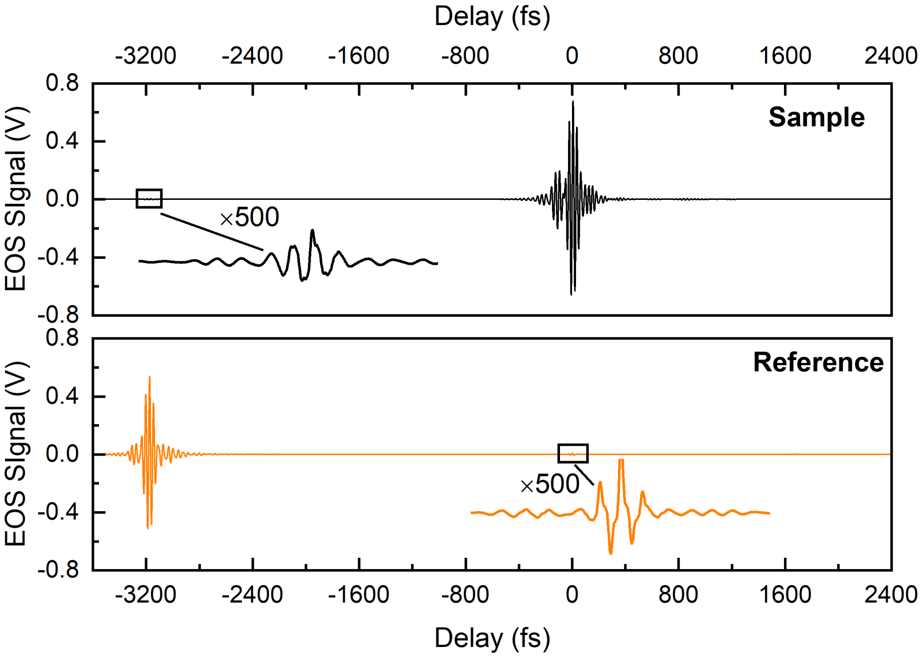

Figure 4.19: Crosstalk between the sample and reference channels for individual scan referencing is clearly seen in both channels

Individual-scan referencing would thus work on a pulse-to-pulse basis. A single laser shot of a Sample mid-IR pulse would be followed by a single laser shot of the Reference mid-IR pulse. Both these pulses originate from the same laser pulse but are now separated temporally by the additional propagation distance in the Reference arm. The recorded signal is thus an interspersed string of data, the odd and even data points of which need to be separated to obtain the signal in the Sample and Reference EOS signals. While the idea worked as planned, a setback was encountered due to the limited bandwidth of the amplification in the balanced photodetector, resulting in traces of the signal from the Sample EOS trace emerging in the Reference EOS trace and vice-versa. This is shown in Fig. 4.19, where the Sample and Reference EOS signals, obtained by averaging 14,000 scans each have been plotted in the top and bottom plots respectively

4.5.2 Capturing dynamics

The rapid scanning of delays with the dual-oscillator ECOPS approach taken here makes it possible to monitor sub-second dynamics. As a test to demonstrate this, a dynamic injection event was measured by injecting an aqueous solution of $DMSO_2$ into a water-filled liquid cuvette, while continuously acquiring EOS traces. The $DMSO_2$ solution had a concentration of 1 mg/ml. A custom sample delivery system by CLADE GmbH was used to inject the sample into the liquid cuvette.

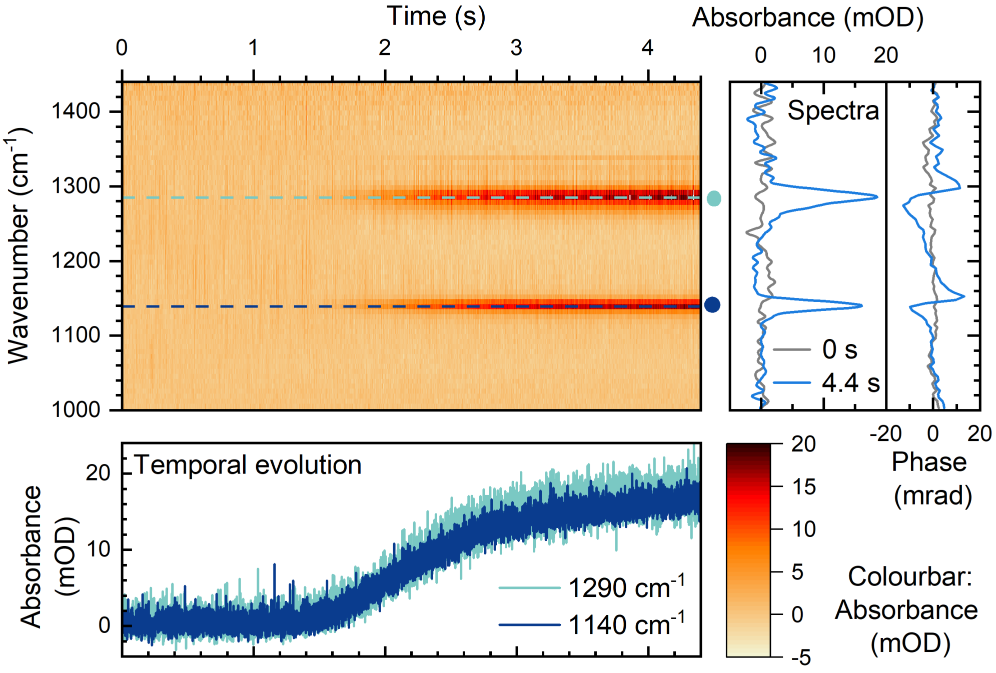

Figure 4.20: Spectral evolution of an injection process, where water is replaced by a 1-mg/ml aqueous solution of $DMSO_2$ (heatmap). The right panel shows the absorbance and spectral phase at the start- (0s) and end- (4.4 s) points of the injection event shown. In the bottom plot, the absorbance at two specific wavenumbers, i.e., 1140 and 1290cm^{-1} is plotted as a function of the laboratory time in dark blue and cyan respectively.

We depict the spectral dynamics of the injection in Fig 4.20 in the form of a 2-dimensional heatmap, with the x-axis corresponding to time, the y-axis, to wavenumber, and the colourbar, to absorbance in units of optical density. The plot shows 4.4 seconds of laboratory time, within which the injection is completed. The spectral amplitude and phase at the start (0 s) and end (4.4 s) are plotted on the panels to the right of the heatmap in grey and blue, respectively. The two absorption peaks at 1140 and 1290 cm^{-1}, corresponding to the symmetric and asymmetric stretching vibrations of the SO_2 group[24] are clearly visible, both in the absorbance and in the spectral phase. The temporal evolution at these two wavenumbers is plotted on the panel below the heatmap in dark blue and cyan. On considering the first 100 ms of time, i.e., well before the injection, the absorbance has a standard deviation of 0.8 and 1.1 mOD, respectively. The total absorption increases during the injection to settle at 16 mOD and 18 mOD.

4.5.3 Working with biological samples

As a first step towards biomedical application, we recorded EOS traces with human blood serum as the sample in the liquid cuvette. We then replaced the sample with distilled water, to take a reference measurement. The envelope of the EOS signals for the serum sample and the water reference are plotted in Fig. 4.21. Comparing the signal envelopes, one can see the resonant vibrational response of the serum sample that stays above that of the water reference, once the excitation pulse dies down. The field-sensitive nature of EOS enables the separation of the resonant vibrational response of samples, from the strong excitation.

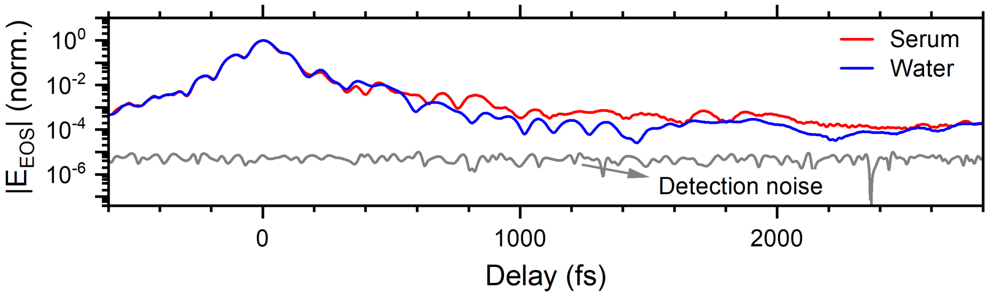

Figure 4.21: The envelope of the electric-field response of a sample of human blood serum is compared with that of water

The ability of the EOS-based dual-oscillator spectrometer to rapidly record the molecular fingerprints of coherently vibrating samples in the condensed phase across picosecond delay ranges with attosecond timing precision at kHz rates for a broad spectral range make it a viable candidate for new applications in infrared spectroscopy. Previous demonstrations of dual-oscillator[80] and dual-comb spectroscopy[51] with attosecond precision involved a constant repetition rate offset between two laser oscillators. In this case, the total delay range is determined by the pulse repetition frequency. The scanned delay range is on the order of nanoseconds for MHz repetition rates, often limiting their application to gas-phase spectroscopy. The new approach of EODT makes it possible to scan much smaller delay ranges, on the order of picoseconds, without comprising timing precision, opening up new avenues, for condensed-phase spectroscopy. The applicability of dual-oscillator scanning with EODT extends beyond field-resolved infrared spectroscopy, to other techniques such as pump-probe spectroscopy, and coherent anti-Stokes Raman spectroscopy. In the next chapter, this dual-oscillator spectrometer is employed for a case-control study, using infrared spectroscopy as a diagnostic tool for the detection of cancer.

Chapter 5

Application: Infrared phenotype diagnostics

In the previous chapter, I described the development of a novel rapid electric-field-resolved infrared spectrometer to analyze liquid samples. In this chapter, I will expand on the steps taken in translating the newly developed device towards clinical use. This was done through a case-control clinical study called *Lasers4Life* (German Clinical Trial Register: DRKS00019844, `www.lasers4life.de`) which aims at testing the effectiveness of field-resolved infrared spectroscopy in diagnosing common cancer phenotypes from infrared spectra of human blood plasma. The study involving more than 5300 participants was done in collaboration with medical specialists at the LMU University Hospital.

The study has four major sub-parts, corresponding to four common cancers: that of the lung, breast, bladder, and prostate. In each case, electric-field molecular fingerprints (EMFs) of venous blood plasma were acquired for a matched group of case and control subjects. A machine-learning model was used to develop a binary classifier to successfully distinguish between fingerprints obtained from cases and controls. The classifiers were then tested on newly acquired fingerprints to evaluate their accuracy. Kosmas V. Kepesidis performed the matching of the cases and controls, and the optimization of parameters for the binary classifier.

The performance of the field-resolved spectrometer was benchmarked against a commercial Fourier-Transform infrared spectrometer (MIRA Analyzer by CLADE GmbH). The following section shows the workflow for the study initiated in 2017.

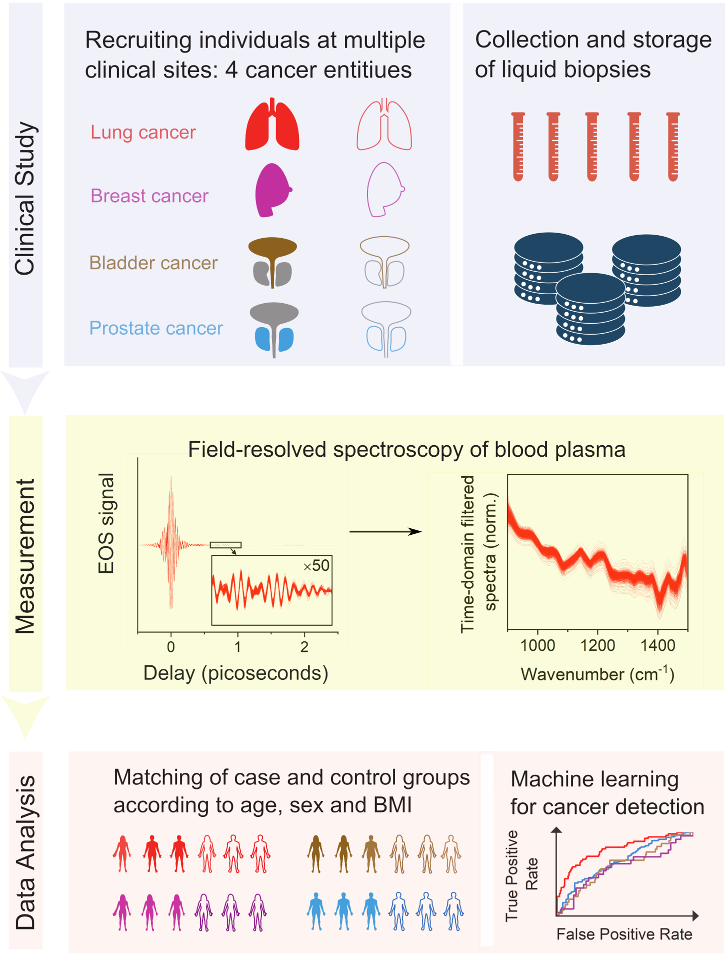

Figure 5.1: *Lasers4Life* workflow (adapted from Fig. 1 in Ref. [41]): Individuals were recruited in total, including lung, breast, bladder and prostate cancer phenotypes and non symptomatic references and individuals with a non-malignant pathology. Blood samples were collected, processed, transported, and stored according to standardized procedures. Infrared electric-field molecular fingerprints of the samples were captured by the technique of electro-optic sampling. For each phenotype, the case and control groups were matched for age, gender distribution, and body mass index before developing a machine-learning-based binary classifier for each of the cancer phenotypes

5.1 *Lasers4Life*: Workflow

Fig. 5.1 displays the workflow for the *Lasers4Life* clinical study. The steps are described below.

5.1.1 Sample collection, transport and storage

Human blood samples were collected in the different sites following the standardized procedure described in [41]. The blood samples were drawn into 7.5 plasma monovettes (Sarstedt) and placed in an upright position for at least 20 minutes before centrifugation at 2000g for 10 minutes, at a temperature of 20°. The supernatant was divided into 0.5 ml aliquots and placed in a -80°C freezer within 5 hours from the blood draw. Samples were transported to the location of the spectroscopic analysis, where they would be placed again in -80 °freezers. Transportation from the collection facility to the site of analysis was done under dry ice conditions.

5.1.2 Preparation for measurement

Prior to spectroscopic measurement, the 0.5 ml aliquots of blood plasma were thawed, centrifuged again at 2000g for 10 minutes, distributed into measurement tubes, such that each tube contained 100 µl of blood plasma. The measurement tubes were placed again in the - 80 °freezer, such that each sample hence passes through 2 freeze-thaw cycles between blood draw and spectroscopic measurement. The samples were measured in a randomized order and in a blinded fashion, i.e, with the measurement technician not knowing the phenotype corresponding to the a sample being measured. The spectroscopic measurements were performed in batches of 32, containing 25 blood plasma samples, 5 samples of quality control serum (pooled human serum, BioWest, Nuaillé, France), with one quality control serum being measured after 5 samples of blood plasma, and 2 samples of aqueous dimethyl sulfone with a concentration of 1 mg/ml, measured at the start and end of each batch. An automated sample delivery system (CLADE GmbH, Esslingen, Germany) with a 30 µm thick liquid cuvette with ZnSe windows was used.

5.1.3 Measurement and data management

The EOS-based spectroscopic measurement was performed using *InfraSampler 1.5*, which has a dual-oscillator setup that is capable of capturing 2,800 traces per second. When a measurement is started, the liquid cuvette is filled with water. A measurement control program that manages both the data acquisition and the sample delivery systems was developed in-house by colleagues Patrik Karandusovsky, Wolfgang Schweinberger, and Alexander Weigel.

Before measuring each sample, the liquid cuvette is cleaned and filled with de-ionized water. The acquisition of the EOS traces is started when the water is in the cuvette. The measurement control program triggers the injection of the following sample into the cuvette after 40 seconds of measurement. A 10- second window is considered to ensure complete injection of the sample, after which there is another 40 seconds of measurement. Each sample thus involves a total of 90 seconds of continuous acquisition, starting with water in the cuvette, capturing the injection until the cuvette is filled with the sample of interest. After the measurement of the sample, the cuvette is cleaned by an automated procedure, lasting close to 2 minutes, in preparation to measure the next sample.

The raw data acquired in a measurement involving the injection of a single sample, is recorded over a total of 70 seconds and takes up 28 GB of hard disk space. In the 2 minute interval between subsequent measurements, the sample is transferred from the measurement computer to a second computer where the data is processed, using a 5 Gigabit/s direct network connection. On a typical day, 3 batches, i.e., 96 measurements are done in a day, corresponding to 75 clinical study samples. The raw data is pre-processed to extract the delay axis, as mentioned in Section 4.4. The individual EOS traces, after delay extraction, shift correction and interpolation, are batch-averaged in sets of 128. This, and the removal of every alternate gate-laser shot where a mid-IR pulse is absent, reduces the size of a 90 second measurement to 150 MB. The raw data is archived, and the data which has been processed and averaged, is transferred to a server for storage and analysis.

The measurement of the samples occur in a randomized fashion, in order to avoid bias or systematic errors that may arise, for example, from acquiring all samples of a particular phenotype sequentially before the samples of another type. This improves reliability for training the binary classifier.

5.1.4 Standardization

Electro-optic sampling of the molecular response of few-cycle mid-infrared pulses enables the possibility to temporally separate the molecular response from the intense short-lived excitation. Efforts were taken in our research group, initiated by Marinus Huber [43, 42], to design a procedure to standardize electric-field resolved molecular fingerprints. Taking Fourier transforms of field-resolved fingerprints of the measured liquid samples, they were transferred to the spectral domain. These spectra were referenced with measurements taken with pure water in the liquid cell, and a time filter was applied to separate out the noise brought about by the impulsive excitation. The sequence of steps involved is breifly described below.

The EOS signal in the time domain, $S(t)$ is expressed as a convolution of the electric field, $E(t)$, with the instrument response function, $IRF(t)$.

$$S_{ref}(t) = E(t) \circledast IRF(t) \tag{5.1}$$

We model the change in the signal on introducing a sample by convolution with another term $H(t)$, such that the new signal is given by:

$$S_{sam}(t) = E(t) \circledast IRF(t) \circledast H(t). \tag{5.2}$$

$H(t)$ is referred to as the sample response in the time domain. On performing a Fourier transform, convolution corresponds to multiplication, giving us the relation:

$$FT(S_{sam}(t)) = FT(E(t) \circledast IRF(t) \circledast H(t)) = \tilde{E}(\omega) \cdot I\tilde{R}F(\omega)\tilde{H}(\omega). \tag{5.3}$$

In the absence of the sample, we have:

$$FT(S_{ref}(t)) = FT(E(t) \circledast IRF(t)) = \tilde{E}(\omega) \cdot I\tilde{R}F(\omega). \tag{5.4}$$

Now taking a ratio of spectra, with and without the sample in the beam path,

$$\frac{FT(S_{sam}(t))}{FT(S_{ref}(t))} = \frac{\tilde{E}(\omega) \cdot I\tilde{R}F(\omega)\tilde{H}(\omega)}{\tilde{E}(\omega) \cdot I\tilde{R}F(\omega)} = \tilde{H}(\omega), \tag{5.5}$$

we get the Fourier transform of the linear sample response in the frequency domain. To make the assumption of a linear, instrument independent sample response as close to reality as possible, we perform an additional step to minimize technical noise contributions. Since a major portion of the measured optical signal, and the associated noise is contained in the short and intense excitation pulse, we filter this portion out in the time domain, such that the obtained filtered sample response is devoid of this noise. The time-filtering is done by transforming $\tilde{H}(\omega)$ back to the time domain. After the time-filter is applied, it is transformed once again to the frequency domain, for compatibility with time-integrating approaches such as FTIR spectroscopy.

$$\tilde{H}(\omega) \xrightarrow{FT} H(t) \xrightarrow{time-domainfilter} H(t)w(t) \xrightarrow{FT} \tilde{H}_{filtered}(\omega) \tag{5.6}$$

The measurement of a sample involves 70 seconds of continuous acquisition, 30 seconds with water, a 10 second interval within which the sample is injected, and 30 seconds of sample measurement. Fig. 5.2(left) shows exemplary averaged EOS traces of a water reference (blue) and a blood plasma sample (red). The inset on the bottom right corner zooms into a section of the trace, clearly showing how the signal corresponding to water diminishes

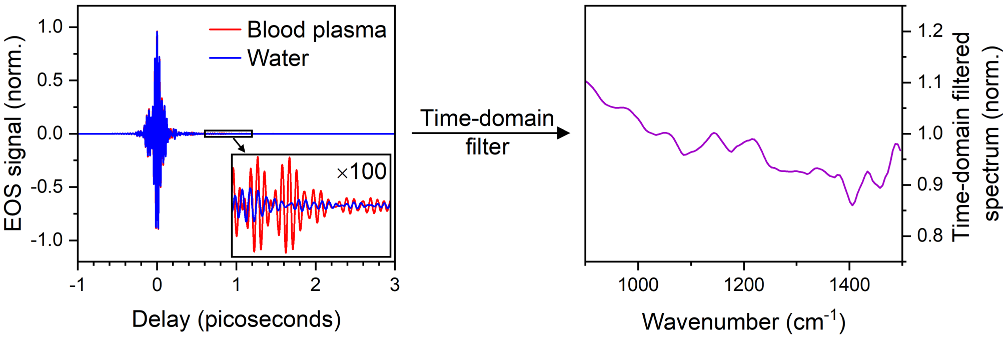

Figure 5.2: The left panel shows EOS traces measured with water (blue) and blood plasma (red) in the liquid cuvette. The inset zooms into the delay range between 0.6 ps and 1.2 ps, showing the resonant oscillations following the excitation. The time-domain filter was applied following the standardisation procedure to obtain the filtered spectrum shown on the right panel (purple). Time-domain filtered spectra were used for further analysis.

quicker than that of the plasma sample, which shows strong oscillations even at delays beyond 1 picosecond after the peak of the excitation. EOS traces are averaged over the entire 30 seconds and the time-domain filter is applied, to obtain a single averaged result with the response plotted as a function of wavenumber, depicted in the right panel of Fig. 5.2. The time-filtered spectrum is used for analysis and classification.

5.1.5 Analysis and classification

The sequence of steps described in the previous section show the journey of the spectroscopic data, from the moment it is recorded, capturing each individual laser pulse as a separate data point at 300 MB/s, followed by delay extraction, interpolation, averaging and standardization, to obtain the spectral response as a 100-kB spreadsheet. Now that the data is prepared, we set out to take a deep look, to answer biological questions, among which is the capacity to detect diseases such as cancer. We seek to use a linear machine learning classification model to identify systematic patterns that are characteristic to individuals that share a common phenotype. To do this with the highest efficiency, while at the same time ensuring that the patterns that are learnt do not arise from confounding variables. We perform careful statistical matching to ensure this.

When using machine learning algorithms for regression or classification, care needs to be taken that models that are developed do not describe solely

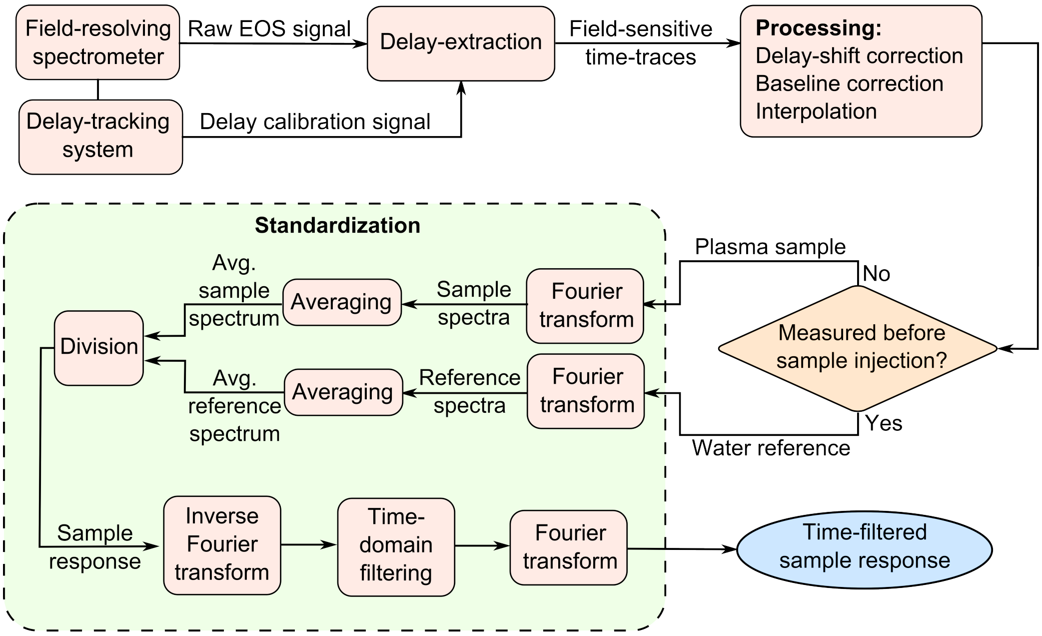

Figure 5.3: The flow diagram shows the various steps involved from measuring the molecular fingerprints using the field-sensitive spectrometer, to obtaining the time-filtered sample response which is the final outcome. The steps involve the extraction of delay axis and processing of the EOS traces as mentioned in 4.4, followed by standardization as described in 5.1.4

the original dataset, but are generally applicable to new data of the same time, that is, overfitting needs to be avoided. To do this, it is important to have a large enough dataset. The parameters of the classifier model need to be chosen wisely. Validation and testing on sets of data that are different from the one used for training reveal how widely these can be applied.

Matching of individuals enrolled in the clinical study In a case-control medical diagnostic study, the effect of confounding factors is one that is significant. Let us take the example of lung cancer. The average age of diagnosis is 70[86]. Thus, age is a confounding factor, with a higher age suggesting a higher risk of cancer being detected. Unless special care is taken, it is to be expected that the cases have a higher mean age than the control participants. The machine learning model trained to detect cancer may also attribute age-related patterns to the model to diagnose cancer. This can be circumvented by matching the age of the cases and controls such that the mean and standard deviation is as close as possible to each other for the cases and controls. A similar effect could stem from factors such as gender and body mass index.

Case and control sample groups were matched considering the three observables of age, sex, body mass index (BMI), and number of participants, for all training sets (described below). A subset of samples is excluded from the case set, as well as the control set, to match the mean and standard deviation to as much an extent as reasonably feasible. Examples are shown in the Results section 5.2.1.

Training and testing the classifier model For the different cases studied, involving different types of cancer, the samples were split into training and test sets. Around 20 percent of the samples were set aside to form an independent test set to evaluate the performance of the classifier. The remaining set of matched clinical samples were labelled as the training set, to develop the binary classifier model.

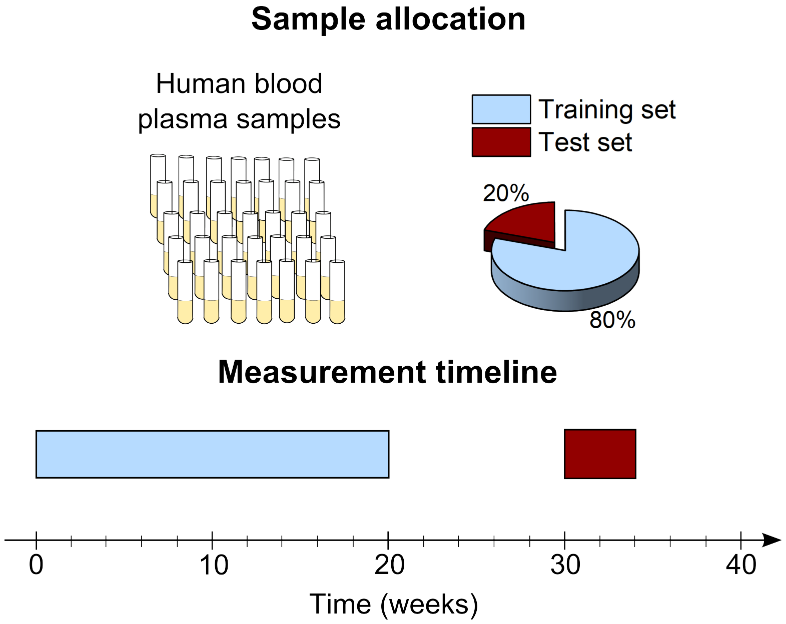

Figure 5.4: Splitting of the entire set of blood plasma samples into a training set and a test set (top), and the timeline for performing the measurements of the training and test sets (bottom).

Samples from the training set were measured first, in a randomized fashion. Training of the binary classification models based on a linear support vector machine was performed using the scikit-learn [69] open-source machine learning package in Python, and was implemented by Kosmas V. Kepesidis. The accuracy of the training process is first estimated by means of a 5-fold cross-validation performed on measurements of samples in the training set. In order to evaluate the final performance of the classifier model in an unbiased manner, the test set is locked away during the whole process of training and optimizing the model [78].

For the developed instrument and the whole approach to be deemed useful, it is important to also evaluate the robustness of the classifier model subject to slowly accumulating physical changes in the measurement system. A necessary condition is that a trained classifier model should be able to effectively classify measurements performed in the future, and that it is not limited to a time-frame of a single campaign covering a few weeks. To do this, a 10-week time-gap was introduced between measurements of the training set and the test set. Fig. 5.4 shows the distribution of samples into the training and test sets, and the timeline for performing the measurements.

5.2 *Lasers4Life*: Results

5.2.1 Distribution of samples in the training and test sets

From the >5,300 samples that were successfully measured, a subset of around 3̃200 samples was selected to constitute matched case and control groups for four common cancers: lung cancer, prostate cancer, breast cancer, and bladder cancer. The distribution of phenotypes for the overall training set is shown in Table 5.1. In addition to the four cancer phenotypes and non-symptomatic references, samples of individuals with benign prostatic hyperplasia (BPH) and benign disease were measured as well.

Phenotype	# Samples
Non-symptomatic	571
Prostate cancer	600
Benign prostatic hyperplasia	554
Lung cancer	419
Benign disease	321
Bladder cancer	166
Breast cancer	137
Total	**2768**

Table 5.1: *Lasers4Life* training set

The groups of non-symptomatic reference individuals and individuals with one of the four types of cancer are expected to be the easiest to classify. Classifying these two phenotypes should indeed be the first step in developing a new diagnostic test, but is however not a sufficient condition. A meaningful diagnostic test must also be able to differentiate between individuals with another disease of the same organ, or any physiology that is not malignant, and a case of the particular cancer phenotype of interest. This was the motive behind the inclusion of samples of individuals with BPH and benign disease. In this thesis, which describes the study's first phase, these samples have been excluded, thus utilizing only those samples from non-symptomatic individuals and individuals with cancer. The distribution of samples in the test set is shown in Table 5.2.

Phenotype	# Samples
Non-symptomatic	181
Prostate cancer	132
Lung Cancer	56
Bladder cancer	30
Breast cancer	24
Total	**423**

Table 5.2: *Lasers4Life* test set

Case and control groups were matched according to age, sex, and BMI to create the training set for each of the 4 cases. Our matching procedure is described in Table 5.3, taking the example of bladder cancer. Out of all non-symptomatic control samples (>500), 166 were chosen so as to best match the observable parameters. The mean and standard deviation of the age, sex (represented as 0 and 1), and BMI are shown, before and after matching.

Observables	Cases	Unmatched controls	Matched controls
Age	71.99 ± 10.36	50.85 ± 16.23	71.07 ± 9.44
Sex	0.21 ± 0.41	0.65 ± 0.48	0.19 ± 0.40
BMI	25.86 ± 4.29	25.31 ± 5.06	26.28 ± 3.97

Table 5.3: Matching case and control groups of individuals for bladder cancer

5.2.2 Infrared fingerprint-based cancer classification

The performance of the developed binary classifiers in correctly categorizing the EMFs of samples of human blood plasma was tested for four common cancer types, lung cancer, prostate cancer, bladder cancer and breast cancer. The outcome is expressed in terms of the area under the receiver operating characteristic (ROC) curve, as discussed in section 2.5.4. Fig. 5.5 shows the

ROC curves for each of the 4 cancer phenotypes measured using the field-resolved spectrometer described in the thesis, for both the training and test sets.

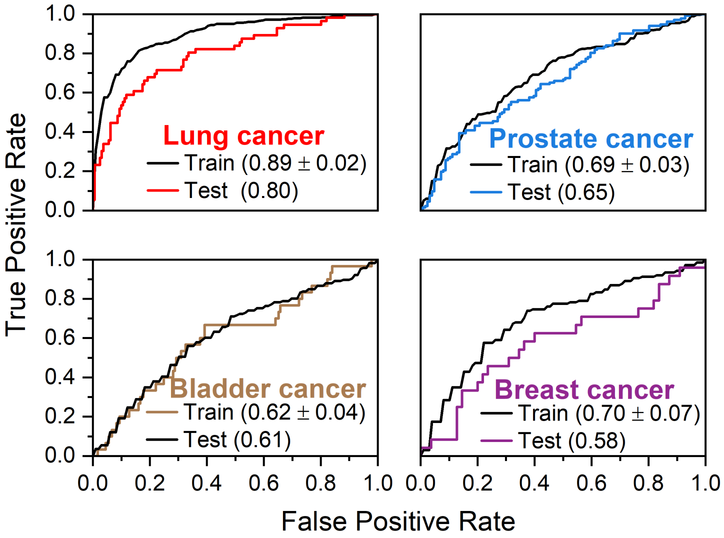

Figure 5.5: ROC curves for the classification of 4 cancer phenotypes from non-symptomatic references are shown for measurements performed using the developed field-resolved spectrometer for lung cancer, prostate cancer, bladder cancer and breast cancer. The ROC for the training sets, obtained by performing a 5-fold cross validation, are plotted in black. The ROC for the independent set, samples of which were measured after a 10-week chronological gap, are plotted in red, blue, light brown, and purple, respectively. The area under the curve is specified in each case.

The ROC for the training sets are obtained by a 5-fold cross validation. This involves dividing the training dataset into 5. The model classifier is trained using data from 4 out of 5 parts, and the classification accuracy is evaluated on the remaining subset of the training set. This is repeated 5 times by cycling the subset that is used for evaluation. This leads to 5 ROC curves, plotted as solid black lines in Fig. 5.5. The mean and standard deviation of the area under the ROC curve are mentioned for each case.

For the case of lung cancer versus non-symptomatic references using FRS, the area under the ROC curve is 0.89 for the training set, with a standard deviation of 0.02 on performing the 5-fold cross validation. For the case of the test set measured after a chronological gap of 10 weeks, the area under the curve (AUC) reduces to 0.80, implying an 80 percent chance of a sample being correctly classified into case or control. We attribute this decrease mainly to the changes accumulated in the measuring apparatus over the gap period decrease the effectiveness of the learnt classifier in its performance. Other factors such as biological randomness, as well as the lower number of samples in the test set could lead to differences in the obtained AUC values.

This lung cancer detection capability is promising. A previously reported lung cancer screening approach involving a collection of four serum-based markers [9] boasted of an AUC of 0.83, among syptomatic individuals. The individual markers, however resulted in lower AUCs ranging from 0.69 to 0.76. Infrared fingerprints provide the advantage of providing a fairly high classification accuracy with just a single test. The low-dose CT technique in the National Lung Screening Trial in the United States of America showcased an AUC of 0.93 [73].

For the classification of prostate cancer cases from non-symptomatic references, the same general behaviour can be seen, though with a lower values of the AUC: 0.69 ± 0.03 and 0.65 for the training and test sets, respectively. In the first phase of the study, as described in this thesis, analysis was limited to prostate cancer cases and non-symptomatic controls, excluding samples from individuals with a benign pathology. As prostate cancer grows slowly, with typical tumour doubling times of two years or more [82], in comparison to the exponential growth at the early stages of lung cancer [35] with doubling times of 5-6 months [4], it is not surprising that the EMFs classify prostate cancer cases from controls less accurately than for lung cancer. The ROC curves for the case of bladder cancer show areas that are smaller in comparison to the previous cases of lung cancer and prostate cancer, with a test set AUC of 0.61. For the case of breast cancer, the AUC obtained for the test set was 0.58. The classification accuracy for bladder cancer and breast cancer are close to pure chance, and do not look promising at the moment. This needs to be further investigated, as the search continues for robust blood-based biomarkers for the detection of bladder cancer [59, 54], and breast cancer [58].

5.2.3 Stability of infrared fingerprints

The reproducible functioning of the entire molecular fingerprinting apparatus is a prerequisite for any practical applications to probe materials. Contributors to noise and errors in measurement are manyfold. Technical variability associated with the fingerprinting process is based on multiple factors: Fluctuations in the laser source, the mid-infrared generation, the injection of the sample fluid into the liquid cuvette, detection by electro-optic sampling, and the cleaning of the liquid cuvette in between samples. These are however, not the only source of variation. Biological variabilty is defined by variations in the spectral features of samples of blood plasma from person to person. This interpersonal biological variability has been found to be higher than the technical variability for infrared spectroscopy [40] as well as mass spectroscopy [15].

Before tackling the medical problem of biological variability in the properties of biofluid samples across individuals, we sought to estimate the technical variability of the newly developed field-resolved fingerprinting approach across different timescales, such as days, weeks and months. Over the course of the entire measurement campaign, a practice of measuring samples of commercially available quality control(QC) serum (pooled human serum, BioWest, Nuaillé, France) repeatedly at regular intervals was adopted. All QC serum samples are nominally identical. Thus, there is no biological variability across these samples, and variations in their fingerprints are attributed to technical variability, and possible variations in sample handling. In practice, one sample of QC serum was measured after measuring five plasma samples from the study cohort.

The top panel Fig. 5.6 shows the averaged time-filtered spectra of quality control serum (black), and of all study plasma samples (red), along with the standard deviation (shaded region) over the entire training data set which was acquired over a timespan of 10 weeks. The filtered spectra were normalized to the peak at 1143 cm^{-1}. The bottom panel displays the wavenumber-averaged standard deviation for all QC serum and study plasma measurements over timescales of a day, week, month, and the entire training and test sets, lasting 20 and 2 weeks respectively.

The standard deviation of QC serum samples represents the stability of the molecular fingerprinting process, as a measure of how reproducible the measuring apparatus along with technical workflow of sample handling is, in its ability to capture the molecular fingerprint of nominally identical samples.The standard deviation in the study plasma samples encompasses, in addition, the biological variability in the makeup of blood plasma across individuals, across different phenotypes, as well as differences in the acquisition and processing of samples in the multi-centric study. The standard deviation of the study samples surpasses the fingerprinting reproducibilty indicated by standard deviation of the QC serum samples by 110 %, 90 %, and 70 % over the timescale of a day, week and month respectively. In each case, e.g, the timescale of a day, the standard deviation of all measurements acquired in each day was calculated, following which I took the mean across all days. Both the QC serum and study plasma samples show a rising trend with the length of the timescale involved. The standard deviation of all measurements across the training and test sets is also shown.

Outliers, with spectral components that deviated from the mean by

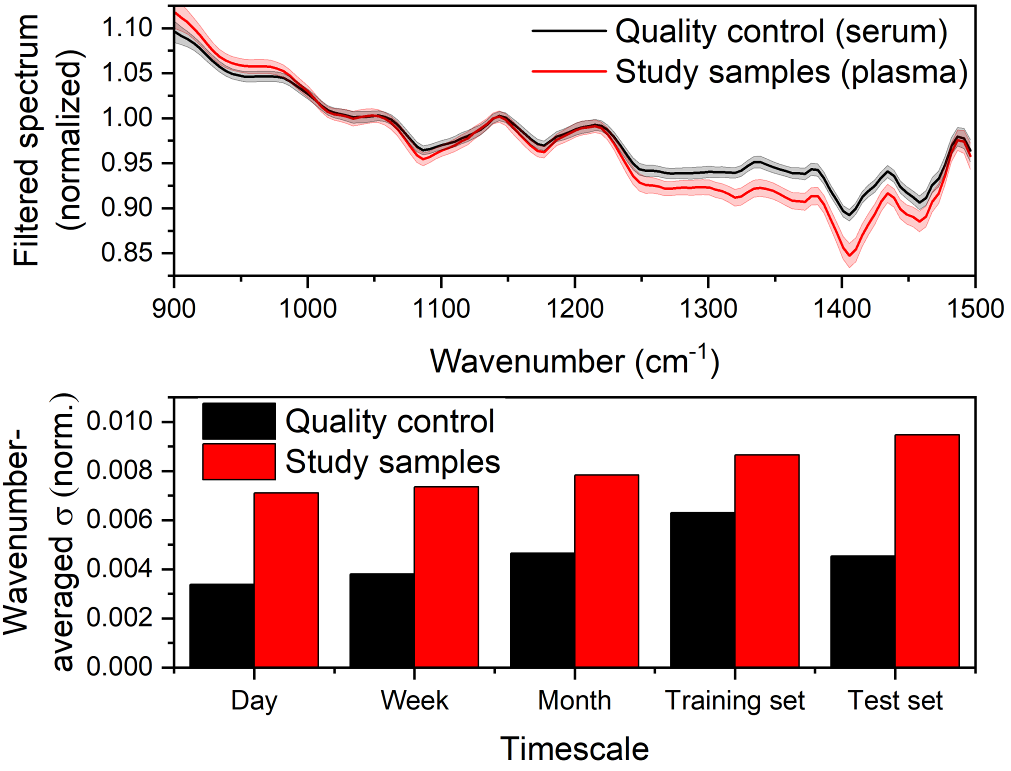

Figure 5.6: (Top) Time-domain filtered sample response for quality control serum (black), and blood plasma study samples(red), averaged over all measurements acquired across 10 weeks. This corresponds to the entire training set of the first phase of the *Lasers4Life* campaign. The shaded area around each line represents the standard deviation over the entire training set. (Bottom) Wavenumber-averaged standard deviation in the time-domain-filtered spectra of quality control serum (black) and study plasma samples (red) over different timescales from within a day to the entire training and test data sets.

3 times the standard deviation were excluded from the stability analysis. Wrong labeling of samples and improper injection into the liquid cuvette are considered to be the main cause for these outliers, which amount to 2 percent of the measured samples.

The fact that the standard deviation for the QC serum samples are clearly lower than that for the study samples confirms the fact that the sensitivity of our fingerprinting is higher than the level of biological noise involved in such a blood plasma based case-control study. The training set, which was acquired over 20 weeks, however, shows a significant increase in the standard deviation for the QC serum samples, with the value for the study plasma samples being only 40 % higher. We attribute this increase in variation to changes made in the optical setup of the spectrometer for maintenance and upkeep, within the 20-week time-frame of measuring the samples in the training set. This needs to be further investigated, and reveals scope for improvement for the instruments to be developed in the future.

5.2.4 Capacity of spectroscopic fingerprinting to detect cancer

In order to benchmark the performance of the newly developed field-resolved spectrometer, an identical measurement campaign with all the > 5300 samples was undertaken, with a commercial Fourier-transform infrared (FTIR) spectrometer (MIRA Analzer, CLADE GmbH). An identical sample delivery system with a robotic arm, as in the MIRA analyzer, was used with the field-resolved spectrometer. The measurements were performed in the same 'randomized' order, with a gap between the training and test sets.

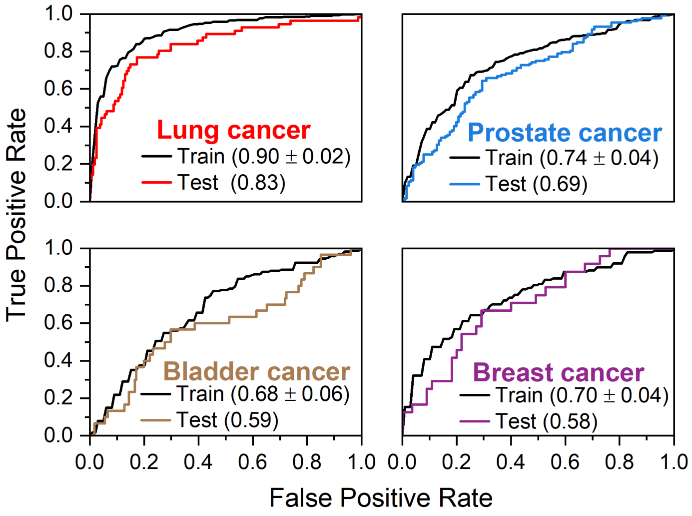

Figure 5.7: The ROC curves corresponding to classifying the infrared fingerprints of blood plasma samples from individuals with lung cancer, prostate cancer, bladder cancer, and breast cancer from that of non-symptomatic reference individuals, acquired using a commercial Fourier-transform infrared spectrometer. The solid black lines represent ROC curves for the training sets, while the coloured lines represent the test.

Fig. 5.7 shows the ROC curves for the measurements taken with the FTIR spectrometer. The AUC values are comparable to those obtained with the field-resolved spectrometer, as shown in Fig. 5.5, with marginally higher values obtained with the FTIR. That this newly developed spectrometer matches the performance of the state-of-the art commercial FTIR spectrometer sends an encouraging message to pursue further development of the technique.

Overall, we were able to test the newly developed field-resolved spectrometer in a clinical study involving thousands of individuals, to detect common cancer phenotypes. The results of the binary classification between individuals with a cancer phenotype and non-symptomatic controls showed promising results, especially for the cases of lung and prostate cancer, reinforcing the efficacy of infrared molecular fingerprinting in identifying these phenotypes in a minimally invasive manner, from blood plasma. While the FTIR spectrometer and the field-resolving spectrometer are completely different instruments, the fact that the classification accuracy of both approaches are similar can be seen as a supporting argument for the robustness of infrared molecular fingerprinting. While the current device is on par with FTIR, improved versions with a broader bandwidth in the shorter wavelength range of the molecular fingerprinting region [46, 87] combined with higher stability [50] sensitivity and better engineering are expected to go far beyond.

Chapter 6

Conclusions and Outlook

This thesis described the development path of a rapid field-resolving infrared spectrometer for probing human blood plasma samples, exploring its potential as a single-measurement medical diagnostic tool. The device measured the waveforms of mid-infrared pulses transmitted through a cuvette filled with a liquid sample of interest by rapid electro-optic sampling. Demonstrating two approaches to perform this, sensitive measurement of mid-infrared waveforms across picosecond delay ranges with attosecond timing precision was performed, enabling condensed-phase spectroscopy with high throughput and suppressed technical noise.

Chapter 3 described a first attempt at rapid scanning using a sonotrode, which is a sonification device vibrating at an ultrasonic frequency, as an optical delay line. A part of the few-cycle near-IR pulses that drove mid-IR generation was split off at an earlier stage to serve as the gate for electro-optic sampling [77]. Equipped with interferometric delay tracking to precisely track relative delay fluctuations of the gate and mid-IR beam paths, we achieved sensitive detection of mid-IR waveforms at 38,000 scans per second for a total delay range of 1.6 ps with 34-attosecond timing precision. Here, the delay range for the scan and the scanning rate were determined by the dimensions and mechanical properties of the sonotrode.

Chapter 4 showcased a dual-oscillator setup with electronically modulated repetition frequencies for field-resolved spectroscopy with rapid-delay scanning. Here, the gate for electro-optic sampling was sourced from a second laser oscillator. The repetition frequency of this laser was carefully controlled with respect to that of the first laser which generated the infrared, by means of an active feedback loop. In a previously demonstrated dual-oscillator spectrometer with sub-femtosecond timing precision approach for electro-optic sampling[51], a constant offset was maintained between the two repetition frequencies of the two lasers. In such a scenario, the scanned delay range equals the reciprocal of the pulse repetition frequency. For a 100 MHz repetition frequency, this corresponds to 10 nanoseconds.

Using the novel technique of electro-optic delay tracking, combined with the electronic modulation of the repetition frequency, we demonstrated scanning over picosecond delays suited to condensed-phase spectroscopy with attosecond-level timing precision. By limiting the scanned delay range, waveforms could be captured at kHz rates, thus opening a door for field-resolved spectroscopy to applications such as label-free flow cytometry [30, 36], monitoring reaction kinetics[56, 72, 48] and protein conformational changes[89]. Rapid scanning also allowed suppressing technical noise contributions and fluctuations at sub-kHz frequencies by freezing their effect within a scan.

Finally, Chapter 5 described using the field-resolving spectrometer in a large-scale case-control clinical study to identify individuals with one of four common cancers from field-resolved infrared molecular fingerprints of their blood plasma. The newly developed system displayed robust functioning over more than half a year, which was the time required to complete the first phase of measurements in the *Lasers4Life* study involving sample investigation over 5300 human individuals. With the help of machine-learning-based pattern recognition, individuals with lung cancer and non-symptomatic control individuals could be classified with 80 % accuracy. The results were not as promising for the other types of cancers studied, namely prostate cancer, breast cancer, and bladder cancer. We obtained comparable results for both techniques by measuring identical samples with a state-of-the-art commercial FTIR spectrometer. We consider this as supporting the diagnostic capacity of infrared molecular fingerprints, seeing how completely different techniques within infrared spectroscopy lead to the same result.

While FTIR spectroscopy has been a well-established technique for several decades, we believe that field-resolved spectroscopy is at an early stage with great potential for development in the future. Efforts have been underway in extending the bandwidth [46, 87], stability[50], and sensitivity. On other fronts, studies in the recent past have helped better understand the dynamics of coherent energy transfer between broadband infrared light and molecular vibration states [70], the relationship between the structure of a protein and its infrared fingerprints[97], as well as the link between infrared fingerprints and disease-induced molecular changes in the blood [94]. Potential biomedical applications of infrared spectroscopy of biofluids are not limited to cancer detection. With first demonstrations that an individual's blood-based infrared molecular fingerprint is stable over timescales of several months [40], the technique could benefit the emerging field of personalized medicine. The application of infrared spectroscopy imaging in investigating the chemical makeup of biological tissues in histopathology is also being pursued intensely [8]. With great potential on many fronts [25], infrared molecular fingerprinting is at a crucial development phase in its journey toward real-world application in medical facilities. As researchers across locations and disciplines focus on the right questions and the best approaches to push forward this goal [25], I believe it is only a matter of time till this great potential breaks through to benefit mankind.

Appendix A

Data Archiving

All data presented in this thesis, all figures and program code used to generate them are stored on the data archive server of the Laboratory of Attosecond Physics at the Max Planck Institute of Quantum Optics.

Bibliography

[1] C.K. Akhgar, G. Ramer, M. Żbik, A. Trajnerowicz, J. Pawluczyk, A. Schwaighofer und B. Lendl, *Analytical Chemistry* **92** (2020), 9901.

[2] D. Allan, *Proceedings of the IEEE* **54** (1966), 221.

[3] T. Amotchkina, M. Trubetskov, A. Weigel, D. Hahner, S.A. Hussain, P. Jacob, I. Pupeza und V. Pervak: In *2021 Conference on Lasers and Electro-Optics Europe and European Quantum Electronics Conference*OSA Technical Digest. Optica Publishing Group (2021) Page ce 6 2.

[4] T. Arai, T. Kuroishi, Y. Saito, Y. Kurita, T. Naruke und M. Kaneko, *Jpn J Clin Oncol* **24** (1994), 199.

[5] J. Backhaus, R. Mueller, N. Formanski, N. Szlama, H.G. Meerpohl, M. Eidt und P. Bugert, *Vibrational Spectroscopy* **52** (2010), 173.

[6] M.J. Baker, S.R. Hussain, L. Lovergne, V. Untereiner, C. Hughes, R.A. Lukaszewski, G. Thiéfin und G.D. Sockalingum, *Chemical Society Reviews* **45** (2016), 1803.

[7] M. Beck: *Quantum Mechanics : Theory and Experiment.* Oxford University Press, Incorporated, New York, UNITED STATES, 2012.

[8] R. Bhargava, *Annual Review of Analytical Chemistry* **16** (2023), 205.

[9] S. Blanco-Prieto, L. De Chiara, M. Rodríguez-Girondo, L. Vázquez-Iglesias, F.J. Rodríguez-Berrocal, A. Fernández-Villar, M.I. Botana-Rial und M.P. de la Cadena, *Scientific Reports* **7** (2017), 41151.

[10] R.W. Boyd: *Nonlinear Optics, Third Edition.* 3. Auflage. Academic Press, Inc., USA, 2008.

[11] J. Braithwaite, *BMJ* **361** (2018), k2014.

[12] D. Brida, G. Krauss, A. Sell und A. Leitenstorfer, *Laser & Photonics Reviews* **8** (2014), 409.

[13] T. Buberl: *Towards next-generation molecular fingerprinting.* Ludwig-Maximilians-Universität München, Dissertation, March 2021.

[14] G. Cerullo, A. Baltuška, O. Mücke und C. Vozzi, *Laser & Photonics Reviews* **5** (2011), 323.

[15] B. Crews, G.J. Wikoff Wr Fau Patti, H.K. Patti Gj Fau Woo, E. Woo Hk Fau Kalisiak, J. Kalisiak E Fau Heideker, G. Heideker J Fau Siuzdak und G. Siuzdak, *Analytical Chemistry* (2009).

[16] N. Cristianini und J. Shawe-Taylor: *An Introduction to Support Vector Machines and Other Kernel-based Learning Methods.* Cambridge University Press, 2000.

[17] A. Darrudi, M.H. Ketabchi Khoonsari und M. Tajvar, *Journal of Preventive Medicine & Public Health* (2022).

[18] T. Davenport und R. Kalakota, *Future Healthcare Journal* (2019).

[19] T. Ditmire, *American Scientist* **98** (2010), 394.

[20] P.A. Elzinga, R.J. Kneisler, F.E. Lytle, Y. Jiang, G.B. King und N.M. Laurendeau, *Appl. Opt.* **26** (1987), 4303.

[21] P.A. Elzinga, F.E. Lytle, Y. Jian, G.B. King und N.M. Laurendeau, *Applied Spectroscopy* **41** (1987), 2.

[22] M. Evans. In *Vectors, Tensors and Fields.* Edinburgh (2002), .

[23] J. Faist, F. Capasso, D.L. Sivco, C. Sirtori, A.L. Hutchinson und A.Y. Cho, *Science* **264** (1994), 553.

[24] W.R. Feairheller und J.E. Katon, *Spectrochimica Acta* **20** (1964), 1099.

[25] D. Finlayson, C. Rinaldi und M.J. Baker, *Analytical Chemistry* **91** (2019), 12117.

[26] P.A. Franken, A.E. Hill, C.W. Peters und G. Weinreich, *Phys. Rev. Lett.* **7** (1961), 118.

[27] D. Freude. *Lecture notes in Spectroscopy for Physicists*, June 2006. Universität Leipzig.

[28] K. Fritsch, M. Poetzlberger, V. Pervak, J. Brons und O. Pronin, *Optics Letters* **43** (2018), 4643.

[29] A.B. Garrett, *Journal of Chemical Education* **39** (1962), 534.

[30] D. Gerz, M. Huber, H. Mirkes, F. Lindinger, Y. Münzenmaier, A. Weigel, M. Kielpinski, T. Henkel, M. Zigman, F. Krausz, J. Popp und I. Pupeza: In *Conference on Lasers and Electro-Optics/Europe (CLEO/Europe 2023) and European Quantum Electronics Conference (EQEC 2023)*Technical Digest Series. Optica Publishing Group (2023) Page cl_2_1.

[31] R. Ghorbani und F.M. Schmidt, *Applied Physics B* **123** (2017), 144.

[32] L.H. Goetz und N.J. Schork, *Fertility and Sterility* (2018).

[33] P.R. Griffiths, *Science* **222** (1983), 297.

[34] J.A. Hanley und B.J. McNeil, *Radiology* **143** (1982), 29.

[35] M.A. Heuvelmans, R. Vliegenthart, H.J. de Koning, H.J. Groen, M.J. van Putten, U. Yousaf-Khan, C. Weenink, K. Nackaerts, P.A. de Jong und M. Oudkerk, *Lung Cancer* **108** (2017), 48.

[36] K. Hiramatsu, T. Ideguchi, Y. Yonamine, S. Lee, Y. Luo, K. Hashimoto, T. Ito, M. Hase, J.W. Park, Y. Kasai, S. Sakuma, T. Hayakawa, F. Arai, Y. Hoshino und K. Goda, *Science Advances* **5** Page eaau0241.

[37] C. Hofer. *Theoretical Background.* Springer International Publishing, Cham, 2022. Pages 9–32.

[38] M. Huber: *Field-resolved infrared spectroscopy.* Ludwig-Maximilians-Universität München, Dissertation, November 2020.

[39] M. Huber, K.V. Kepesidis, L. Voronina, M. Božić, M. Trubetskov, N. Harbeck, F. Krausz und M. Žigman, *Nature Communications* **12** (2021), 1511.

[40] M. Huber, K.V. Kepesidis, L. Voronina, M. Božić, M. Trubetskov, N. Harbeck, F. Krausz und M. Žigman, *Nature Communications* **12** (2021), 1511.

[41] M. Huber, K.V. Kepesidis, L. Voronina, F. Fleischmann, E. Fill, J. Hermann, I. Koch, K. Milger-Kneidinger, T. Kolben, G.B. Schulz, F. Jokisch, J. Behr, N. Harbeck, M. Reiser, C. Stief, F. Krausz und M. Zigman, *eLife* **10** (2021), e68758.

[42] M. Huber, M. Trubetskov, W. Schweinberger, P. Jacob, M. Zigman, F. Krausz und I. Pupeza: In *2023 Conference on Lasers and Electro-Optics Europe and European Quantum Electronics Conference*, Volume ch_13_1. (2023).

[43] M. Huber, M. Trubetskov, W. Schweinberger, P. Jacob, M. Zigman, F. Krausz und I. Pupeza. *Standardised electric-field-resolved molecular fingerprinting*, in review.

[44] R. Huber, A. Brodschelm, F. Tauser und A. Leitenstorfer, *Applied Physics Letters* **76** (2000), 3191.

[45] S.A. Hussain, W. Schweinberger, T. Buberl, C. Hofer und I. Pupeza: In *2019 Conference on Lasers and Electro-Optics Europe and European Quantum Electronics Conference*, Volume ed_6_2. Optica Publishing Group (2019).

[46] H. Kassab, S. Gröbmeyer, W. Schweinberger, C. Hofer, P. Steinleitner, M. Högner, T. Amotchkina, D. Gerz, M. Knorr, R. Huber, N. Karpowicz und I. Pupeza, *Opt. Express* **31** (2023), 24862.

[47] P.L. Kelley, *Phys. Rev. Lett.* **15** (1965), 1005.

[48] J.L. Klocke, M. Mangold, P. Allmendinger, A. Hugi, M. Geiser, P. Jouy, J. Faist und T. Kottke, *Analytical Chemistry* **90** (2018), 10494.

[49] R.J. Kneisler, F.E. Lytle, G.J. Fiechtner, Y. Jiang, G.B. King und N.M. Laurendeau, *Opt. Lett.* **14** (1989), 260.

[50] M. Kowalczyk, N. Nagl, P. Steinleitner, N. Karpowicz, V. Pervak, A. Głuszek, A. Hudzikowski, F. Krausz, K.F. Mak und A. Weigel, *Optica* **10** (2023), 801.

[51] A.S. Kowligy, H. Timmers, A.J. Lind, U. Elu, F.C. Cruz, P.G. Schunemann, J. Biegert und S.A. Diddams, *Science Advances* **5** (2019), eaaw8794.

[52] A. Lambrecht, M. Pfeifer, W. Konz, J. Herbst und F. Axtmann, *Analyst* **139** (2014), 2070.

[53] P.D. Lewis, K.E. Lewis, R. Ghosal, S. Bayliss, A.J. Lloyd, J. Wills, R. Godfrey, P. Kloer und L.A.J. Mur, *BMC Cancer* **10** (2010), 640.

[54] S. Li, K. Xin, S. Pan, Y. Wang, J. Zheng, Z. Li, X. Liu, B. Liu, Z. Xu und X. Chen, *Cellular & Molecular Biology Letters* **28** (2023), 28.

[55] K.M.G. Lima, K.B. Gajjar, P.L. Martin-Hirsch und F.L. Martin, *Biotechnology Progress* **31** (2015), 832.

[56] E. Lins, S. Read, B. Unni, S.M. Rosendahl und I.J. Burgess, *Analytical Chemistry* **92** (2020), 6241.

[57] X. Liu, R.M. Osgood, Y.A. Vlasov und W.M.J. Green, *Nature Photonics* **4** (2010), 557.

[58] S.Y. Loke und A.S.G. Lee, *European Journal of Cancer* **92** (2018), 54.

[59] R. López-Cortés, B.B. Gómez, S. Vázquez-Estévez, D. Pérez-Fentes und C. Núñez, *J Proteomics* **247** (2021), 104329.

[60] T.H. Maiman, *Nature* **187** (1960), 493.

[61] K.S. Maiti, E. Fill, F. Strittmatter, Y. Volz, R. Sroka und A. Apolonski, *Scientific Reports* **11** (2021), 18381.

[62] I. Newton, *Philosophical Transactions of the Royal Society of London* **6** (1672), 3075.

[63] M. Paraskevaidi, C.L.M. Morais, K.M.G. Lima, K.M. Ashton, H.F. Stringfellow, P.L. Martin-Hirsch und F.L. Martin, *Analyst* **143** (2018), 3156.

[64] F. Paries, O. Boidol, G. von Freymann und D. Molter, *Optics Express* **31** (2023), 6027.

[65] W.W. Parson und C. Burda. *Vibrational Absorption.* Springer International Publishing, Cham, 2023. Pages 331–375.

[66] R. Paschotta. *Self-focusing.* RP Photonics Encyclopedia, May 2007.

[67] R. Paschotta. *Self-phase Modulation.* RP Photonics Encyclopedia, Jun 2007.

[68] T.H. Pearson und A.J. Ihde, *Journal of Chemical Education* **28** (1951), 267.

[69] F. Pedregosa, G. Varoquaux, A. Gramfort, V. Michel, B. Thirion, O. Grisel, M. Blondel, P. Prettenhofer, R. Weiss, V. Dubourg, J. Vanderplas, A. Passos, D. Cournapeau, M. Brucher, M. Perrot und E. Duchesnay, *Journal of Machine Learning Research* (2011).

[70] M.T. Peschel, M. Högner, T. Buberl, D. Keefer, R. de Vivie-Riedle und I. Pupeza, *Nature Communications* **13** (2022), 5897.

[71] M.C. Phillips, M.S. Taubman, B.E. Bernacki, B.D. Cannon, R.D. Stahl, J.T. Schiffern und T.L. Myers, *Analyst* **139** (2014), 2047.

[72] N.H. Pinkowski, Y. Ding, C.L. Strand, R.K. Hanson, R. Horvath und M. Geiser, *Measurement Science and Technology* **31** (2020), 055501.

[73] P.F. Pinsky, D.S. Gierada, H. Nath, E.A. Kazerooni und J. Amorosa, *Journal of Medical Screening* **20** (2013), 165.

[74] M. Porer, J.M. Ménard und R. Huber, *Optics Letters* **39** (2014), 2435.

[75] I. Pupeza, M. Huber, W. Schweinberger, M. Trubetskov, S.A. Hussain, L. Vamos, O. Pronin, F. Habel, V. Pervak, N. Karpowicz, E. Fill, A. Apolonski, M. Zigman, A.M. Azzeer und F. Krausz: In *2017 European Conference on Lasers and Electro-Optics and European Quantum Electronics Conference*. Optica Publishing Group (2017) Page CH_2_4.

[76] I. Pupeza, M. Huber, M. Trubetskov, W. Schweinberger, S.A. Hussain, C. Hofer, K. Fritsch, M. Poetzlberger, L. Vamos, E. Fill, T. Amotchkina, K.V. Kepesidis, A. Apolonski, N. Karpowicz, V. Pervak, O. Pronin, F. Fleischmann, A. Azzeer, M. Žigman und F. Krausz, *Nature* **577** (2020), 52.

[77] I. Pupeza, D. Sánchez, J. Zhang, N. Lilienfein, M. Seidel, N. Karpowicz, T. Paasch-Colberg, I. Znakovskaya, M. Pescher, W. Schweinberger, V. Pervak, E. Fill, O. Pronin, Z. Wei, F. Krausz, A. Apolonski und J. Biegert, *Nature Photonics* **9** (2015), 721.

[78] S. Russell und P. Norvig: *Artificial Intelligence: A Modern Approach*. 3. Auflage. Prentice Hall, 2010.

[79] A.L. Schawlow und C.H. Townes, *Phys. Rev.* **112** (1958), 1940.

[80] T.R. Schibli, J. Kim, O. Kuzucu, J.T. Gopinath, S.N. Tandon, G.S. Petrich, L.A. Kolodziejski, J.G. Fujimoto, E.P. Ippen und F.X. Kaertner, *Optics Letters* **28** (2003), 947.

[81] A. Schliesser, N. Picqué und T.W. Hänsch, *Nature Photonics* **6** (2012), 440.

[82] H.P. Schmid, J.E. McNeal und T.A. Stamey, *Cancer* **71** (1993), 2031.

[83] W. Schweinberger, L. Vamos, J. Xu, S.A. Hussain, C. Baune, S. Rode und I. Pupeza, *Optics Express* **27** (2019), 4789.

[84] D. Sheng, X. Liu, W. Li, Y. Wang, X. Chen und X. Wang, *Spectrochimica Acta Part A: Molecular and Biomolecular Spectroscopy* **101** (2013), 228.

[85] F. Shimizu, *Phys. Rev. Lett.* **19** (1967), 1097.

[86] A.C. Society. *Cancer Facts & Figures 2023*. `https://www.cancer.org/research/cancer-facts-statistics/all-cancer-facts-figures/2023-cancer-facts-figures.html`, 2023.

[87] P. Steinleitner, N. Nagl, M. Kowalczyk, J. Zhang, V. Pervak, C. Hofer, A. Hudzikowski, J. Sotor, A. Weigel, F. Krausz und K.F. Mak, *Nature Photonics* **16** (2022), 512.

[88] M. Sánchez-Brito, F.J. Luna-Rosas, R. Mendoza-González, M.M. Mata-Miranda, J.C. Martínez-Romo und G.J. Vázquez-Zapién, *Talanta* **221** (2021), 121650.

[89] B. Süss, F. Ringleb und J. Heberle, *Review of Scientific Instruments* **87** (2016), 063113.

[90] F. Tauser, C. Rausch, J.H. Posthumus und F. Lison: In *Commercial and Biomedical Applications of Ultrafast Lasers VIII*, herausgegeben von J. Neev, S. Nolte, A. Heisterkamp und C. B. Schaffer, Volume 6881. International Society for Optics and Photonics, SPIE (2008) Pages 139 – 146.

[91] H. Thimbleby, *Journal of Public Health Research* **2** (2013), jphr.2013.e28.

[92] H. Timmers, A. Kowligy, A. Lind, F.C. Cruz, N. Nader, M. Silfies, G. Ycas, T.K. Allison, P.G. Schunemann, S.B. Papp und S.A. Diddams, *Optica* **5** (2018), 727.

[93] V. Untereiner, G. Dhruvananda Sockalingum, R. Garnotel, C. Gobinet, F. Ramaholimihaso, F. Ehrhard, M.D. Diebold und G. Thiéfin, *Journal of Biophotonics* **7** (2014), 241.

[94] L. Voronina, C. Leonardo, J.B. Mueller-Reif, P.E. Geyer, M. Huber, M. Trubetskov, K.V. Kepesidis, J. Behr, M. Mann, F. Krausz und M. Žigman, *Angewandte Chemie International Edition* **60** (2021), 17060.

[95] A. Baltuška, T. Fuji und T. Kobayashi, *Phys. Rev. Lett.* **88** (2002), 133901.

[96] A. Weigel, P. Jacob, D. Gröters, T. Buberl, M. Huber, M. Trubetskov, J. Heberle und I. Pupeza, *Opt. Express* **29** (2021), 20747.

[97] S. Ye, K. Zhong, J. Zhang, W. Hu, J.D. Hirst, G. Zhang, S. Mukamel und J. Jiang, *Journal of the American Chemical Society* **142** (2020), 19071.

[98] J. Zhao, H. Lui, D.I. McLean und H. Zeng, *Applied Spectroscopy* **61** (2007), 1225.

Acknowledgements

Pursuing research as a doctoral student at *Attoworld* over the last four years has been a very memorable journey and a unique learning experience. I would like to thank all the wonderful people who have made this possible.

My heart-filled gratitude to my supervisor, Ferenc Krausz, firstly for believing in me and allowing me to be a part of this truly incredible research group. It is a great privilege to be in an environment with so many brilliant researchers who not only possess great knowledge and expertise but are also willing to pass it on to those who are new. I admire how you have led by example and made extra effort to cultivate a healthy, positive, and productive work culture within the group. To see your effort and dedication bear fruit in the form of the Nobel Prize has been such a joy to behold. To see this happen in my time here at *Attoworld* has made it even more special for me. Thank you for investing in me, for imparting your vision, and for your research guidance and advice. You are truly an inspiration.

I sincerely thank Prof. Jürgen Hauer for his support as the second reviewer of my doctoral dissertation.

Thanks to the International Max Planck Research School - Advanced Photon Science (IMPRS-APS) for supporting my doctoral journey to make it more fruitful. I especially thank Vladislav Yakovlev for providing the environment and resources for my fellow students and me to grow in our research careers.

I am very grateful to Ioachim Pupeza, who served as my project coordinator for the first 2.5 years of my doctoral research period, for being a great mentor in scientific research and beyond. Your guidance, leadership, and great engagement in the project has been a vital aspect, without which we wouldn't have accomplished what we have. Thank you, dear Ioachim, for always being there, especially in times of difficulty, whether a scientific roadblock or a more personal moment of discouragement. Your words of support and encouragement are something I have always found very helpful. I rejoice with you in the recent successes in your academic career.

I am also extremely grateful to Mihaela Žigman, my project coordinator for the last 1.5 years, who has been an inspiring role model and a great leader. Thank you, dear Mihaela, for immediately making me feel welcome in your team. Your sincere and people-centered leadership approach has been a great blessing to me. I am very grateful for all the tips and advice that you have given me, enabling me to reach this far.

I thank Alexander Weigel, whom I have had the honour to work closely with right from the start of my journey at *Attoworld*. You patiently taught, coached, and advised me in all aspects, in the lab, with programming, and in recording, preparing, and presenting my research. What you have invested in me is something more than I, as a young researcher, could ask for or have imagined, and for this I am forever grateful.

Next, I would like to thank Wolfgang Schweinberger, whom I worked closely with for a major portion of my project. Thank you, Wolfgang, for sharing your knowledge and experience, training me to think better while solving problems, and overcoming hurdles in the lab. Thank you for your companionship, advice, honest feedback, and support. I have truly enjoyed working with you.

My special thanks to Frank Fleischmann, our biorepository and lab manager, who has been more than supportive and helpful in all aspects of concern in the lab. Dear Frank, you have always done far more than I ask whenever I have come to you for help or advice. Thank you for that. My sincere thanks to Frank and to Eric Grießinger for all your input, for explaining important aspects of handling biological samples to me, and for patiently training me in this. I am very grateful for your immense support and the team-spirit with which we could together carry out measurments for the *Lasers4Life* campaign.

I thank my former colleagues, Christina Hofer and Theresa Buberl, for being such supportive office mates. Thank you for all the advice, encouragement, and help you have given me over the years, in the lab and outside. I am also thankful to current and former colleagues, Daniel Gerz, Abhijit Maity, Hadil Kassab, Tarek Eissa, Maximilian Högner, Marinus Huber, Lucy Voronina, Sanchi Maithani, Ann-Kathrin Raab, Philipp Sulzer, Michael Trubetskov, Ernst Fill, Kiran Sankar Maiti, Patrik Karandušovský, Kosmas Kepesidis, Lea Gigou, Aleksander Sebesta, Cristina Leonardo, Sebastian Gröbmeyer, Nathalie Nagl, and Wei Liang, for all the interesting scientific discussions as well as the refreshing lunch and coffee breaks. Thank you all so much.

Thank you again, Christina, Mihaela and Ioachim for reading my thesis and providing your valuable feedback.

I am very grateful to the wonderful admin team at *Attoworld* for being so helpful and supportive with all administrative tasks and beyond. Thank

you to Nicole Buchwiser, Ruth Göttler, Klaus Franke, Kerstin Schmidt-Buchmann, Barbara Spindler, Kathrina Adler, and former members Jana Gerding, Nicole Schöber, and Antje Hubacz.

Special thanks to Dr. Hans-Friedrich Wirth, the operations manager at the Laboratory for Extreme Photonics (LEX Photonics), and the Center for Advanced Laser Applications (CALA), and to Florian Saran, for ensuring that conditions are favourable in the labs to carry out our research. Thank you, dear Florian, for always being ready to help and support us whenever the task seems too big for us.

I thank Mr. Rolf Öhm and his team at the mechanical workshop at the LMU Faculty of Physics for their excellent support in producing customized mechanical components required to perform the experiments.

I am very grateful to my teachers at school and university. I especially thank Mrs. Radhika Shiju, my Physics teacher from high school, who introduced me to the joy of learning physics and inspired me to pursue my passion.

I am thankful to my parents and family for supporting me in every way throughout my life, encouraging me to pursue this journey, and ensuring that I had all that I needed.

Lastly, I want to thank my wonderful wife, Rachel, who stood by me even in the most challenging times, doing all you could to make things easier. Thank you, Rach, for believing in me, never giving up on me, and cheering me on. I couldn't have done this without you.